Hindfoot Kinematics of Healthy Subjects Using Lateral Wedge Insoles in a Biplane Fluoroscopy System

Nathan R Pepin

A thesis

submitted in partial fulfillment of the

requirements for the degree of

Master of Science in Mechanical Engineering

University of Washington

2016

Reading Committee:

William Ledoux, Chair

Randal Ching

Katherine Steele

Program Authorized to Offer Degree:

Mechanical Engineering

University of Washington

Abstract

Hindfoot Kinematics of Healthy Subjects Using Lateral Wedge Insoles in a Biplane Fluoroscopy System

Nathan R Pepin

Chair of the Supervisory Committee:
Affiliate Professor William Ledoux
Mechanical Engineering

Lateral wedge insoles (LWIs) are a type of orthosis used to reduce the external knee adduction moment (EKAM), which is associated with the development and progression of tibiofemoral osteoarthritis. However, their effect on kinematics at the hindfoot is unclear. Biplane fluoroscopy was utilized to measure the kinematics of the tibia, talus, and calcaneus, for a pilot study to demonstrate the feasibility of data collection and analysis. To motivate the study, a literature review of LWIs was first performed, including discussion of EKAM, hindfoot moment, dose response, pain scores and more. A LabVIEW Real-Time system was implemented to upgrade the biplane system to add stance phase timing and additional features. Three subjects were studied in the biplane system with four insole conditions. The calcaneus tended to dorsiflex and invert as stance phase progressed. This study demonstrated that the protocol and data analysis are viable and more subjects can be analyzed.

TABLE OF CONTENTS

LIST OF FIGURES

LIST OF TABLES

ACKNOWLEDGEMENTS

I would like to thank my wife and family for the support they gave me through my whole academic career.

Chapter 1. INTRODUCTION

The primary objective of this thesis was to obtain and analyze hindfoot kinematic data of healthy subjects while using lateral wedge insoles (LWIs) in the biplane fluoroscopy system at the VA Puget Sound in Seattle. These data will be used as a pilot study for a future grant submission. This thesis consists of three main chapters: 1) a review of the LWI literature 2) a user manual documenting the upgraded control system for the biplane fluoroscopy laboratory, necessary to perform the data collection, and 3) an article reporting hindfoot kinematics from a pilot sample wearing LWIs. Two appendices detail two related projects: a) a tool developed to facilitate positioning of the fluoroscopy system and b) a review of the biplane fluoroscopy literature.

Chapter 2 of this thesis includes a comprehensive literature review of the biomechanical efficacy of lateral wedge insoles that motivates the proposed research into how lateral wedge insoles affect the foot and ankle. The review primarily covers the change in the external knee adduction moment and the hindfoot moment in response to lateral wedge insoles. The external knee adduction moment has been used as a proxy for medial compartment loading and as a biomechanical indicator for the development of medial knee. The findings from this review article also inform the experimental methodology used for the pilot study. This chapter is formatted as a review article, and will be submitted to a peer reviewed journal in the near future.

Chapter 3 of the thesis is a user manual for the upgraded biplane fluoroscopy system. Prior to data collection of subjects, it was determined that the previous biplane system was insufficient to complete the study. In particular, one major limitation was that there was no way to objectively determine when the subject was in stance phase. As most gait studies report kinematics in terms of stance and swing phase, this complicated comparing data from the previous biplane system to other studies and additionally made normalizing for gait speed challenging. Further, the timing of

the system was poorly-regulated in its previous state, and so it was difficult to synchronize the fluoroscope imaging with other instrument data. To this end, the system was upgraded with a real time control system to add in this functionality. The addition of a strain gage to the walkway allowed for the determination of when the foot was in contact with the ground, thus allowing for the synchronization of trials. This upgrade provided the ability to collect higher-quality data for the pilot study.

Chapter 4 is the main body of work in this thesis which explores the effect of lateral wedge insoles on the foot and ankle. Extensive research about the knee has shown that lateral wedge insoles tend to reduce the external knee adduction moment, but not much is known about the effect on the range of motion and moments at the ankle. All lateral wedge insoles studies that measured the kinematics of the foot and ankle used optical motion capture techniques with markers placed on the skin. These data suffer from skin motion artifact and from the fact that an adequate amount of markers cannot be placed on each bone of interest. The biplane fluoroscopy system, by contrast, can image all the bones (including deeper ones like the talus), and does not suffer from many of the errors associated with traditional motion capture techniques. The prescription of lateral wedge insoles may change foot joint angles during stance phase which may have negative clinical impacts due to hindfoot eversion. The current study is designed to determine the kinematics of the talocrural and subtalar joints while lateral wedge insoles are worn. This study will be submitted to a peer reviewed journal in the near future.

The appendices contain two other smaller projects to be used as tools for the in-house development of the biplane fluoroscopy system. The first is a software tool that recreates the biplane fluoroscopy laboratory in a virtual environment in order to optimize X-ray emitter and image intensifier placement to obtain a better view of the bones of interest. Rearranging the biplane

system is time consuming and it is difficult to determine if the change in geometry will improve bone image quality without the laborious process of moving the system. This software was created as a tool to reduce the time required to optimize imaging geometry but allowing the user to simulate placement of the emitters and image intensifiers. The second is a review of the other biplane fluoroscopy systems currently in use. This was completed to discover improvements to include to our own system. Information such as hardware (high speed cameras, emitters, and image intensifiers), distortion correction methods, marker-based and model-based tracking methods, and the bias and precision of the other systems was tabulated and discussed. This information was used to set benchmarks for our system in how we collect and process data.

Chapter 2. LATERAL WEDGE INSOLE REVIEW

2.1 INTRODUCTION

Osteoarthritis is associated with loss of motion, pain and stiffness in joints, and can be detrimental to a person's quality of life. It is a progressive condition that can require surgery as treatment for advanced stages. Tibiofemoral osteoarthritis (OA) is the most common form of knee osteoarthritis and is estimated to affect 12.5% of the population 45 years and older [1]. It is associated with excessive loading of the medial condyle of the knee [2,3]. One main research thrust is to slow the progression of OA through biomechanical interventions by reducing the load of the knee. The aim is to prolong the time before an invasive treatment such as surgery is required.

Indirect measurements of the medial knee load are used in gait laboratory analysis to easily and non-invasively estimate medial knee loading. The peak and average external knee adduction moment (EKAM) tend to be larger for OA subjects than healthy subjects. The EKAM has been shown to be a reliable surrogate for measuring the load on the medial condyle [2,4]. An elevated EKAM is also a good predictor of future chronic knee pain [5] and correlates with the progression of OA as indicated by radiography [6]. The EKAM follows a double hump pattern with the first hump being larger than the second. Thus, it is believed that lowering the EKAM will decrease medial knee contact forces, relieving pain and slowing the progression of OA.

One conservative, simple, and inexpensive treatment for OA is the prescription of lateral wedge insoles (LWIs). LWIs are orthoses that are placed in the shoe under the foot; they are thicker on the lateral aspect than on the medial, producing a wedge-shaped cross-section. This orthosis geometry is theorized to realign the knee and foot to reduce the EKAM, which unloads

the medial condyle of the knee during stance phase. Studies have suggested that LWIs move the center of pressure (COP) laterally which may reduce the moment arm and thus the moment about the knee.

Previous reviews of the efficacy of LWIs have focused on the reduction of the first peak EKAM as this is thought to be associated with the pain and progression of OA. While the majority of subjects tend to have a reduced EKAM with the prescription of LWIs, there is a consistent ~20% minority that have either no change or an increase in their EKAM [7–9]. Factors such as OA grade, wedge angle or insole customization may change the kinematics and kinetics of the subjects individually. These factors may determine the effectiveness, or lack thereof, of lateral wedge insoles on reducing the EKAM. In addition, reviews have neglected to characterize the kinematics and kinetics at the ankle. The wedges act on the knee through the ankle, which may modify the effectiveness of the LWI. Changes in ankle kinetics and kinematics may present clinical implications in the future. The purpose of this review is to summarize both the application of LWIs and their effect on EKAM, but also emphasize the effect of LWIs on the hindfoot.

2.2 METHODS

2.2.1 *Inclusion Criteria*

All papers that performed a biomechanical analysis with LWIs were considered for evaluation in this review. Papers that met the search criteria were included in the review and were included in all sections that the authors deemed relevant. The articles found in the search were included if they were full text articles in English, and were published in a peer reviewed journal before

February 2016. Only articles containing dynamic over ground walking with LWIs and the EKAM as a primary outcome were included. Thus papers that evaluated LWIs solely in terms of clinical metrics, such as walking score, were omitted. The subject populations were chosen to include healthy controls and/or subjects with medial knee OA, with no other neurological or musculoskeletal pathologies such as stroke. The control conditions for testing included shod, neutral wedge, or barefoot, and insoles had to be either used in fully enclosed shoes or attached to the subjects' bare feet. Shoes that had a wedged outer sole were included, but shoes with a variable stiffness sole were not. Some studies contained varus knee braces, subtalar strapping or other concurrent ankle or knee treatments; however, only the results from the conditions without the concurrent treatments are reported in this review.

2.2.2 *Search Strategy*

Studies were searched for in the Web of Science database using the search terms "lateral wedg*", "foot ortho*", "wedge ortho*", "wedg* insol*", and "varus wedg*". Two authors (NP, MK) first screened all studies independently by title and abstract to eliminate obvious exclusions. If the paper met the inclusion criteria, full documents were retrieved. All of the relevant studies found using the search terms then had their citation list checked for additional studies. All included studies were then reviewed and discussed by authors NP, MK, JI, and WL.

The percent difference in EKAM and hindfoot moment were calculated for all studies between the LWIs and the corresponding control conditions. All studies were tabulated with relevant methods, materials and results. Studies were separated into healthy or OA populations. The papers with both populations were split into their respective categories. A further subdivision was created within the healthy or OA split to categorize the studies by their control

condition, such as shod (without a neutral wedge in a shoe) or neutral (if a neutral wedge was placed in the shoe). A third category was created to compare the LWI to barefoot.

2.2.3 *Risk of Bias*

A risk of bias assessment was completed using a modified Downs and Black checklist by two authors (NP, MK). A validation of this modified questionnaire was not completed to determine the ability of the questionnaire to accurately and consistently rate studies as it has been modified in a similar fashion in the past to assess similar biomechanical studies [10,11]. Ten questions were excluded from the original checklist, as they did not pertain to a one time laboratory based randomized control trial (questions 8, 9, 13, 17, 19, 21-26). Questions 5, 14, and 27 (5, 11, and 16 in modified checklist) were modified to better suit the studies included and the checklist can be found in Appendix A. The confounder that was used in question 5 was walking speed, as that has been shown to affect the magnitude of EKAM [12]. Question 14 was changed to determine if the insole order was randomized. Question 27 was modified to determine if the study reported a power calculation before recruitment, and was the recruitment equal to or greater than the calculated number of subjects to detect a clinically important effect where the probability value for a difference due to chance is less than 5%. Two authors (NP and MK) independently completed the risk of bias assessment of all included articles. The papers were rated for quality as high (>85%), medium (70-85%) and low (<70%).

2.3 RESULTS

The search produced (230) articles and after they were screened for relevance 46 remained. Six studies were excluded after the full article was retrieved: one was not in a peer-reviewed journal, three studies contained minimalist footwear, one study contained a shoe with an adjustable sole and one study reported a subject with concurrent knee surgery. Three papers were found in the reference list of included papers. Forty three papers were included in the review (Figure 1). Four studies had a population that was excluded from the review, while the healthy populations were included [13–16].

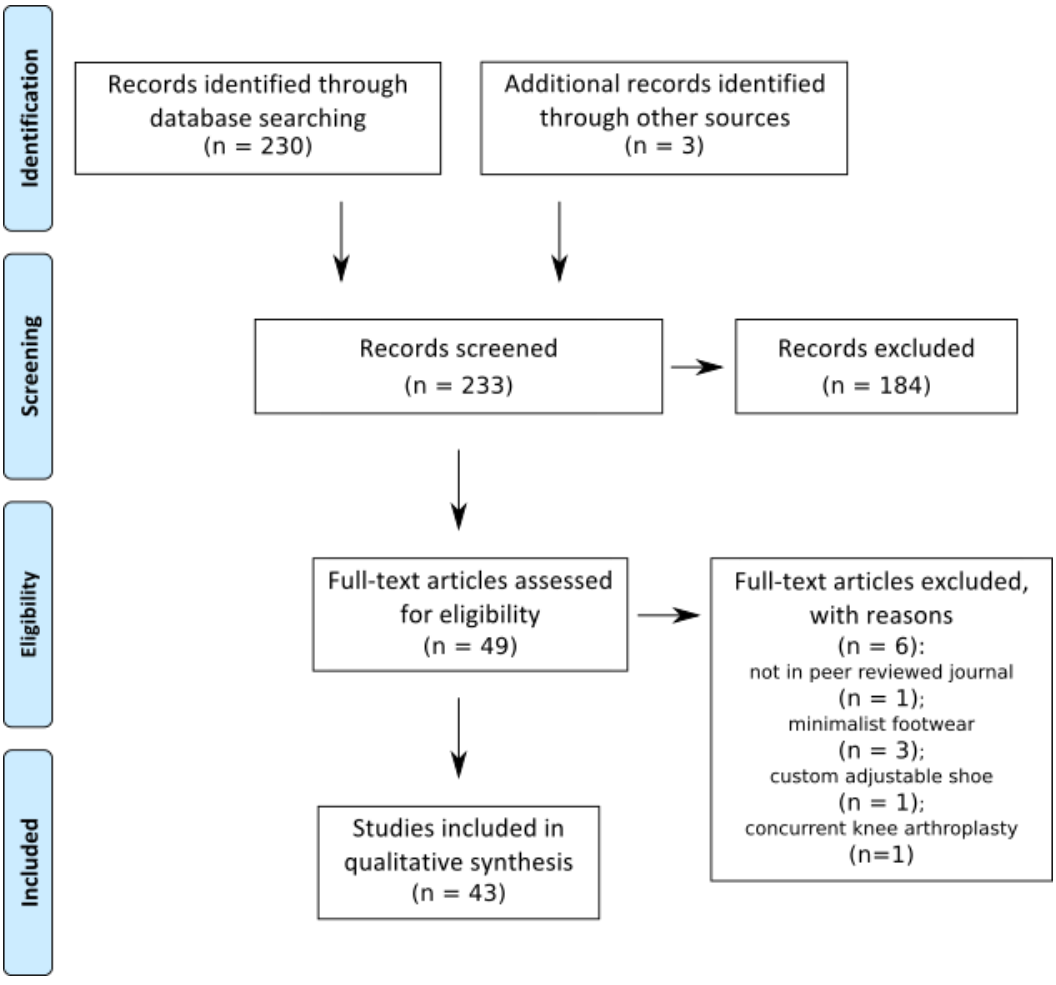

Figure 2.1. Flowchart describing the inclusion and exclusion of the papers for the review.

Twenty studies investigated the use of LWIs on the EKAM with a healthy subject population [7,8,13–30]. The wedge angle of the insoles ranged from 2 to 14 degrees and the change in EKAM ranged between a 19.8% increase to a 24.4% reduction compared to the specified control conditions [15,18]. Most studies reported a reduction in EKAM between 5 and 10% with respect to the control conditions (shod or neutral wedging) (Figure 2.2, Figure 2.3). Six of the studies included LWIs with arch supports [15,21,23,25,27,30].

Twenty six studies investigated the effects of LWIs on the EKAM of subjects with medial knee OA [7–9,22,27,30–50] clinically classified by the Kellgren Lawrence scale. The degree of wedging ranged from 4 to 11degrees. A reduction in EKAM was found to be between 1.6% and 11.9% [22,36]; the majority of these studies reduced EKAM between 4 and 9% (Figure 2.4, Figure 2.5). Eight studies included LWIs with arch supports [27,30,32,33,38,40,41,47]

Four studies compared the use of LWIs to that of walking barefoot with OA subjects [34,44,51,52] and no studies used barefoot as a control with healthy subjects (Figure 2.6). The change in EKAM ranged between an increase of 14% to a decrease of 9% [34,44] with the majority of studies finding a decrease in EKAM of 5 to 8%.

Thirteen studies described the hindfoot moment in healthy subjects with the prescription of LWIs [7,8,13,15,18–21,23,25–28]. Most of the studies found an increase in hindfoot moment between 6% and 81%; however, the range was wide, varying from an increase of 725% to a decrease of 22% [25,27] (Figure 2.7, Figure 2.8) .

Eight studies that measured the hindfoot moment used OA subjects [7,8,27,33,39,41,44,48] with a hindfoot moment ranging between a 7% decrease to a 600% increase with most studies between a 10 and 50% increase compared to the control conditions (Figure 2.9, Figure 2.10).

The studies had an average quality score ± SD of 79.9 ± 9.4% (Chapter 16.36.3). Six were scored low quality (<70%), 20 scored medium quality (70-85%) and 17 scored high quality (>85%). All but five papers scored well in the reporting category. Around half of the papers scored well in external validity with 25 of 43 papers describing the population from which the subjects were recruited. The majority of the papers scored at least moderate in internal validity but only three papers blinded the researchers to the test conditions. Twelve studies completed a power analysis beforehand.

Table 2.1. Included studies with relevant parameters and results.

Author	Population Statistics	Walking Speed	Kinematic and Kinetic Data Capture Devices	Wedge Construction	Wedge Condition	EKAM Percent Change From Control	Hindfoot Moment Percent Change From Control
Crenshaw [17]	healthy only 17 total 27.7 (6.5) years	self-selected	6 camera motion capture (Motion Analysis Corp.) 60 Hz 1 force plate (AMTI) 1000 Hz	full length nickleplast subjects' own shoes	C: 0 degree wedge I: 5 degree wedge	C vs I: -6.8*	
Kerrigan [31]	OA only 7 female + 8 male 69.7 (7.6) years 10 K-L III 5 K-L IV	self-selected	unspecified number of cameras for motion capture (Vicon) 120 Hz 2 force plates (AMTI) unspecified Hz	full length amerifoam durometer 55 subjects' own shoes	C: Shod I1: 3.175mm flat I2: 5 degree wedge I3: 6.35mm flat I4: 10 degree wedge	C vs I1: -5.3* I1 vs I2: -3.8* C vs I4: -8.3* I3 vs I4: -8.1*	
Maly [40]	OA only 3 female + 9 male 60.0 (9.4) years	self-selected	unspecified number of cameras for motion capture (Qgait) 100 Hz 1 force plate (AMTI) 100 Hz	heel wedge unspecified material routine footwear	C: shod I1: 5 degree wedge I2: orthosis	C vs I1: -2.1 P < 0.101 C vs I2: 4.2	
Nester [25]	healthy only 7 female + 8 male 19 to 41 years	108 steps/minute	unspecified motion capture 2 force plates (Kistler) 200 Hz	heel to metatarsal heads high density eva with softer base over wedge medium density medial arch support subjects' own shoes	C: shod I: wedge lateral	C vs I: No reported changes	C vs I: -22.6
Kakihana[18]	healthy only 5 female + 5 male female 24.8 (2.1) years male 25.2 (4.3) years	85 steps/minute	7-12 camera motion capture (Vicon) at 60 Hz multiple but unspecified number of force plates (Kistler) at 60 Hz	full length eva 100-300 kg/mm^2 taped to bare feet	C: 0 degree wedge I1: 3 degree wedge I2: 6 degree wedge	C vs I1: -8.9 C vs I2: -24.4*	C vs I: 18.8 C vs I2: 56.3*
Kakihana[7]	13 healthy 13 female 64.6 (2.3) years 13 OA 13 female 63.3 (5.6) years	95 steps/ minute	12 camera motion capture (Vicon) 60 Hz 8 force plates (9281C) 60 Hz	full length eva 8200 100-300 kg/mm^2 taped to bare feet	C1: 0 degree wedge I1: 6 degree wedge C2: 0 degree wedge I2: 6 degree wedge	C1 vs I1: -10.3* C2 vs I2: -5.6*	C1 vs I1: 27.8* C2 vs I2: 23.5*

Kakihana[13]	healthy only 25 male 20.7 (1.2) years	self-selected	12 camera motion capture (Vicon) at 60 Hz 8 force plates (9281C) 60 Hz	full length eva 100-300 kg/mm^2 taped to bare feet	C: 0 degree wedge I: 6 degree wedge	C vs I: -9.4*	C vs I: 16.7*
Schmalz[19]	healthy only 4 female + 6 male 34 (9) years	self-selected	6 camera motion capture (Vicon) 120 Hz 2 force plates (Kistler) 1080 Hz	full length unspecified material wedge attached to underside of shoe lab shoe	C: shod I: 14 degree wedge	C vs I: -5.6*	C vs I: 25.9*
Shimada[52]	19 healthy 14 female + 5 male 66.4 (9.3) years 23 OA 17 female + 6 male 67.0 (8.7) years	self-selected	4 camera motion capture (g1812cs) 50 Hz 2 force plates (g1812cs) 50 Hz	heel wedge silicon attached to bare feet	no insole healthy C1: no insole k-l I C2: no insole k-l II C3: no insole k-l III C4: no insole k-l IV C5: no insole all ave I1: 10 mm k-l I I2: 10 mm k-l II I3: 10 mm k-l III I4: 10 mm k-l IV I5: 10 mm all ave	C1 vs I1: -5.1* C2 vs I2: -6.6* C3 vs I3: -3.3 P = 0.058 C4 vs I4: -5.0 P = 0.086 C5 vs I5: -4.4*	
Kakihana[8]	19 healthy 19 female 67.1 (4.2) years 51 OA 51 female 65.5 (3.8) years 22 K-L I 24 K-L II 3 K-L III 2 K-L IV	self-selected	12 camera motion capture (Vicon) 60Hz 8 force platforms (9281C) 60 Hz	full length eva 8200 100-300 kg/mm^2 taped to bare feet	C1: 0 degree wedge healthy I1: 6 degree wedge C2: 0 degree wedge OA I2: 6 degree wedge	C1 vs I1: -11.3* C2 vs I2: -6.0*	C1 vs I1: 29.1* C2 vs I2: 13.0*
Kuroyanagi[34]	OA only 21 total 72 years 20 K-L II 11 K-L III 6 K-L IV	self-selected	6 camera motion capture (Qualysis) 120 Hz 1 force plate (Bertec) 120 Hz	unspecified length silicon rubber attached to bare feet	C1: barefoot k-l II C2: barefoot k-l III C3: barefoot k-l IV I1: 7.6 degree wedge k-l II I2: 7.6 degree wedge k-l III I3: 7.6 degree wedge k-l IV	C1 vs I1: -7.7* C2 vs I2: -8.9* C3 vs I3: -6.3*	

Butler[32]	OA only 11 female + 9 male 63 (6) years 7 K-L II 6 K-L III 7 K-L IV	self-selected	unspecified number of cameras for motion capture (Vicon) 120 Hz 1 force plate (unspecified) 1080 Hz	heel to metatarsal heads crepe durometer 70 with micropuff cover arch supports lab shoe (New Balance 810)	C: shod I: self-selected wedge (9.6 degree ± 3.2 degree)	C vs I: -8.7*	
Hinman[36]	OA only 7 female + 6 male 59.7 (6.2) years	self-selected	8 camera motion capture (Vicon) 120 Hz 2 force plates (AMTI) 1080 Hz	full length or heel wedge high density eva high density eva subjects' own shoes	C: shod I1: 5 degree hindfoot wedge I2: 5 degree wedge full length	C1 vs I1: -7.5 P = 0.158 C2 Vs I2: -11.9* I1 vs I2: -4.8 P =0.055	
Hinman[35]	OA only 24 female + 16 male 64.7 (9.4) years 3 K-L I 10 K-L II 11 K-L III 16 K-L IV	self-selected	6 camera motion capture (Vicon) 120 Hz 2 force plates (AMTI) 1080 Hz	full length high density eva subjects' own shoes	baseline C1: shod baseline I1: 5 degree wedge baseline	C1 vs I1: -5.4*	
Erhart[20]	healthy only 9 female + 6 male 28.6 (4) years	self-selected slow, medium and fast	8 camera motion capture (Qualysis) 120 Hz 1 force plate (Bertec) 120 Hz 1 pressure mat (Rsscan Interntional) 120 Hz	full length shoe outsole is wedged durometer asker c lab shoe	C1: 0 degree wedge slow C2: 0 degree wedge medium C3: 0 degree wedge fast I1: 4 degree wedge slow I2: 4 degree wedge medium I3: 4 degree wedge fast I4: 8 degree wedge slow I5: 8 degree wedge medium I6: 8 degree wedge fast	C1 vs I1: -8.9* C2 vs I2: -7.6* C3 vs I3: -8.5* C1 vs I4: -17.3* C2 vs I5: -12.6* C3 vs I6: -19.1*	C1 vs I1: 81.8* C2 vs I2: 66.7* C3 vs I3: 54.8* C1 vs I4: 168.2* C2 vs I5: 126.7* C3 vs I6: 97.6*

Butler [33]	OA only 17 female + 13 male 63.1 (6.8) years 9 K-L II 9 K-L III 11 K-L IV	self-selected	6 camera motion capture (Vicon) 120 Hz 1 force plate (Bertec) 1080 Hz	unspecified length unspecified material with micropuff cover durometer 70 arch support lab shoe New Balance 812	C: shod I: self-selected wedge (10.0 degree ± 3.2 degree)	C vs I: -8.7*	C vs I: 90.0*
Nakajima[21]	healthy only 9 female + 11 male unspecified age	self-selected	12 camera motion capture (Vicon) 60 Hz 8 forces plates (Kistler) unspecified Hz	full length eva 100-300 kg/mm^2 some conditions with semicustom arch support taped to bare feet	C: 0 degree wedge I1: 0 degree wedge w/ AS I2: 6 degree wedge I3: 6 degree wedge w/ AS	C vs I1: similar C vs I2: -8.5* C vs I3: -7.4*	C vs I1: similar C vs I2: 15.7* C vs I3: 18.1*
Segal[51]	OA only 11 total 51.9 (8.3) years	self-selected	unspecified number of cameras for motion capture Optotrack Motion Analysis System (Northern Digital Inc.) unspecified Hz unspecified number of force plates (Kistler) unspecified Hz	half length dynaflex thermoplastic durometer 50 not specified type of shoe	C: barefoot I1: 6 degree wedge	C vs I1: 1.5	
Hinman[9]	OA only 12 female + 8 male 63.5 (9.4) years 8 K-L II 12 K-L III	self-selected	8 camera motion capture (Vicon) 120 Hz 2 force plates (AMTI) 1080 Hz	full length high density eva durometer type a subjects' own shoes	C1: shod I1: 5 degree wedge C2: shod follow up I2: 5 degree wedge follow up	C1 vs I1: -5.2* C2 vs I2: -4.2*	
Abdallah[41]	OA only 21 female 54.1 (7.42) years	self-selected	6 camera motion capture (Qualisys) 120 Hz 1 force plate (AMTI) 1200 Hz	full length pedilin and plastazote leather cover arch support lab shoes thin and flexible	C: 0x0 degree wedge I1: 6x6 degree wedge I2: 11x11 degree wedge I3: 6x0 degree wedge I4: 11x0 degree wedge	C vs I1: -4.5 C vs I2: -7.6 C vs I3: -9.1 C vs I4: -4.5	C vs I1: 125.0* C vs I2: 225.0* C vs I3: 150.0* C vs I4: 225.0*
Hinman[9]	OA only 45 female + 28 male 63.3 (8.4) years	self-selected	6-8 camera motion capture (Vicon) 120 Hz 2 force plates (AMTI) 1080 Hz	full length eva durometer 70 subjects' own shoes	C: shod I: 5 degree wedge	C vs I: -5.8*	
Leitch[22]	14 healthy	self-selected	8 camera motion capture (Motion Analysis Corp.) 60 Hz	heel wedge eva foam	C1: 0 degree wedge I1: 4 degree wedge	C1 vs I1: -3.9 C1 vs I2: -5.1*	

	10 female + 4 male healthy 44 (8) years 12 OA 7 female + 5 male OA 48 (9) years 2 K-L I 2 K-L II 3 K-L III 5 K-L IV		1 force plate (AMTI) 1200 Hz insole pressure (novel electronics inc.) 60 Hz	durometer shore a 55 lab shoe New Balance 882	I2: 8 degree wedge C2: 0 degree wedge OA I3: 4 degree wedge OA I4: 8 degree wedge OA	C2 vs I3: -1.5 C2 vs I4: -3.3*	
Pagani[48]	OA only 8 female + 2 male 57.5 (7.1) years 6 K-L II 4 K-L III	self-selected	10 camera motion capture (Vicon) 200 Hz 2 force plates (Kistler) 1000 Hz	full length eva lab shoe	C: shod I: 4 degree wedge	C vs I: -7.3	C vs I: 21.6
Moyer[50]	OA only 55 (7) 2 K-L I 5 K-L II 6 K-L III 3 K-L IV	self-selected	8 camera motion capture (Vicon) 60 Hz unspecified number of force plates (AMTI) 1200 Hz	full length eva 3, 6, or 9mm lateral rise durometer shore A 55 custom molded to subjects' feet lab shoe New Balance	C: shod I: custom size wedge	C vs I: -3.2	
Kang[26]	healthy only 24 female + 24 male 23.5 (2.5) years	self-selected	6 camera motion capture (Motion Analyis Corp.) 60 Hz 2 force plates (unspecified unspecified Hz	full length shoe outsole is modified lab shoes	C: shod I: 5 degree wedge	C vs I: -21.3*	C vs I: 228.6*
Arazpour[49]	OA only 7 female + 5 male 4 K-L I 8 K-L II	non-controlled self-selected walking speed	6 camera motion capture (Vicon) 100 Hz 2 force plates (Kistler) unspecified Hz	full length cork composite durometer 60 lab shoe	C:shod I: 6 degree wedge	C vs I: -12.9*	
Jones[23]	healthy only 5 female + 10 male 30.5 (8.6) years	self-selected	10 camera motion capture (Vicon) 100 Hz 2 force plates (Kistler) 3000 Hz	heel to metatarsal heads unspecified material durometer shore a 70 one condition with medial arch support lab shoe Ecco Zen	C: shod I1: 5 degree wedge w/ antipronatory device I2: 5 degree wedge	C vs I1: -9.8* C vs I2: -9.8*	C vs I1: 20.0* C vs I2: 25.0*

Jones[45]	OA only 12 female + 16 male 66.3 (8.2) years 10 K-L II 18 K-L III	self-selected	8 camera motion capture (Qualisys) 100 Hz 2 force plates (Kistler) 200 Hz	heel to metatarsal heads unspecified material durometer shore a 70 medial arch support lab shoe Ecco Zen	C: shod I: 5 degree wedge	C vs I: -12.7*	
Russell[14,16]	14 healthy 14 female 26.1 (6.9) years	1.24 m/s	8 camera motion capture (Qualisys) 240 Hz 1 force plate (AMTI) 1200 Hz	full length eva lab shoe New Balance RC 550	C1: shod I1: 8 degree wedge	C1 vs I1: -6.5*	
Barrios[42]	OA only 19 w/ neutral 62.6 (7.4) years 8 K-L II 6 K-L III 5 K-L IV 19 w/ lwi 61.2 (9.4) years 9 K-L II 8 K-L III 5 K-L IV	self-selected	6 camera motion capture (Vicon) at 120 Hz 1 force plate (Bertec) at 1080 Hz	heel to metatarsal heads crepe durometer 70 lab shoe New Balance 810	self-selected wedge OA 8.7 ± 3.3 degree C1: control group 0 month I1: control group 12 month C2: lwi group w/o lwi 0 month I2: lwi group w/ lwi 0 month C3: lwi group w/o lwi 12 month I3: lwi group w/ lwi 12 month	C1 vs I1: 8.5 P = 0.052 C2 vs I2: -7.3 C3 vs I3: -7.8 Significant when pooled across visits C2 vs I2 and C3 vs I3	
Telfer[15]	healthy only 6 female + 6 male 28 (5.6) years	self-selected	12 camera motion capture (Qualisys) 120 Hz 1 force plate (Kistler) 2400 Hz	heel to metatarsal heads 3D printed custom to foot lab shoe custom modified	C1:shod I1: 0 degree wedge I2: 2 degree wedge I3: 4 degree wedge I4: 6 degree wedge	C1 vs I1: 12.2 C1 vs I2: 6.3 C1 vs I3: 19.8 C1 vs I4: 7.3	C1 vs I1: -15.3* C1 vs I2: -15.9* C1 vs I3: -18.9* C1 vs I4: -11.0*
Jones[46]	OA only 22 female + 29 male 59.6 (8.9) years 22 K-L II 29 K-L III	self-selected	16 camera motion capture (Qualisys) 100 Hz 4 force plates (AMTI) 200 Hz	heel to metatarsal heads unspecified material durometer shore a 70 one condition with medial arch support, in results it is averaged with typical wedge lab shoe Ecco Zen	C1: shod affected leg I1: 5 degree wedge ave affected leg C2: shod unaffected leg I2: 5 degree wedge ave unaffected leg	C1 vs I1: -4.8* C2 vs I2: -9.3*	
Molgaard[28]	healthy only 4 female + 8 male 31.9 years	self-selected	8 camera motion capture (Qualisys) 120 Hz 2 force plates (AMTI) 1200 Hz	full length rehband technogel lab shoe Nike Air Pegasus	C1: neutral no injection I1: 10 degree wedge no injection	C vs I: -5.0*	C vs I: 30.0*
Tipnis[24]	25 healthy	1.46 m/s	8 camera motion capture	full length	C: 0 degree wedge	C vs I1: -6.4*	

	13 female + 12 male 23.1 (2.3) years		(Vicon) 100 hz 1 force plate (Bertec) 1500 hz	crepe with micropuff cover inserted under orthosis durometer 70 lab shoe Nike Air Pegasus	I1: 2 degree wedge I2: 4 degree wedge I3: 6 degree wedge I4: 8 degree wedge I5: 10 degree wedge I6: 12 degree wedge	C vs I2: -10.3* C vs I3: -10.9* C vs I4: -10.9* C vs I5: -13.1* C vs I6: -12.8*	
Yeh[27]	15 healthy 15 female 66.8 (5.45) 15 OA 15 female OA 65.27 (4.04) years all K-L II or III	self-selected	6 camera motion capture (Vicon) 120 Hz 2 force plates (AMTI) 1080 Hz	full length eva semi-custom lab shoe kung fu shoes	C1: shod I1: 7 degree wedge C2: shod OA I2: 7 degree wedge OA	C1 vs I1: -8.6* C2 vs I2: -4.0*	C1 vs I1: 725.0* C2 vs I2: 600.0*
Pagani[29]	14 healthy 14 male 24 (4.8) years	self-selected	10 camera motion capture (Vicon) 200Hz 2 force plates (Kistler) 1000 Hz	unspecified length unspecified material lab shoe victoria sneaker marron	C: shod I: 4 degree wedge	C vs I: 0.0	
Duivenvoorden[43]	OA only 28 female + 14 male 54 (7) years 15 K-L 1 8 K-L II 18 K-L III 1 K-L IV	self-selected	3 camera motion capture (Qualisys) 100 Hz 1 foroce plate (AMTI) 200 Hz	full length cork with leather bottom subjects' own shoes	C: shod I: 6 degree wedge	C vs I: -4.0	
Fu[30]	OA only 6 female + 4 male 56 years	Not specified	6 camera motion capture (Vicon) 60 Hz 1 force plate (Kistler) 60 Hz	full length insole unspecified length unspecified material	C: flat insole I1: lwi I2: lwi w/ arch support	C vs I1: -13.0* C vs I2: -13.5*	
Hsu[44]	OA only 10 female 66 (5.3) years	0.77 m/s barefoot baseline 0.78 m/s lwi baseline 0.90 m/s barefoot follow up 0.85 m/s lwi follow up	6 camera motion capture (Vicon) 120 Hz 2 force plates (AMTI) 1080 Hz	full length eva semicustom medial arch support lab shoes kung fu shoes	C1: barefoot baseline I1: 7 degree wedge baseline C2: barefoot 6 week I2: 7 degree wedge 6 week	C1 vs I1: -8.4 P = 0.15 C2 vs I2: -14.1 P = 0.35 C1 vs C2: -28.2* I1 vs I2: -10.6 P = 0.25	C1 vs I1: 44.4* P = 0.42 C2 vs I2: -6.8 P = 0.83 C1 vs C2: 118.5 P = 0.35 I1 vs I2: 41.0 P = 0.05
Chapman[39]	OA only 27 female + 43 male 60.3 (9.6) years	self-selected	16 camera motion capture (Qualsys) 100 Hz 4 force plates (AMTI) 200 Hz	heel to metatarsal heads eva durometer shore a lab shoe Ecco Zen	C: shod I: 5 degree wedge	C vs I: -5.8*	C vs I: 54.5*

	all K-L II or III					
Jones[38,47]	OA only 27 female + 43 male 60.3 (9.6) years all K-L II or III	self-selected	16 camera motion capture (Qualisys) 100 Hz 4 force plates (AMTI) 200 Hz	heel to metatarsal heads unspecified material durometer shore a 70 one condition with medial arch support lab shoe Ecco Zen	C: shod I1: barefoot I2: 5 degree wedge I3: 5 degree wedge w/ arch support	C vs I1: -7.7* C vs I2: -5.1* C vs I3: -5.1* I1 vs I2: no difference I1 vs I3: no difference

P values reported for all significant results are marked with an *.
K-L = Kellgren-Lawrence grade, C = Control condition, I = Intervention number

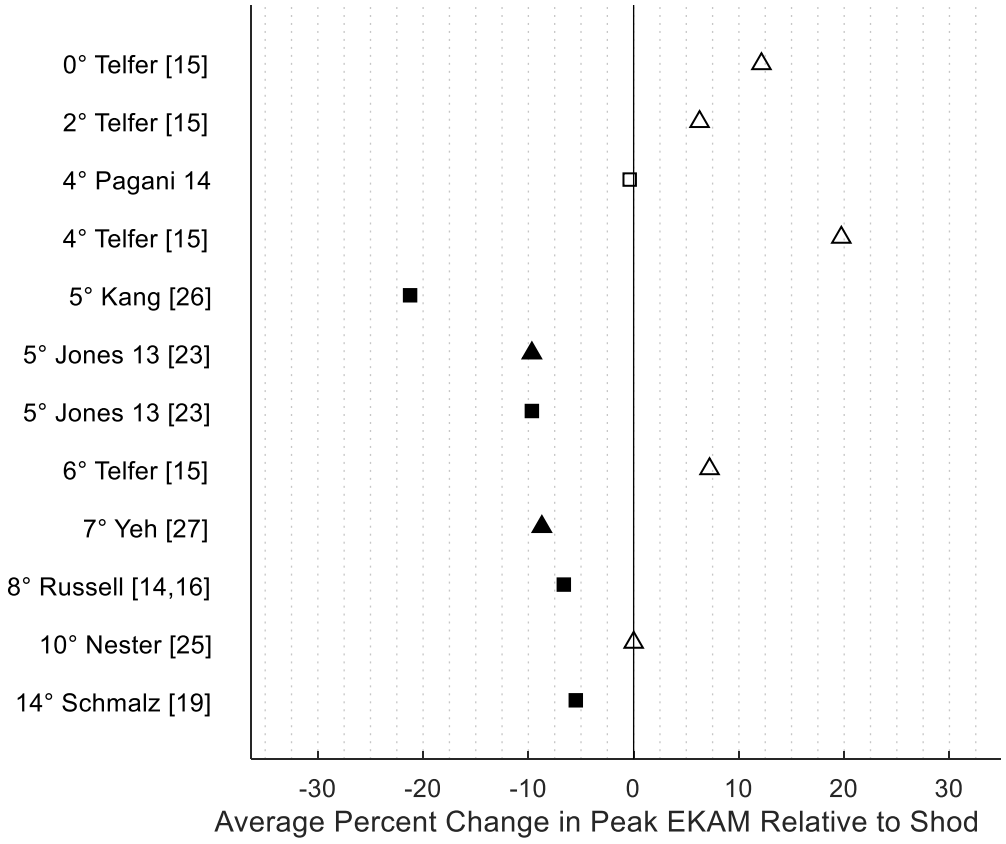

Figure 2.2. The percent change in EKAM relative to shod with healthy subjects. Squares represent typical wedges, and triangles represent LWIs with arch supports. A solid symbol represents a statistically significant change, while a hollow symbol represents a non-statistically significant change.

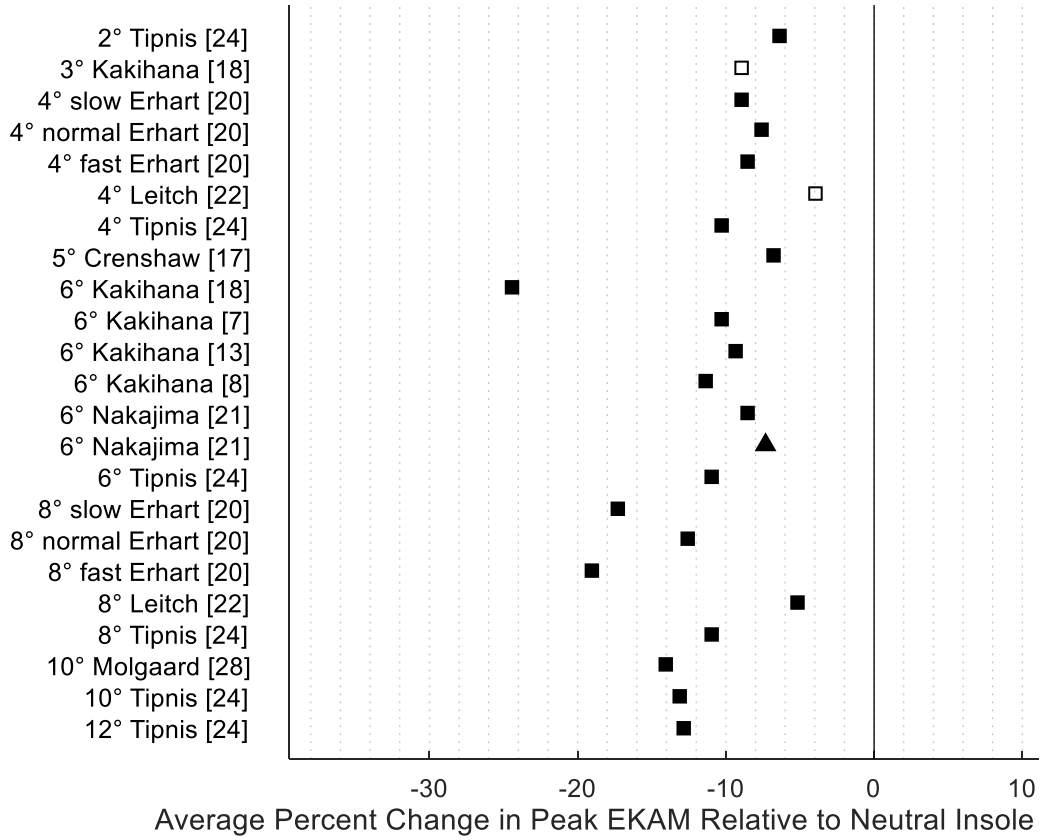

Figure 2.3. The percent change in EKAM relative to neutral insoles with healthy subjects. Squares represent typical wedges, and triangles represent LWIs with arch supports. A solid symbol represents a statistically significant change, while a hollow symbol represents a non-statistically significant change.

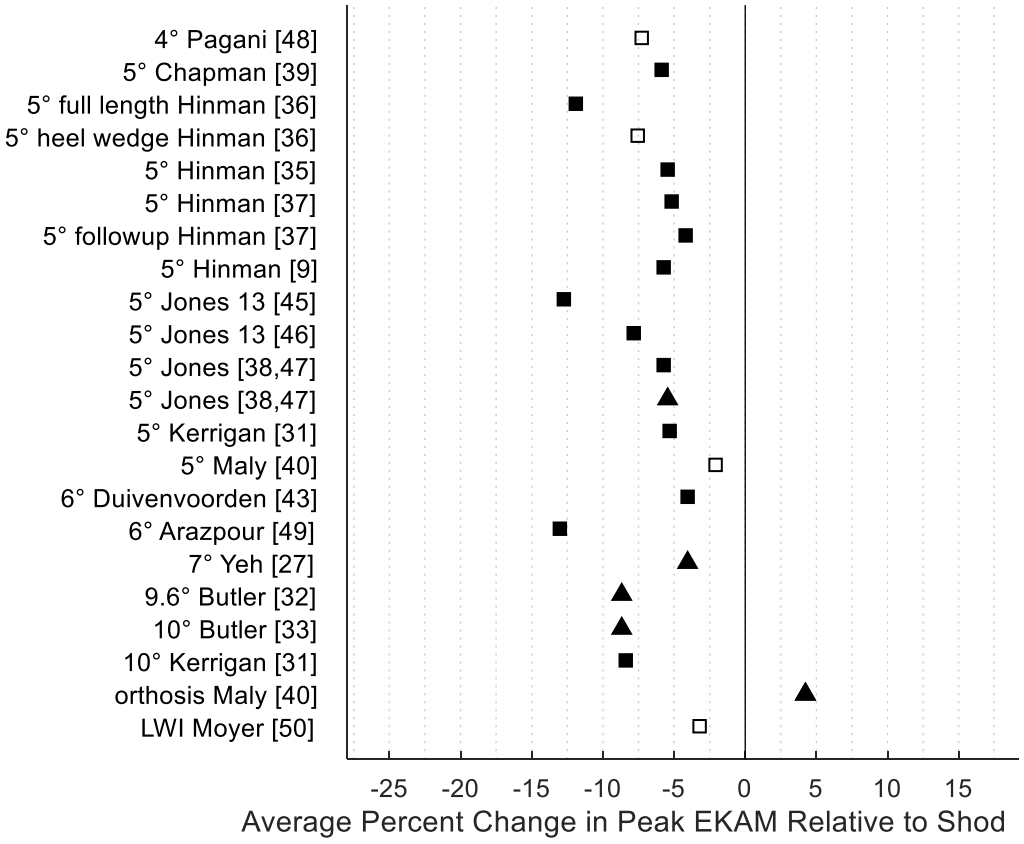

Figure 2.4. The percent change in EKAM relative to shod with OA subjects. Squares represent typical wedges, and triangles represent LWIs with arch supports. A solid symbol represents a statistically significant change, while a hollow symbol represents a non-statistically significant change.

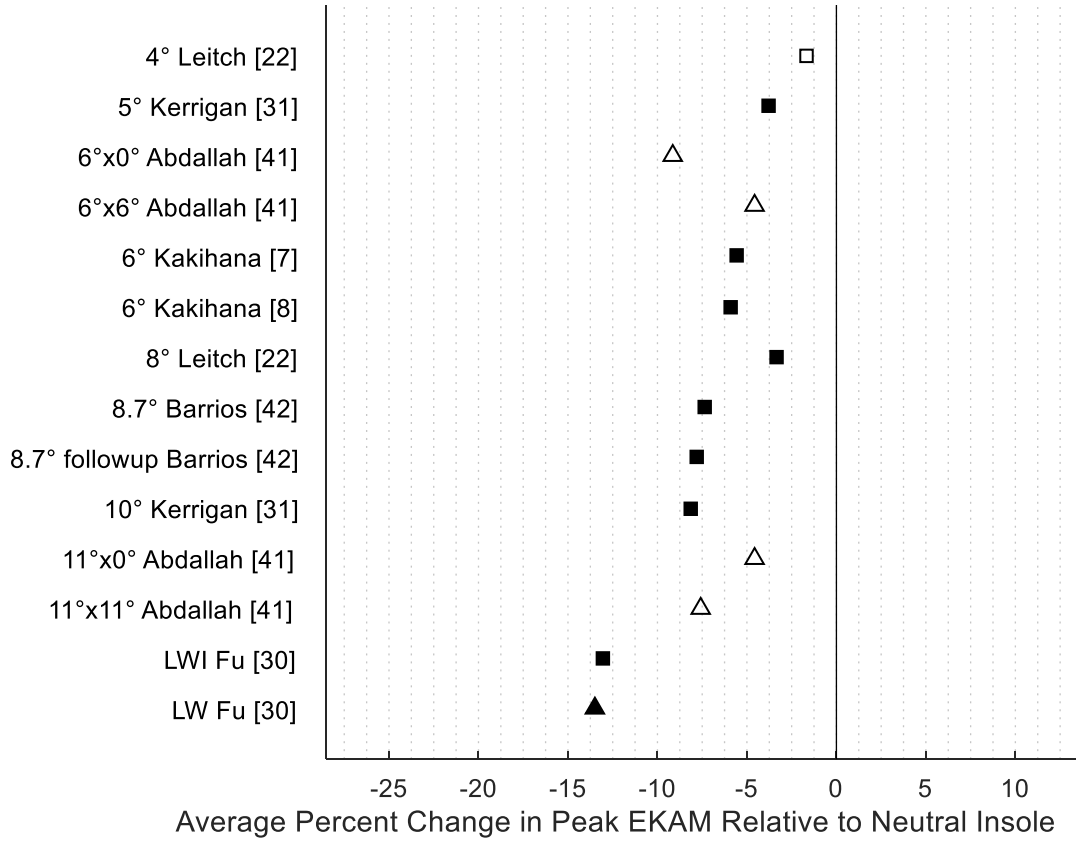

Figure 2.5. The percent change in EKAM relative to neutral insoles with OA subjects. Squares represent typical wedges, and triangles represent LWIs with arch supports. A solid symbol represents a statistically significant change, while a hollow symbol represents a non-statistically significant change.

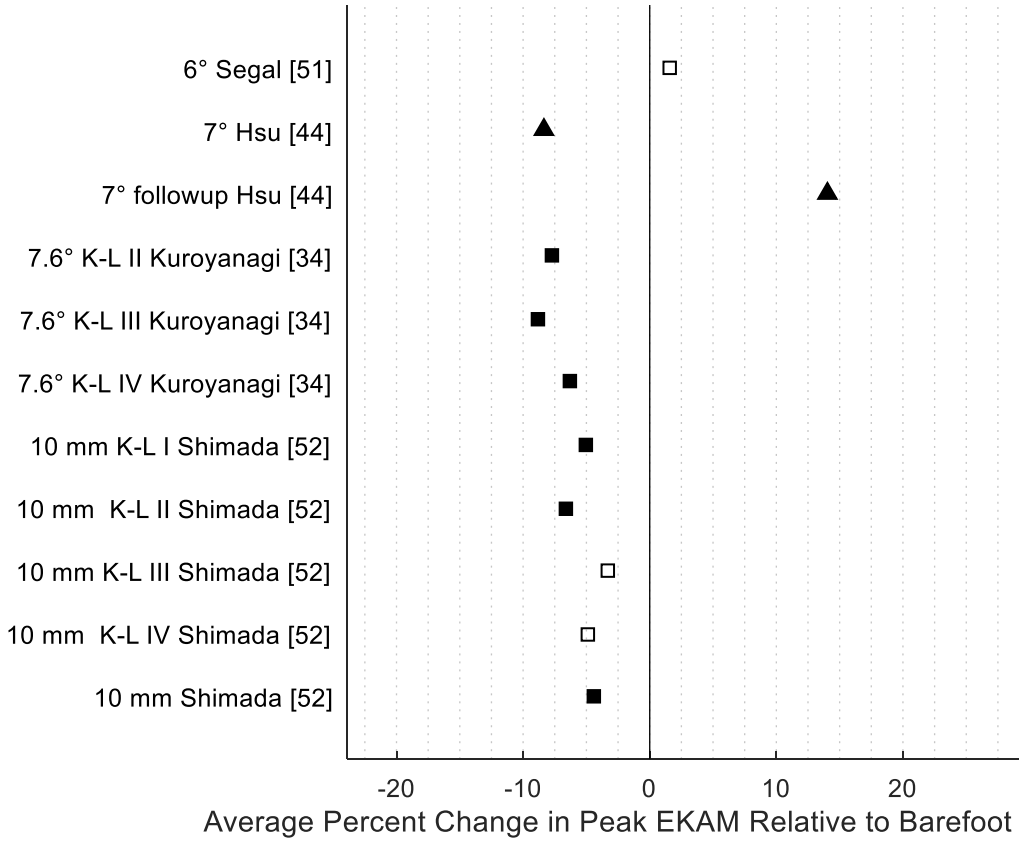

Figure 2.6. The percent change in EKAM relative to barefoot with OA subjects. Squares represent typical wedges, and triangles represent LWIs with arch supports. A solid symbol represents a statistically significant change, while a hollow symbol represents a non-statistically significant change.

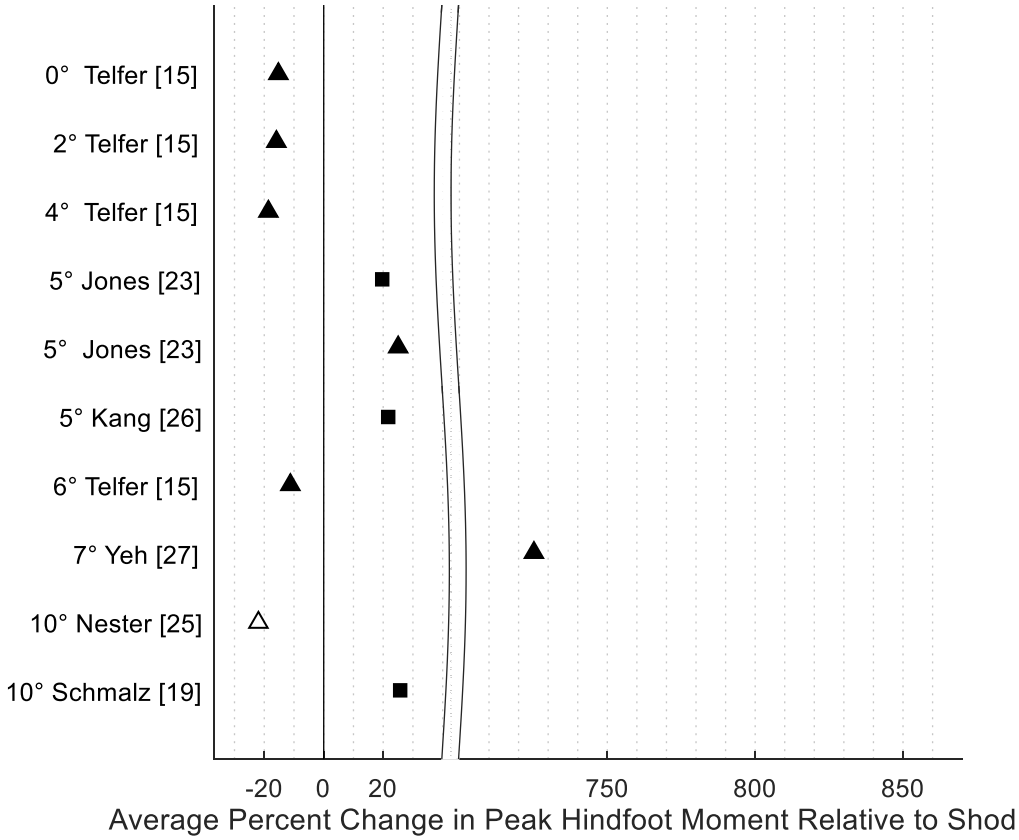

Figure 2.7. The percent change in hindfoot moment relative to shod with healthy subjects. Squares represent typical wedges, and triangles represent LWIs with arch supports. A solid symbol represents a statistically significant change, while a hollow symbol represents a non-statistically significant change.

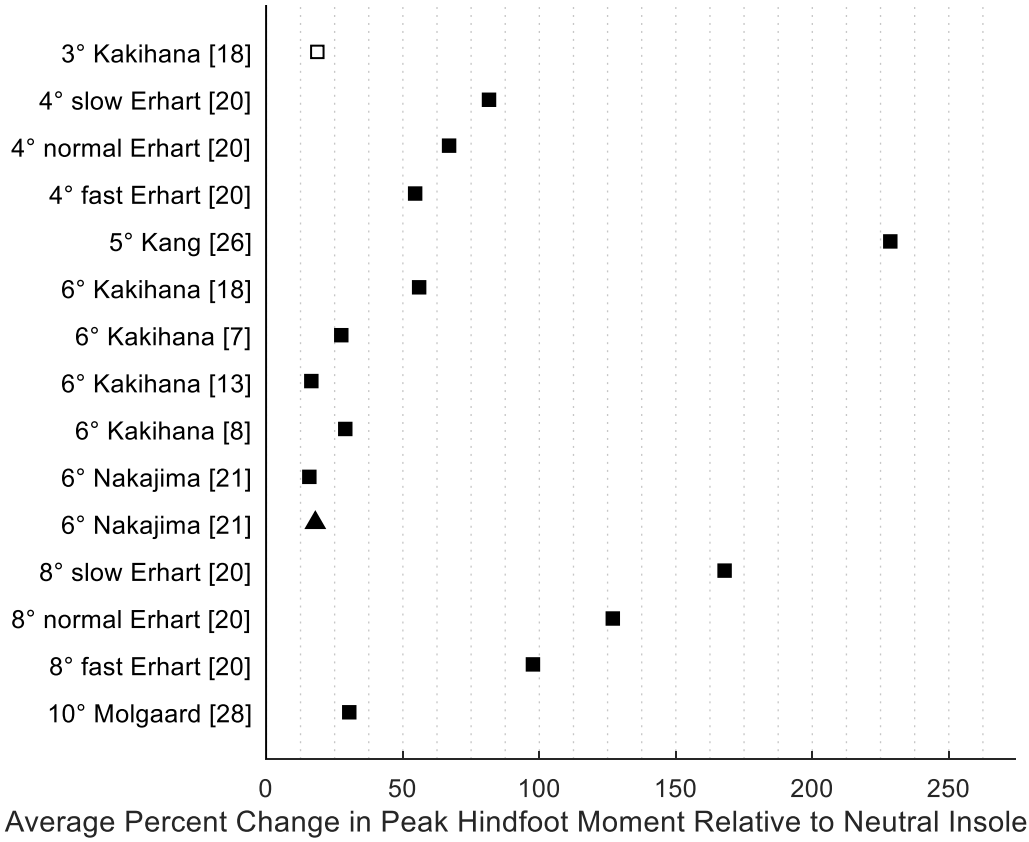

Figure 2.8. The increase in hindfoot moment relative to neutral insoles with healthy subjects. Squares represent typical wedges, and triangles represent LWIs with arch supports. A solid symbol represents a statistically significant change, while a hollow symbol represents a non-statistically significant change.

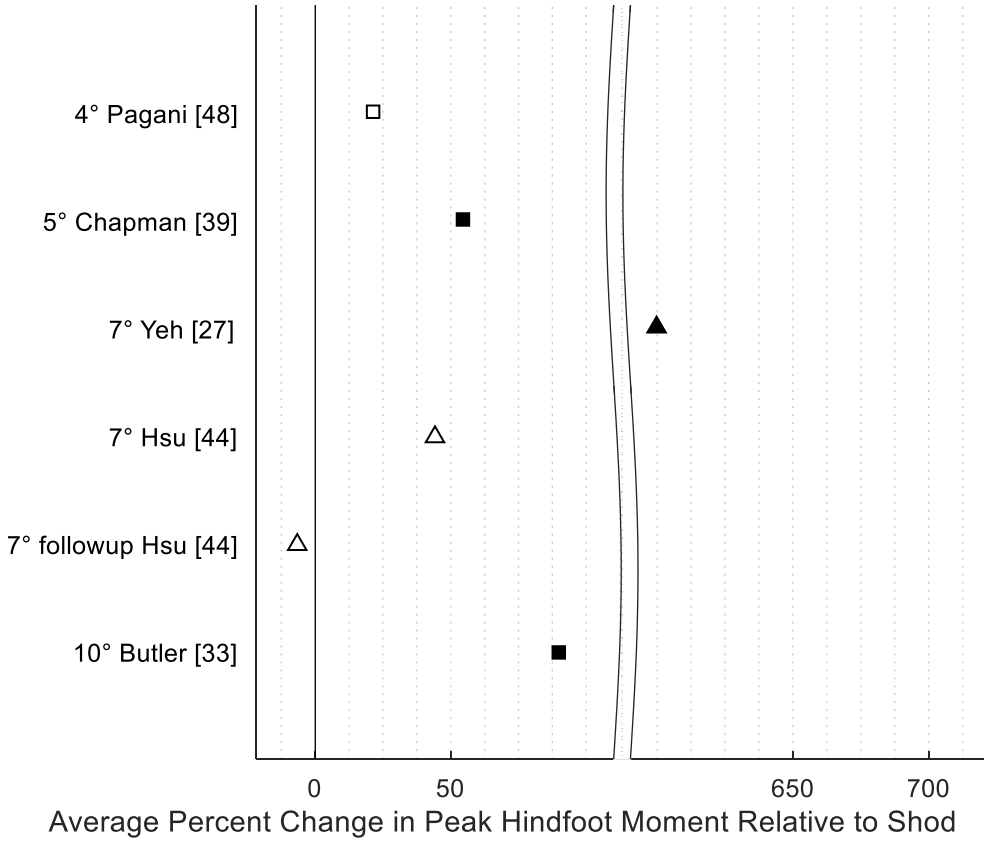

Figure 2.9. The percent change in hindfoot moment relative to shod with OA subjects. Squares represent typical wedges, and triangles represent LWIs with arch supports. A solid symbol represents a statistically significant change, while a hollow symbol represents a non-statistically significant change.

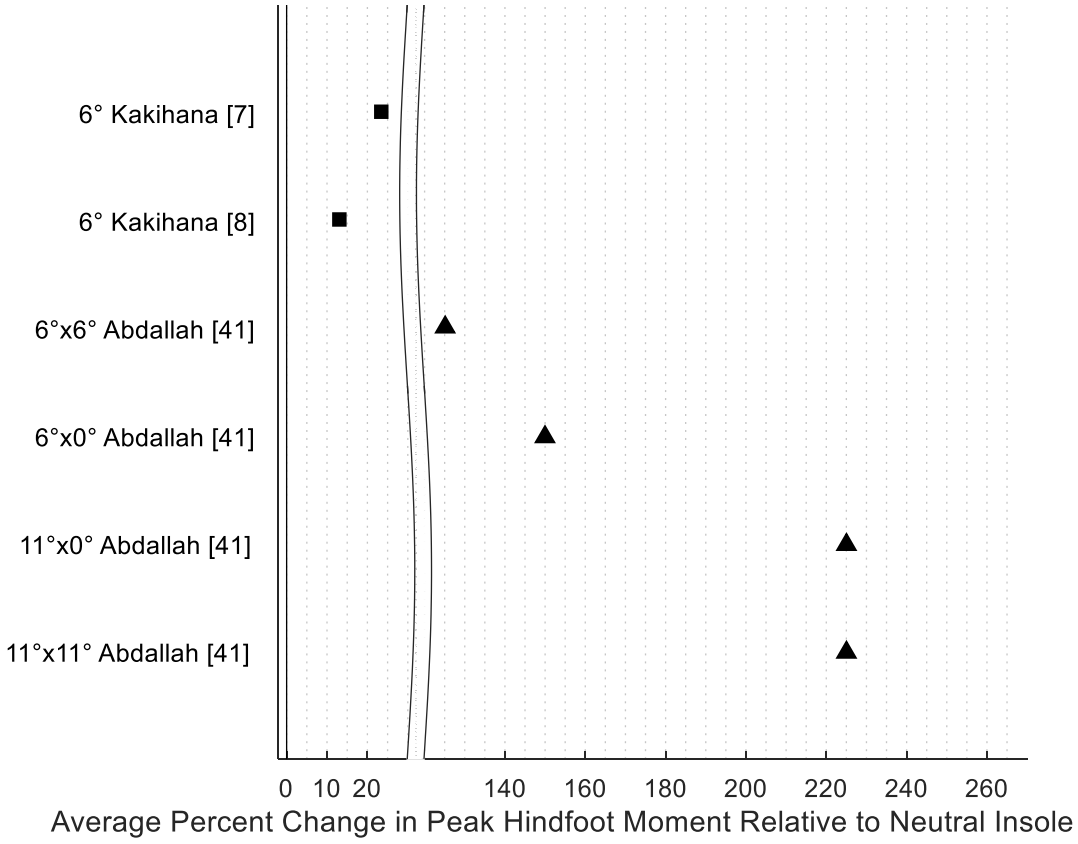

Figure 2.10. The percent change in hindfoot moment relative to neutral insoles with OA subjects. Squares represent typical wedges, and triangles represent LWIs with arch supports. A solid symbol represents a statistically significant change, while a hollow symbol represents a non-statistically significant change.

2.4 DISCUSSION

This review included 43 papers that contained healthy, OA, or both subject populations who were prescribed LWIs to determine how the insoles may reduce the biomechanical factors that relate to medial knee OA. The studies were split into four main groups based on population (healthy or OA subjects) and control condition (shod or neutral wedge). Four with studies with healthy subjects [15,18,25,29], seven with OA subjects[36,40,41,44,48,51,52], and one study

with both populations [22] did not report a significant decrease in EKAM with the prescription of LWIs. Two studies reported a decrease in hindfoot moment [15,44], and four studies reported a non-significant change in hindfoot moment [18,25,44,48] .

2.4.1 *Risk of Bias Assessment*

The majority of the papers were ranked as either moderate or high quality with 37 of 43 papers scoring 71% or higher. The external validity category was generally high, but most papers did not report the population from which the subjects were recruited. This reduced the ability to generalize results across populations. Internal validity was also generally high with most studies presenting the insoles in a random order, but most papers did not explicitly state whether the researchers were blinded to the conditions in data collection or processing. Blinding researchers to the insole condition during data collection can be difficult, but the data analysis could be blinded during processing. As many LWI studies have been completed, future research should include an a priori power analysis to estimate the population size needed for the variables of interest. This calculation was lacking in many studies, with the majority of studies not completing a power analysis.

2.4.2 *LWIs Reduce the EKAM*

The majority of papers published have shown a reduction in the EKAM for healthy and OA populations. Crenshaw et al. [17] reported a decrease in EKAM of 6.8% for a 5 degree wedge compared to a neutral wedge. This study also demonstrated the significance of the reduction in EKAM by using an analytical model to determine the force on the medial condyle with and

without a LWI. The model showed a significant decrease in medial contact force with the use of LWIs. Kerrigan et al. [31] demonstrated that the effectiveness of a LWI is not a consequence of the extra cushioning that may be provided the insoles but from the wedge angle itself. When using 3.175 or 6.35 mm thick neutral insoles, there was no significant reduction in the EKAM compared to shod. However, wedges of 5 and 10 degrees reduced EKAM by 5.3 and 8.3% from shod, respectively, indicating that the larger wedge was more effective. Hinman et al.[9,35–37] conducted multiple studies with OA subjects using 5 degree wedges, and saw an EKAM reduction between 5.2 and 11.9% for all studies.

Several studies have found contradictory results with a healthy population, which may be due to differences in the construction of the insoles. Five studies with healthy subjects did not show a reduction in EKAM [15,18,22,25,29]. Nester et al. [25] did not report a significant difference between a 10 degree LWI with an arch support and a shod condition. The insole used in this study had a 3 mm thick covering that was softer than the wedge material. The added soft material could change the effective wedge angle of the LWI, and possibly diminish its effects. Leitch et al. [22] did not find a significant reduction in EKAM for the 4 degree wedge condition, but did for the 8 degree condition. Kakihana et al. [18]did not find a significant reduction for the 3 degree wedge condition. Pagani et al. [29] did not find a reduciotn in EKAM with a 4 degree full length LWI. Telfer et al. [15] used 3D printed fully customized orthosess with wedging angles of 0, 2, 4, and 6 degrees. They reported a non-significant increase in first peak EKAM by 12.2, 6.3, 19.8 and 7.3 %, respectively, from the shod (i.e., no insole) control condition.

Seven studies with OA subjects did not have a significant decrease in EKAM [36,40,41,44,48,51,52]. Maly et al. [40] found non-significant reductions in EKAM of 2.1% for a 5 degree heel wedge and a 4.2% increase with an off the shelf orthosis. These results may be

attributed to the heel wedges used in this study are not as effective as full length wedges [36] and their population may not react as strongly to the LWIs since most of the population was either awaiting surgery or had other current treatments, which suggest a severe OA grade [34,52]. A study by Abdallah et al. [41], found non-significant reductions in EKAM by 9.1% with a six degree wedge and 0 degree contralateral wedge, and a reduction of 7.5% with an 11 degree wedge prescribed bilaterally. Medial arch supports have been shown to increase the variability in EKAM [53] , but did not significantly change the EKAM on average. This may be why the percent reducitons were similar to what is seen in other papers, but do not show statistical significance. The study by Pagani et al. [48]also had a non-significant 7.3% reduction in EKAM with a 4 degree wedge. Leitch et al. [22] did not find a reduction in EKAM with 4 degree LWIs but did for the 8 degree condition. The prescription of insoles should be specific to the patient, as the patient may need a higher degree of wedging to allow the insole to be more effective in reducing pain and EKAM, especially if they have advanced stages of medial knee OA.

Five studies had a barefoot condition[34,44,47,51,52]. Segal et al. [51] found an increase in EKAM relative to barefoot, along with Hsu et al. [44] at follow up. Jones et al. [47] found that barefoot reduced EKAM more than LWIs. Other studies by Kemp et al. and Kerrigan et al. [54–56] have found that subjects with or without medial knee OA respectively, walking with shoes tends have an increased EKAM compared to barefoot. Kuroyanagi and Shimada et al. [34,52] did find a reduction in EKAM which may be due to the larger wedging used in the studies.

Four studies differentiated between subjects with varying amounts of OA described by the Kellgren Lawrence scale[32–34,52] and four studies had a healthy and an OA population [7,8,22,42]. EKAM has been reported to be up to 79% higher for OA subjects[52]. Subjects with higher grade OA tend to have a higher EKAM[34,52]. Other studies have shown more modest

increases in EKAM of 7 and 24% with wedging [7,8], with one study showing no significant differences between the two populations, but showing a trend towards higher EKAM in OA [22]. Shimada et al.[52] found significant reductions in EKAM for subjects with K-L grade I ($p<0.043$) and II ($p<0.001$), and non-significant reductions in EKAM in K-L grade III ($p<0.058$) and IV ($p<0.086$) with the same size LWIs. Subjects with a higher Kellgren Lawrence grade also prefer a larger wedge angle as it has been thought to minimize pain while walking, determined by subject reported discomfort while conducting a lateral step down test [32,33,42]. Another study found similar results, with a reduction in EKAM of 7.7% for grade II and 6.3% for grade IV[34].

In general, a subject with a higher grade OA measured on the Kellgren-Lawrence scale has a higher EKAM, and OA subjects have a higher EKAM than healthy matched controls. The main purpose of LWIs is to slow progression and lessen the symptoms of OA by reducing the EKAM. LWIs are used to reduce the EKAM (typically by 5 to 10%) but may not reduce the magnitude measured in OA subjects to that of healthy subjects [7,8,22,27,52]. LWIs of the same angle do not decrease the EKAM of subjects with a higher grade OA compared to a lower grade. More severe OA subjects tend to choose higher angled wedges. A larger wedge angle may be necessary to reduce EKAM in subjects with a higher grade OA and to increase comfort at the knee.

2.4.3 *LWIs Increase Hindfoot Eversion Moment*

Most studies found a significant increase in hindfoot moment with the use of LWIs for healthy and OA populations. LWIs tend to increase the hindfoot moment due to a lateral shift in COP [7–9,18]. The percent increase in hindfoot moment tends to be much larger than the percent

reduction of the EKAM. This could be from the relative changes in the length of the moment arms, with the hindfoot moment arm having a greater percentage increase with wedging. The moments can be close to zero in the prescribed control condition which can create a large increase in hindfoot moment if there is any change [27]. Erhart et al. [20] found that the hindfoot moment increased with walking speed, and that it increased with an larger angled LWI.

Telfer et al. [15] found a decrease in hindfoot moment with custom LWIs ranging from 0 to 6 degrees in 2 degree increments compared to shod. Nester et al. [25] also noted a decrease in hindfoot moment with a semicustom insole. The foot may be cradled more in these two studies with a customized LWI and a LWI with an arch support with the added base layer. This may change how the foot interacts with the LWI compared to other studies that do not have an arch support, or a relatively small arch support.

There are mixed results as to whether or not LWIs increase the hindfoot eversion angle. Six studies found that the eversion angle increases [8,15,21,23,33,39], while four papers did not find a significant increase in hindfoot eversion angle [7,13,18,48], although one paper approached significance ($p=0.07$) [18]. Erhart et al. [20] noted a medial shift in the COP but still saw an increase in the hindfoot moment.

Two studies [7,8] found that OA subjects tend to have a smaller increase in hindfoot moment than in healthy age matched controls. This may be related to that OA subjects tend to have a more everted foot type than healthy aged matched controls [57]. The foot posture of the subject could change the effect of the LWI on the hindfoot and this should be studied further. The use of LWIs may cause more strain on the medial aspect of the foot with the increased hindfoot moment and should be cautiously prescribed to asymptomatic patients.

2.4.4 *Responders and Non-Responders to LWIs*

Thirteen papers specifically classified non-responders to LWIs [7–9,15,17,20,25,32,35,36,38–40]. Most studies tend to find that around 20% of the population does not have a reduction in EKAM with LWIs. Crenshaw et al. [17] had 2/17 healthy subjects with no significant change in EKAM and 4/17 subjects with an increased EKAM. In two studies by Kakihana et al. with OA and healthy subjects, only the OA population contained subjects that exhibited an increase in EKAM, with non-responders consisting of 15.3% [7] and 17.6% [8] of the OA subjects. Butler et al. [32] found that subjects with an increased EKAM had a much smaller increase in hindfoot angle than the responders. Contrary to what was found by Kakihana et al. [7,8], this study had 8/73 subjects with a medial shift in COP and 5/8 of those still had a reduced EKAM. Leitch et al. [22] found that all subjects had a reduced EKAM with the 8 degree wedge. During the 4 degree wedge condition one subject experienced an increased EKAM, and three others showed little change. Another study found that 15% of the subjects exhibited an increase in EKAM when the amount of wedging was self-selected through a lateral step down test [32]. Jones et al. [38] had 46% of the subjects as non-responders to LWIs, showing that almost half of the OA population did not receive any beneficial results from the insoles. This was the highest non-responder rate of all of all the studies reviewed. Studies in the future should classify responders and non-responders to the insole condition so that the effect or lack thereof can be classified properly.

2.4.5 *Dose Response to LWIs*

Seven papers used multiple insole heights[18,20,22,31,41], and in two of those the primary goal was to determine the dose response of LWIs [15,24]. The two studies consisting of an OA population had conflicting results: Abdallah et al. [41] used 6 and 11 degree wedges, and had no significant reduction in EKAM from a neutral condition when insoles were applied unilaterally or bilaterally. Kerrigan et al. [31] found that EKAM was reduced by 5.3% and 8.3% for 5 and 10 degree wedges, respectively, relative to a neutral insole. Kakihana et al. [18] used 0, 3 and 6 degree wedges with a healthy population and attached the insoles to the bottom of the subjects' feet with tape. The 3 degree wedge produced a non-significant reduction in EKAM by 8.9% and a significant reduction with the 6 degree wedge by 24.4% from the neutral insole. Leitch et al. [22] also found that a 4 degree wedge did not produce a significant reduction in EKAM but an 8 degree wedge did. Erhart et al. [20] saw a reduction in EKAM of 7.6 and 12.6% in healthy subjects with a 4 and 8 degree wedged shoe sole.

Telfer et al. [15] used a variety of medial and lateral wedges (ranging from 10 degrees medial to 6 degrees lateral in 2 degree increments) and found a trend that for every 2 degree increase in lateral wedging there is a 1.4% reduction in EKAM. Tipnis et al. [24] used 0 to 12 degree lateral wedges in 2 degree increments, and found that EKAM decreased for all wedges, with less change with increased wedging after 6 degrees. The reduction in EKAM was 6.4% for a 2 degree wedge, 10.3% for 4 degree and 12.8% for 12 degree. LWIs may have a diminishing return in the reduction in EKAM with wedging greater than 6 degrees. Further, subject comfort tends to play a role: greater than 10 degrees tends to become prohibitively uncomfortable [31]. The degree of wedging may play a role in how many subjects respond favorably to LWIs, as some subjects may need larger wedging for the EKAM to change [7,18,20].

2.4.6 *Center of Pressure*

The COP tends to shift laterally in healthy and OA populations by around half a centimeter due to lateral wedging. This shift is one of the mechanisms that is thought to reduce the moment arm acting on the knee, thus reducing the EKAM. Thirteen studies noted an effect on the COP from the prescription of LWIs. Six used a healthy population [13,18,20,23,29,44], four with both healthy and OA subjects[7,8,22,27] and four with only OA subjects [9,39,40,51]. The lateral shift in COP tends to be from 0.47 to 6 mm with LWIs[23,51]. Hinman et al. [9] found a significant correlation between the peak EKAM and the lateral change in the COP. In one study using healthy subjects the hindfoot moment arm increased from 54 mm to 58 mm with the use of a 6 degree lateral wedge insole compared to a neutral wedge. This was accompanied by a non-significant change in hindfoot eversion angle and the authors hypothesized that there was a lateral shift in COP (as it was not directly measured)[18]. A study by Erhart et al. [20] did not measure COP directly but bisected the foot medially-laterally and tracked pressure on each half. They found an increase in medial pressure of the foot with the use of a 4 and 8 degree LWIs but still found that in healthy subjects the hindfoot moment increased, and the EKAM decreased. They also determined that the trend of medial-to-lateral heel pressure, or the shift in COP, can predict the change in EKAM. Two other studies also noted that the lateral excursion of the COP could predict the reduction in EKAM [7,18]. Hsu et al. [44] noted that the immediate lateral shift in the COP was maintained at a 6 week follow up.

The three studies that had only OA subjects produced mixed results. Maly et al. [40] found that the COP had no significant lateral shift but noted an anterior shift with the use of a 5 degree LWI heel wedge. Chapman et al. [39] found a significant lateral shift in COP by 4 mm with full-length 5 degree LWIs. Another study by Hinman using full-length 5 degree lateral

wedge insoles found that the center of pressure shifted laterally by 3.4mm [9]. Kakihana et al. had OA and healthy subjects and [7,8] noticed that the OA subjects who increased their EKAM had a medial shift in COP. This was also seen in conjunction with a smaller increase in hindfoot moment and smaller decrease in EKAM in OA subjects compared to healthy. Leitch et al. [22] also noted a lateral and anterior shift in COP, with a reduction in EKAM in healthy and OA subjects.

2.4.7 *Medial Arch Supports*

An increased hindfoot moment can lead to feelings of instability and lack of comfort [21]. A medial arch support is added to an LWI to reduce the hindfoot moment while still allowing a reduction in EKAM. Sixteen studies used wedges with a medial arch support or customized insoles [15,21,23,25,27,30,32,33,38,39,41,44–47,47]. Five studies [21,23,38,39,47] contained LWIs with and without arch supports found that the reduction of EKAM was not significantly different between wedging with and without an arch support. Nakajima et al. [21] tested how the EKAM and hindfoot moment changed using flat and wedged insoles, each with and without an arch support. The hindfoot moment was increased with wedging, but was not significantly different with or without an arch support on the neutral or wedged insoles. Further, hindfoot eversion was not significantly different between the LWI and the LWI with an arch support. Similarly, Jones et al. [23] found that the EKAM is unaffected with the use of arch supports and a LWI with an arch support both conditions increased the hindfoot moment by a similar amount as the LWI compared to a neutral orthosis. Another study by Jones et al. [38] observed EKAM non-responders both with and without arch supports: some subjects had an increase in EKAM in one of the two wedge conditions, and others increased EKAM in both wedge conditions. Butler

et al. [33] also found that LWIs with arch supports reduced EKAM and increased the hindfoot moment, and hindfoot angle in OA subjects with a self-selected wedge angle. In another study the hindfoot eversion changed around 1 degree due to wedging[23] which may or may not be clinically significant. Telfer et al. [15] used 3D printed fully customized orthoses and found that compared to shod all EKAM's were greater with wedging ranging from 0 to 6 degrees laterally; EKAM reduced as the wedge angle became greater, but the hindfoot moment decreased for all conditions compared to shod. Two studies did not find a significant decrease in EKAM using a LWI with an arch support in an OA population with one finding a decrease in hindfoot moment, the other finding a greater hindfoot moment with a larger wedge angle with arch supports [25,41]. A study by Hinman et al. [53] found that medial arch supports did not significantly change the average EKAM but did highly change individuals peak EKAM. Arch supports may need to be prescribed on a per subject basis. The insoles may increase comfort, as more of the foot is cradled by the insole, which in turn may make the patient more compliant in their prescription. Ultimately, the different protocols and wedge construction may have an impact on the hindfoot moment and more studies should be completed to evaluate the kinematics and kinetics of the hindfoot with and without arch supports.

2.4.8 *Pain Relief*

Eight studies conducted biomechanical analyses while measuring pain[27,30,35,38,39,45,49,51]. Pain was quantified using one of three clinical assessments during gait analysis: a) the visual analog scale (VAS), b) the Western Ontario and McMaster Universities Osteoarthritis Index (WOMAC) pain and function scores, and c) the knee osteoarthritis outcome score (KOOS). The majority of the biomechanical trials demonstrated an immediate reduction in pain with the

prescription of LWIs. One study that measured the immediate effects of LWIs on pain found that the OA subjects had a significant reduction in pain measured using VAS, while the neutral insoles did not [27]. Jones et al. [45] found that WOMAC scores decreased with the use of LWIs after two weeks of use compared to baseline and no significant change in stiffness while pain was significantly reduced as measured on the VAS. Hinman et al. [35] found that subjects' pain, rated on the WOMAC scale was reduced by 20% after 3 months of using a 5 degree LWI. There were also correlations between larger reductions in EKAM at baseline to less pain reported at the 3 month follow up. Jones et al. [38] conducted a similar study but only measured immediate response and included LWIs with and without medial arch supports. They found that pain only decreased with the use of arch supports, and did not differ between subjects who had a reduction or increase in EKAM. This study only measured immediate outcomes of using LWIs and also found that comfort of the LWI in the shoe and knee pain reduction were highly correlated. Another study by Jones et al.[47] also found an immediate reduction in pain with the use of LWIs with medial arch supports, but no reduction in pain in a typical LWI without arch supports, and the wedges were determined to be more comfortable than the subjects' own shoes. Segal et al. [51] did not find a reduction in pain measured by the VAS, but did have a significant reduction measured by the KOOS with the subjects recording pain every day for two weeks while using the insoles. Longer clinical trials may serve as a better indicator of the effectiveness in reducing pain due to the novelty and limited time that the subjects spent with the insoles of these studies. Arazpour et al. [49] found a reduction in pain after six weeks of LWI use. On average longer term studies show a small, and potentially clinically relevant, reduction in pain when compared to a no insole control condition. The 5-9% reduction in the EKAM may not reduce the load enough to lower pain, even with the thousands of steps taken per day, as the

muscle co-contraction and other forces throughout the knee may be too great for a clinically significant reduction in pain.

2.4.9 *LWIs Effectiveness Over Time*

Five studies completed biomechanical studies at both baseline and a follow up visit [37,42–45]. One study by Jones et al. [45] reported that after two weeks of LWI use, the EKAM was reduced compared to a baseline of no intervention. After a two week washout period the EKAM and kinematics were not significantly different than before the intervention showing that the beneficial effects will diminish without use. An article published by Hinman et al. [37] found that the five degree LWIs in this particular study do not deteriorate and maintain their benefits after one month of use. Two studies that tested LWIs at baseline and after 6 weeks of use also found that the EKAM was reduced by a similar amount immediately and at follow up [43,44]. The longest study was conducted by Barrios et al. [42] who found that at baseline the EKAM was reduced by 9% compared to a neutral insole condition and after a year of use the EKAM experienced a similar reduction of 8%.

2.4.10 *Methodological Differences*

The studied insoles varied by length, wedging angle, density, and hardness. The length of the wedging has been shown to affect the magnitude of reduction in EKAM, with a full length insole producing a reduction in the first-peak EKAM by 4.4% more than a heel wedge [36]. Shimada et al. [52] used a large wedge angle and showed a significant reduction in EKAM for moderate Kellgren-Lawrence grades (I and II) but not severe grades (III and IV). Maly et al. [40] also used

heel wedges for subjects who were candidates for knee surgery, and did not find a reduction in EKAM, as the degree of wedging may not have been enough to create a significant difference. Leitch et al. [22] found that EKAM reduced with the use of heel wedges, and the EKAM reduction was not significantly different between the OA and healthy populations for an 8 degree wedge. While heel wedges may not be the best type of insole to reduce EKAM, a wedge angle that is sufficiently great may provide some benefit; however, similar benefits may be achieved with a full-length insole of lesser wedging. More about wedge angle can be viewed in the dose response section. Another study by Segal et al. [51] also used heel wedges with OA subjects compared to barefoot and did not find a significant change in EKAM. The use of a full length wedge has been shown to be better able to reduce EKAM the over the whole stance: heel wedges may not be as effective at reducing the average EKAM or the first peak EKAM as full length wedges, and do not reduce the second peak EKAM.

We are unaware of a study that compared the effect of hardness or density values of wedges that have been used. The hardness scores of the LWIs are not consistently reported in the same scale, and are reported to be about 55 (Shore A scale) and 70-90 (Rockwell scale). The different hardness values for the materials may allow for different deformations of the wedge, especially if a softer base layer is placed over the wedge. If the entire surface of the wedge is not uniformly loaded, the wedge deformation could change the effective wedge angle. The load tends to shift laterally [20,22] possibly causing more deformation on the lateral aspect of the LWI, which further changes the effective wedge angle. Better reporting of the wedge material, through material property testing and through composition description.

Further, the type of shoes worn varied considerably between the studies and often within a study. There are many different laboratory shoes used for testing, with some studies allowing

subjects to use their own shoes, which may vary in materials, construction and wear. This may play a role in the increase of the hindfoot moment and change in EKAM, making some studies hard to compare unless the reported laboratory shoe construction is similar between studies. Four studies did not use shoes, but rather had the insoles taped to the bottom of the subjects' feet [7,8,18,21] , including Kakihana et al. [7,8,18] which had the lowest reported EKAM of the all of the reviewed studies. The shoe could offer extra support to the insole to reduce its deformation when worn. The addition of shoes and even the type of shoe could increase the moment arm about the knee, thus increasing the moment [55,56].

Some subject specific variables such as femorotibial angle and OA grade have an effect on the EKAM. A more varus femorotibial angle increases the moment arm length which in turn increases the moment[58–60]. The manner in which different populations walk may also have an effect on the EKAM, as walking speed, and toe out angle change the EKAM [9,20]. A larger population would be helpful in washing out the influence of subjects with extreme femorotibial angles; alternatively, this variable could be controlled for in subject recruitment.

The measurement equipment and procedure is inconsistent between studies. One of the primary factors for changing EKAM is moving the COP laterally, and some studies have reported significant changes in EKAM with a shift of 3.5 and 6 mm [9,23]. That is, the differences in COP needed for a significant result to be found are very small, amplifying the chance of a null result solely due to limited precision in the COP measurement. Also, most of the studies used optical motion capture to record the kinematics of markers placed on the shoe or skin at various bony landmarks. Determining kinematics about the ankle may be difficult due to soft tissue artifact. The camera count for most studies was different as was the marker configuration, marker count and kinematic model. As a result, the definition of the body

segments from the markers may not be the same and different models could be used with different assumptions about skeletal geometry. This could influence the precision or sensitivity of the data in post processing and particularly complicates comparing results across different studies. The procedure for how subjects walked may also change the EKAM reported. Most studies controlled for walking speed and had the subjects walk either at a prescribed speed, or a self-selected (but constant between trials) speed. The EKAM can be around 9% greater for a self-selected fast walking speed than for a self-selected slow walking speed [20]. A paper by Shimada et al. [52] has the highest EKAM reported around 1 Nm/kg. Their subjects were instructed to walk with their arms crossed in front of their torso as to not block optical hip markers with their hands as their arms swung during gait. Such a modification to gait could cause the subject to walk in an unnatural gait pattern that could affect the EKAM or cause the center of mass to follow an unnatural trajectory. The results for the hindfoot moments are difficult to compare between laboratories because of the shoe condition and marker configurations. Some studies have holes cut in the shoes for makers to be attached directly to the skin, others had the insoles attached directly to the feet without shoes, and lastly some studies applied the markers directly to the shoes themselves.

These factors make it difficult to compare absolute magnitudes of EKAM between studies that were conducted using different protocols and in different research labs. A better comparison would be to use the relative changes between the control condition and the wedged condition. Special care still has to be taken since the control condition could be a neutral insole, barefoot, or shod. The shod and neutral insole conditions could be similar in EKAM magnitude, as seen by Kerrigan et al. [31], or very different, as seen by Telfer et al. [15]. Later studies have classified the subject populations into a group with reduced EKAM (responders) and a group

who do not have a reduced EKAM (non-responders) when using LWIs. Earlier studies that do not make this distinction may report a lower reduction in EKAM, as the responders will be pooled in with subjects which have an increase in EKAM. The methods of each paper reviewed should be compared to see how the data collection may be different, and conclusions based on the results should be drawn carefully because of inconsistencies in testing equipment, multi-segment models, subjects, and interventions.

This review reported the biomechanical effects of LWIs on the EKAM and hindfoot moment compared to multiple control conditions. From this review the following conclusions can be drawn: (i) LWIs reduce the EKAM on most healthy and OA subjects, but about 15% to 20% of the population who may have an unchanged or even increased EKAM, so care should be taken in the prescription of LWIs, (ii) LWIs on average increase the hindfoot moment; these effects have not been extensively studied short or long term, (iii) Wedge construction can determine the effectiveness of the LWI, which should be full length and at least 4 degrees to provide a reduction in EKAM but may have diminishing effects greater than 6 degrees, (iv) The shift in COP can be used to predict the reduction in EKAM, and is the highest correlated parameter to the reduction of the EKAM.

2.4.11 *Limitations to the Review*

All of the values presented in this article were calculated by the reviewers from the data given in the articles. Some of the data needed for the review was only presented in figures, and was estimation from the figures using interpolation. This may cause a discrepancy between the reported values in the review and the actual papers.

2.4.12 *Conflicts of Interest*

The authors have no conflicts of interest.

Chapter 3. BIPLANE CONTROL SYSTEM

The purpose of this document is to act as a reference manual for the biplane fluoroscopy system located at the VA Puget Sound Health Care System in Seattle, WA. This system is used for high speed motion capture of fluoroscope images of static or dynamic objects. This manual is divided into (9) sections that are titled (1) Introduction (2) DAQ Version 1.0.0 (3) DAQ Version 2.0.0, (4) DAQ Version 3.0.0, (5) Hardware and Specifications, (6) Validation Procedure and Theory, (7) Daily Use, (8) Future Improvements, and (9) Appendix.

3.1 INTRODUCTION

This software was created to upgrade the ability to control the biplane system, implement new safety features, and capture additional data that better allows for analysis of the gait cycle. The most prominent improvement is the ability to measure strain data to detect when the foot is in contact with the walkway, i.e., to determine heel strike and toe off. Heel strike and toe off are two important times during the gait cycle, marking the beginning and end of the stance phase. The time difference of heel strike and toe off give the duration of stance phase and allow the researcher to quantify occurrences as a percentage of stance phase which is standard in the biomechanics community. Pilot testing has indicated that there is no clean way to determine when the foot is in contact with the ground using the biplane fluoroscopy images alone, so this independent measure was used. The whole foot may not fit in the small field of view, so the strain gage would also allow heel strike or toe off to be determined when part of the foot is not imaged. LabVIEW was utilized as well as hardware from National Instruments to implement these upgrades due to the flexibility and versatility of the software and hardware. A real time (RT) chassis and field programmable gate

array (FPGA) were utilized for their determinism and ease of data collection given the large amounts of data and high sampling rates.

3.1.1 *About the System*

The primary purpose of the biplane system is to collect high speed X-ray images of the foot during over-ground gait trials. The subject starts at the far end of the 4.9 meter walkway which has railings on both sides and one end (see Hardware and Software Specifications for more detail). The other end is enclosed by a wall. The subject begins walking, breaking the infrared gate number 1 (IR gate) positioned about 0.5 meters from the start. Both cameras start record images, and after a short duration, the fluoroscopes begin firing. All of the IR gates are attached to the railing about waist height, with the switch to the subject's left, and the reflector to the subject's right. The subject then passes through IR gate 2 which is approximately 1.7 meters from IR gate 1. The subject steps onto the carbon fiber floor plate that is X-ray transparent. The gait trial concludes after the subject takes another step out of the field of view and crosses IR gate 3 which is 1.1 meters from IR gate 2. The zero image frame is marked and the fluoroscope turns off. The center of the field of view of the X-ray imaging is located approximately at the center of the plate. There are two X-ray sources that straddle the walkway about waist height. The sources' positions are biased toward the end of the walkway and face toward the start of the walkway. The image intensifiers (IIs) are under the plate with their positions biased toward the start of the walkway, facing toward the end of the walkway so the II screen is normal to the X-ray source. The positioning of the source and emitter is slightly asymmetrical aimed through the floor to allow better imaging of the foot. The high speed cameras are attached to the back of the IIs through a custom fixture. The IR gates are used as inputs to the system to start and stop data collection, initiate the output signals, fire the fluoroscopes, and

pretrigger/trigger the cameras. The fluoroscopes need an "on" signal to fire, and the pretrigger and trigger signals for the camera need a digital edge (rising or falling, set by user in camera software). The fluoroscopes should fire just before the subject is in the field of view until the subject leaves the field of view to capture the end of swing phase and all of stance phase. Both cameras start recording when they receive the pretrigger signal. They have a circular buffer so that they can only record the previous 1996 ms with their current settings. They start recording when the subject passes through IR gate 1. Both cameras receive the trigger signal when the subject passes through IR gate 3 and set the current frame to frame zero, and capture the specified amount of post trigger frames. The cameras should stop recording within 1996 ms after the first frame of interest is captured so no important image data are lost. Most gait trial image sequences last a little more than half of a second. The data collected during a trial consists of two sets of high speed fluoroscope images (one from each camera), a spreadsheet file with all of the input and output signals of the system, and the strain of the X-ray transparent plate. The inputs and outputs are the signals to/from the IR gates, fluoroscope firing, and the camera pretrigger and trigger. The strain is used to determine when the foot was in contact with the plate.

3.1.2 *Workflow*

The LabVIEW programming environment is graphical, and is based around arranging graphics icons on a graphic "block diagram". This diagram consists of various types of "loops" (while loops, for loops, case structures, etc.) that are analogous to programming constructs in traditional text-based programming languages. Contained within each loop are various "blocks" which are the analog of functions connected by "wires" which represent data flow, the analog of variables. This layout is designed to resemble traditional wiring diagrams used in electronic design. Programs are

organized into “virtual instrument” files (VI), consisting of functions (subVIs), and a collection of VIs constitute a project.

The system is comprised of three devices, the user interface (UI), the RT and FPGA. The UI code was created from a consumer/producer template, the RT from a queued message handler template and the FPGA from a state machine template provided by National Instruments in the 2015 LabVIEW package. The architecture uses a message system to communicate within and between the three devices. Each device has its own defined and limited job. Some of the VIs were provided by the template were deleted, while some stayed in their original form, and others ranged between slight and heavy modification. Many new VIs were created for the specific use on this system and could be used in other applications due to their modularity. There were many phases of building the current system after the template was stripped of most of its components; this design process will be described below.

The first task was simply to set up the message streams between the UI loops within the UI, then from the UI to the RT, and then between the RT and FPGA. Once data could be transferred between the three systems, a single case (a defined state that executes one of multiple tasks) was created to make the FPGA collect a specified amount of data at a specified start time for a specified duration. (This case is later denoted as “Static Capture” on the FPGA.) To do this, additional cases were added to the FPGA, latches were created, a single pulse square wave generator was created, and the messaging structure increased to contain more cases. After a single static case was created and was working as expected, three more static cases were created, for capturing static data during various calibration states and during static subject trials. A Dynamic Capture case, to be used for subject gait trials, was then created for when both the start time and duration of data capture would be unknown. The message structure was again increased, new latches were created, new logic VIs

were implemented, and a new case on the FGPA was created. The system was then tested for temporal accuracy through validation tests and human subject testing began.

3.1.3 *Acronyms*

DAQ - Data Acquisition - Referring to the collection of signals from one or more measurement devices.

DMA - Direct Memory Access - The data transfer method between the real time system and the field programmable gate array.

FIFO - First In/ First Out - The order in which data are inserted and removed from a queue or buffer, mainly referring to the message scheme between loops or devices, and the buffer used in the DMA.

FPGA - Field Programmable Gate Array - One of the two devices located in the real time chassis and is an uncommitted logic array configured by a compiled bitfile. The term is also used to refer to the LabVIEW file used to configure the logic array.

IR gate - Infrared Gate (1,2,3) - Refers to one or all three switches that are used to trigger the system. They are located on the underside of the railings on the walkway.

PC - Personal Computer - The desktop computer in the biplane laboratory.

RT - Real Time - The second of the two devices located in the real time chassis. It runs a Linux operating system. The term is also used to refer to the LabVIEW code that runs on the system.

UI - User Interface - This term is used to refer to the desktop computer where the user interacts with the biplane system. It also refers to the LabVIEW code run on the desktop computer.

VI - Virtual Instrument - LabVIEW's version of a programming function. They contain inputs and outputs (control and indicator in LabVIEW terminology), used to collect, process and store data. Virtual instruments can consist of many subVIs, or many subfunctions used as building blocks.

3.1.4 *Input Signals*

IR gates 1,2,3 - The voltage across the respective IR gate. Gates are normally open, with a 5V signal, and when the beam is broken drop to 0V. They are used for timing of the system during gait trials.

Strain - The voltage difference between the two sides of the Wheatstone bridge in the National Instruments bridge completion module. The voltage is not calibrated to measure the actual strain of the plate.

3.1.5 *Output Signals*

Fluoroscope Fire Signal - The signal controlling whether or not the fluoroscopes to emit X-rays for image capture.

Pretrigger - A falling edge signal (between the camera signal hot and ground wires) used to start the image capture of both of the high speed cameras.

Trigger - A falling edge signal (between the camera signal hot and ground wires) used to mark the zero frame of the image capture.

3.2 DAQ VERSION 1.0.0: ARDUINO

Version 1.0.0 consisted of hardware to control the biplane system. Only the theory will be explained since the system is currently in a non-working condition, and the user should have enough information to use the system through the theory alone.

3.2.1 *User's Theory*

The previous system utilized Arduino (Arduino, Italy) hardware to control the timing to all of the components of the biplane system, and used the Phantom software on the PC to record and change image settings. The hardware had two analog input signals which are now known as IR Gate 1 and 3's signals. These gates are at the very beginning and end of the walkway. The gates maintained 5 V until the IR beam was broken and then the gates moved to the closed position and changed to 0 V. The outputs to the system were the pretrigger, trigger and a signal to fire the fluoroscopes and their timing was based on the inputs from the IR gates. All of the outputs were switches that completed their respective circuits.

When Gate 1 was tripped, an input signal was sent into the Arduino. In response, the Arduino hardware sent out a pretrigger signal to both cameras simultaneously to start recording images. Another output signal was sent to the fluoroscopes from the Arduino after a specified delay; this delay was set by an external dashpot. The dashpot created a delay with a longer delay when the dashpot was positioned more clockwise. The normal setting for it was about halfway through its range of motion, which was about a half second delay. With this setting the fluoroscopes would not fire well before (> 0.5 seconds) the subject was in the field of view. The delay was meant to limit the amount of radiation exposure to the subject and staff in the biplane fluoroscopy room.

When Gate 3 was tripped, a second input signal was sent to the Arduino. The Arduino then sent out a trigger signal to both cameras simultaneously. This trigger signal marked the zeroth frame; the cameras then recorded the specified amount of post trigger frames (10 frames at 1000 Hz) and then stopped recording. All of the frames could then be viewed and saved. The fire fluoroscope signal was also reverted back to the off state so the fluoroscope would stop firing.

The Arduino hardware was also set up to control the biplane system without tripping the IR gates. This was useful for taking images for the distortion correction and 3D localization of the system during the calibration routine, and for taking static images of a subject. The Arduino acted in the same manner as previously explained, but instead of the two IR Gates controlling the input signals there were two buttons. These two buttons were wired in parallel with the gates, so that if either one was tripped the system behaved the same. Pressing one button (parallel to IR Gate 1) started the fluoroscope firing and sent the pretrigger signal, while pressing the other button (parallel to IR Gate 3) sent the trigger signal and stopped the fluoroscope. In between button presses, the fluoroscopes fired and recorded the desired amount of frames. The IR gates did not have to be tripped in that order to start firing; either could be tripped first.

After the subject tripped IR Gate 3 or the user pressed the button to stop the fluoroscopes from firing, a reset button was pressed to reset both of the gates. Care was taken as to when this button should be pressed. If it were pressed before the subject was back to the starting area for a walking trial and they were to trip an IR gate, the fluoroscope would then fire again until the other gate was tripped or the button on the Arduino associated with the other gate was pressed. A manual capture fluoroscope button was also intended, but never fully implemented.

There were four LEDs on the face of the Arduino to indicate to the user which IR gates have been tripped, whether the fluoroscope was on, and if the camera was on. With the gates tripped, fluoroscope on and camera on, all of the LEDs were lit up.

Figure 3.1. The Arduino control box housing the microcontroller with controls and indicators on the top to manipulate the system.

On the side of the Arduino there were three switches to arm the fluoroscopes, cameras, and timing lights. Flipping them up allowed the output signals to leave the Arduino and change the state of the respective component. Also on the same side was the dashpot knob that could be tuned to adjust the fluoroscope delay after tripping Gate 1; a piece of paper indicated an empirically determined delay that worked reliably. On the front of the Arduino case were five BNC female connections for the two inputs and three output signals.

3.2.2 *Update for Arduino System*

The Arduino hardware is currently not in a working condition. It was in use when lightning struck the building, causing a power surge in the room. The Arduino hardware shorted with the simple surge protection equipment that was in use. A preliminary visual inspection could not determine what component in the Arduino failed making the whole device unusable. A more in depth inspection has not been completed since the system will not be used in the future.

3.3 DAQ VERSION 2.0.0: ARDUINO AND LABVIEW

3.3.1 *Design History*

One of the major disadvantages of the Arduino system was the inability to easily add additional inputs to the system, especially those that require bridge completion (such as strain gages), without additional hardware and a likely redesign of the system. Rather than upgrade to another Arduino-based system, it was decided to pursue a National Instruments-based data acquisition system to allow for a more versatile control of the system and to provide a better platform for future upgrades.

There were two phases in the creation of this software. In the first, the NI hardware was used only for recording signal data, including both the strain data and the Arduino input/outputs (before the lightning strike). The Arduino continued to drive the entire system. This phase was completed in two ways, the first used basic elements and created a fully customizable program (v2.1.1), and the second relied heavily upon LabVIEW's built in functions (v2.1.2). In the next version, v2.2.1, the NI hardware measured all analog inputs and outputs from the Arduino and fired the fluoroscopes, while the Arduino continued to control the camera pretrigger and trigger signals as before. This was done to consolidate more of the signals to one piece of hardware to simplify data collection. All phases of software v2.0.0 utilized a single LabVIEW VI in LabVIEW 2013 (StrainGagePlusArduino.vi). The NI cDAQ-9178 data acquisition chassis was used to capture data with the NI-9201, NI-9263, and NI-9237 modules for analog input, analog output, and bridge completion for strain respectively.

The major improvement afforded by using NI hardware and LabVIEW was the ability to collect strain data that showed when an object made contact with the X-ray transparent plate. It also collected data for all of the other inputs and outputs of the system as version one did not save

data for post processing. This allowed for finer tuning of data collection parameters, and further logged the signal data to file for later post-test analysis if desired. This software was not made into a long term solution and was never developed further than a prototype. The timing results from a validation test and consultation with an NI representative revealed that the system would not be able to be as temporally accurate as was needed for a gait trial data collection (i.e., the ability accurately synchronize the inputs and outputs of the system to within 1ms).

As this is a deprecated system, no further details into those VIs will be given here; the reader can explore the relevant VIs and with the explanations given in the Developer's Theory section should be able to determine how to use the program.

3.3.2 *Developer's Theory*

Phase one (v2.1.0) captured the inputs and outputs of the Arduino, as well as recorded strain data of the X-ray transparent plate. The first iteration (v2.1.1) utilized basic functions to create a data acquisition task. To do this, the LabVIEW program first ran an initialization sequence to configure the measurements to start at the same time. The tasks (data streams) were defined, along with the sample clock and the start trigger for both data reads (i.e., input sampling). One data read consisted of all the signals into and out of the Arduino, and the other was for the strain. The two data reads were separated due to the need to synchronize time clocks between the separate pieces of hardware used to conduct the two reads. The tasks were set up in a master/slave configuration, with the slave starting first. The slave task would be in wait mode until the master task started and both would start when the master was triggered.

Following the initialization sequence, there were two read VIs to collect data of all the analog signals (in and out of the Arduino) and the strain gages. The data collected went through

some logic circuits and was saved into arrays. The logic was to determine when the values were above or below a threshold to denote when a signal was considered on or off. That is, the analog input data were converted to Boolean data indicating the state of the various signals. The data collection and logic occurred in a single while loop. After some testing, the software developed in iteration one was unable to produce the temporal accuracy needed in pre-validation trials, and so iteration two was developed.

The next iteration of the software (v2.1.2) was built to collect all of the signals to and from the Arduino and the strain gages, and heavily relied upon the premade VIs in LabVIEW. The thought behind changing from basic elements to LabVIEW's prebuilt software was that there may be some other logic circuits incorporated in the prebuilt LabVIEW functions that was not implemented in the custom software that may speed up data collection and organize the data better. The setup of this software was much simpler since most of the basic elements used before were incorporated into the prebuilt VIs. There were no initialization steps. The data were read and the same code was used for thresholding. After the data collection, another prebuilt VI was used to save the data. The validation tests described in Section 4 utilized the prebuilt functions.

While the v2.1.2 was implemented, v2.2.1 of the software was being created in parallel, and was only partially built before it was abandoned. It read all of the signals that went to the Arduino and controlled the fluoroscopes, but lacked the ability to read strain and send out the pretrigger and trigger signals. This version (v2.2.1) was abandoned due to the system's inability to fully complete two read VIs (v2.1.2 validation) within the required temporal accuracy. The final iteration of such a system would contain five total VIs (two read VIs and three write VIs) to monitor and control all of the signals; as the system could not maintain the accuracy needed with only two of the five VIs that would be implemented, it was not developed any further. v2.2.1

followed a similar programming flow as the v2.1.1 with the customized software built with basic functions. It started with an initialization, but then it used one read VI and one write VI instead. The write VI wrote a single square wave pulse to fire the fluoroscope for a predefined duration at a specified time.

During the validation stage, it was found that there were latencies between the multiple input signals that were unacceptably large; namely they would not allow us to achieve the goal of 1 ms accuracy in determining stance phase. After extensive testing and consultation with National Instruments, it was decided that our performance requirements exceeded the performance specifications of the NI hardware used in v2.0.0. Accordingly, we transitioned to a LabVIEW system using real-time control. This is the present system, and accordingly the most time will be spent on this section moving forward.

3.4 DAQ VERSION 3.0.0: LABVIEW RT AND FPGA

A RT system, utilizing a FPGA was purchased to address the deficiencies in the prototype LabVIEW system. This system was designed to accurately and precisely record and control all of the inputs and outputs of the biplane system. The control system was designed with the following specific goals:

- Implement the strain gage method for contact detection, synchronized with the other inputs, and operating deterministically, i.e., the timing of inputs and outputs can be controlled with high precision (well below 1ms).
- Read all of the input signals, and set various control signals (camera pretrigger/trigger, fluoroscope fire signal), thus replacing the Arduino system.

- Add an additional IR gate immediately prior to the field of view, to improve the accuracy of the walking speed calculation. This ensures that the walking speed is now the average speed of the subject as they travel through the field of view, instead of the whole walkway.
- Allow for more sophisticated logic to control of the fluoroscope firing than is available with the Arduino. Specific focus is made on numerous safety features to prevent accidental firing of the fluoroscope.
- Provide a single, simplified user interface that is flexible enough to be modified for future needs.

A basic overview of each loop on each component is given in the following sections for the LabVIEW VIs on the desktop, RT, and FPGA systems created in LabVIEW 2015 (BiplaneControllerGroundUp.proj). Also the reasoning behind some of the larger decisions is given. The user should look at the code for a more in depth analysis of the execution and functionality.

3.4.1 *Overarching Theory*

The biplane control system was designed in a modular fashion for easy creation, troubleshooting, and implementation of new features. The system uses three components: the desktop computer (User Interface, or UI), the real time system (RT) and the field programmable gate array (FPGA). Each of these components is given a defined and limited task which suits the memory size, processing speed, accessibility, and determinism of that component. The RT runs a Linux-based operating system and the FPGA execute independently of any operating system (e.g., Windows), allowing for precise control of system state. Also, both of these systems have a limited amount of memory compared to the desktop computer, as well as other hardware limitations.

The three systems are each set up using a different architecture to suit their responsibilities and fit their hardware limitations. The UI is set up with a producer/consumer architecture which allows two or more loops to communicate through messages. Messages are added to a queue and all messages are executed in order. This is a way for all of the user's commands to be processed without loss of information or inputs. The RT system uses a combination of consumer/producer and state machine architecture, and the FPGA only has a single state machine. One loop of the RT and the FPGA can exist in only one of a fixed set of states at a given time. The state can be changed by user interaction directly, or by the software in a predefined chain of states. For a simplified example, the FPGA waits in a safe state so that no devices are able to be triggered or turned on. There is no data collection and it is in an idle state waiting for user input. An example of a user defined state change is when the user selects one of many inputs (i.e., data collection mode) and executes the desired state. The FPGA will then change to that state, and complete all of its specified actions. An example of a chain of states would be when the FPGA completes the data collection mode specified by the user as previously stated; then upon completion of the data collection changes back to the safe state without further input from the user. In this case one state (safe mode) always follows a previous state (data collection mode). This automatic state change is used for many reasons such as completing multi-step actions, or to place the system in a default state where it can wait for the next user input.

The state machine architecture allows the code to be modular and easier to troubleshoot. A message is created in one loop and sent to another in the message stream to provide inputs. A message stream is a communication channel between two or more loops. The states are implemented in LabVIEW as their own separate and independent cases in a case structure. Cases are very easy to add, delete, rename, copy, and modify. Code can be added or changed in one case

and tested without having any effect on the other cases. Most of the time the cases in the case structure run similar code to complete similar tasks but this is not always true.

If multiple cases need to execute concurrently the case structure becomes much trickier. Only one message can be sent and read at a time in a single case structure, and if there is a chain of states, messages may be out of order and cause issues. If two messages are sent at the same time, and the first one read has a third message sent out upon completion, the loop will complete the second message before the third, even if the third message is of a higher importance. This is avoided in the current implementation by having one producer and one consumer per message stream and limiting the amount of messages sent out per loop iteration to one.

Screen real estate is at a premium in graphical programming software, and using a case structure effectively manages space, and allows the user to reuse screen space when dealing with different cases. Cases are layered on top of one another so that the user does not have to scroll around to find the code. This makes connecting wires and finding inputs and outputs much easier because they are always in the same location.

The system is designed for ease of use and safety. The user interacts with the UI which then communicates with the other two systems. This system also has many redundancies and specific procedures to control the fluoroscopes, so they do not turn on accidentally, which could expose the subject and user to unnecessary radiation.

3.4.2 *Names and Tasks of the Loops*

The loops of the three components are described in brief as a quick reference guide.

3.4.2.1 UI

UI Command Loop – Receives user inputs from the front panel and sends them to the communications loop.

UI Communications Loop – Sends messages from the UI to the RT, or to other loops on the UI.

UI Lossless Data Handling Loop – Manipulates and stores lossless data (i.e., data where every acquired sample is retained, for use in post-processing). It also populates some indicators on the front panel.

UI Lossy Data Handling Loop – Populates the majority of the indicators on the front panel to display current settings/measurements. These data are lossy, in the sense that some samples may not be acquired to prevent system lag. These data are used only for user display; data written to file is always lossless.

UI Camera Control Loop (x2) – Displays a live feed from each of the cameras.

3.4.2.2 RT

RT Communications Receiving Loop – Receives messages from the UI and duplicates the messages to control the FPGA communication and RT control loops.

RT Communications Sending Loop – Sends messages and settings to the FPGA to change state.

RT Control Loop – Collects data from the direct memory access first in first out buffer (DMA FIFO) and stores it for the UI to read.

3.4.2.3 FPGA

FPGA Main Loop – The only loop on the FPGA. It writes various signals to control the components to the biplane system and collects analog input signals. All of these signals are sent to the DMA FIFO to then be sent on the RT and ultimately the UI.

3.4.3 *UI*

The UI is run on the desktop computer and is primarily used for the user to communicate with the system through controls, view the current state and action of the system, and log data. The user interacts with the system through a variety of buttons and pull down menus to select the desired actions the system should execute next. The inputs and actions of the system are displayed through numerous indicators such as lights that turn on and off, strings, numeric displays, charts, and graphs. See the section on Daily Use for an explanation of the front panel controls and indicators.

Before any of the loops execute a couple of initializations occur. These initializations set logic controls, calculate constants, and initialize array lengths. Also communication channels are opened. Some of the outputs of the initialization are sent to the various loops to prepare the loops for execution.

UI Command Loop: The first loop to discuss is located at the top of the block diagram and is called the UI Command Loop. This loop takes all of the user inputs from the front panel and either changes the parameters of data collection or packages the inputs into a message and sends it to the UI communications loop. (See the message section below for messaging specifics.) The loop waits for a user input such as a button press, then runs the specified event structure one time and then waits for another input. Some event structures have case structures inside. The proper case structure is run from the parameters that are specified before the event (button press) occurs. This loop only communicates with the other loops; it does not do any data processing.

UI Communications Loop: The next loop is the UI Communications Loop. This loop completes two primary tasks: The first task is processing the messages from the command loop and sends them to the RT and ultimately the FPGA. The other is to execute actions on the UI. The UI Communications Loop waits for a message before the case structure executes. The message determines which case structure is executed. There are many states that the user can specify for data collection on the UI. All of the states on the UI can be reduced into one of two states on the FPGA. By reducing the UI states to two FPGA states, less data has to be transferred, allowing the size of the programs on the RT and FPGA to be smaller. This prevents redundant code on those components with smaller memory capacity. The loop also completes other tasks which involve only VIs on the UI, such as saving data. There are some automated tasks which it completes to make the interface more fluid for the user. One example of this is to populate the strain and analog signals graph after a trial. Another example is to automatically connect the UI to the RT upon start up.

UI Lossless Data Handling Loop: The third loop is the Lossless Data Handling Loop which executes once after every trial. This loop is used to obtain information about the last data acquisition after the trial's completion. It reads the data from a shared variable on the RT system and splits the data into its original 12 signals. The data are lossless because of the way it was captured and transferred. More about this process is explained in the inter device communication sections under FPGA to RT and RT to UI, as this is a two-step process. The data are used to populate a single graph containing the analog inputs and outputs of the system, and to populate the strain graph. These graphs are composed of the data that will be saved for the trial. The user can use these graphs to verify if the signals are as expected, making sure that all the signals were received and that no component failed during data capture. There is some data on either end of the

array that is trimmed off. The trimmed data contains values of the array that are initialized, but not repopulated with values taken during data collection. The two individual strain gages are inverted (so that loading the plate causes a positive change in strain) and summed to produce a single strain. It also calculates the subject's average walking speed between IR gates 2 and 3.

UI Lossy Data Handling Loop: The fourth loop is the Lossy Data Handling Loop. The majority of the indicators on the front panel are controlled by this loop. The indicators provide information to the user about what signals the system is receiving, and the state of all of the components. It displays information such as if the DMA has timed out, when the subject has broken an IR beam, whether the fluoroscopes are receiving a signal that would cause them to fire, etc. The data are lossy as it only reads the most current data at every loop iteration. The front panel has been limited to less than two dozen variables read with 50 ms between iterations (20 Hz update frequency). The indicators do not appear to have any latency (i.e., they appear to update in near real-time) through normal use, although a more in depth speed analysis could be completed for the current computer set up. This loop executes every 50 ms and starts by reading variables directly from the FPGA through the read/write command. The variables then populate numeric indicators or go through thresholding using greater than or less than logic to determine whether the light indicators will be on or off.

UI Camera Control Loop: The fifth and sixth loops on the UI are duplicates, one to display the live stream of each Phantom camera. These loops use the custom VIs provided by the camera manufacturer (Vision Research) to control the cameras. The cameras are initialized, and then the parameters are set. The current image is then read from the camera. The image is converted from 12 to 16 bit and is displayed on the screen. In the future, these loops should also contain

controls to change the settings of the cameras, but for now they are just there to allow the user to stream both views at the same time if desired.

3.4.4 *Safety features built into the VI*

The architecture of the UI allows for many safety features to be implemented to prevent unnecessary radiation exposure to the subject and staff. The “Arm Fluoro?” control was implemented to create a two-step process to fire the fluoroscopes to avoid accidental radiation exposure. If this button is not pressed, then the RT and FPGA do not receive a signal to fire the fluoroscopes and an indicator will illuminate conveying to the user that they forgot to press the button. Another safety feature is the “Emergency Stop” button which stops the fluoroscopes from firing from the front panel. The “Undo Emergency Stop” button then has to be pressed to allow another data capture to begin. This will create a multi-step process to fire the fluoroscope again to avoid subsequent accidental firings. There is also a hardware emergency stop on the BNC cable from the FPGA to the fluoroscopes that can be used that will physically disrupt the signal.

3.4.5 *RT*

The RT is primarily used as a way for the UI to communicate with the FPGA and the FPGA to transmit data back to the UI for logging. It is running on a board in the RT chassis, and has a Linux real time operating system. When data are being transferred back to the UI, it completes some data processing. This device does not suffer from latency due to other processes or programming since it only runs a compiled form of CPU instructions defined by the LabVIEW code for the RT system. The user does not have to interact with this VI minus pressing the run button on first start up. There

are no controls on the front panel and very limited indicators used for system debugging; these controls are either unimportant to the user when controlling the system or may be redundant to the displays on the UI.

There are three loops running on the RT. One of the loops receives commands from the UI, another loop sends commands to the FPGA, and the last loop controls the actions being performed on the RT system. Before any of the loops run there are a couple of pre-initializations which occur, to set some other variables, and set up the communications stream.

RT Communications Receiving Loop: This loop receives messages from the UI and sends out the appropriate messages to the other two loops. The first message is written to the FPGA communication stream. This message consists of a string to identify the message, and a user-defined set of variables as the content of the message. The second message changes the RT state to complement the FPGA state. If the FPGA is sent a message to go to the safe state, the RT will also get a message to go to its safe state. If the FPGA is sent a message to go into either dynamic or static acquisition mode, the RT will be sent a message to go to its single case to handle the data acquisition. Like other loops dependent on dequeue message VIs, this loop only executes when it receives a message.

RT Communications Sending Loop: The second loop reads the message sent from the UI communication loop and then passes the message to the FPGA. The dequeue message VI pauses the loop until a message is received. Once received, the message is unpackaged from the variant data type and is sent to the FPGA read/write VI. This VI sends all of the variables to the FPGA during one loop iteration to change the state of the FPGA and send the appropriate variables for the state change.

RT Control Loop: The third loop changes the state of the RT to compliment the FPGA. There are three states the RT loop can be in. The first one is the initialization state, which is called upon start up; currently nothing occurs during this state, but is designed to provide for future expansion. This would be where variables and other processes could be initialized in the future for this loop. The second state, Safe State, is where the RT waits for a command, and does not complete any actions.

The third, and most complicated of the states is the data acquisition state. This state reads the data from the FIFO between the FPGA and the RT, and stores the data in a single variable. A more in depth description of the data transfer method from the FPGA to the RT is given in the Communication Section. The basic task flow of the loop include: 1) determine the amount of data to read per loop iteration, 2) read a chunk of data from the FIFO buffer, and 3) append these values to an array during every loop iteration. After the FPGA has finished placing data in the FIFO (and thus switched back to Safe State), the RT completes one more iteration and reads the rest of the data from the FIFO, thereby emptying the buffer. While the RT is reading data a shared variable is set to true which illuminates an indicator on the UI front panel to let the user know that data are being collected. Afterward it is switched back to false, and all of the data are sent to a shared variable for the UI to read and process further.

3.4.6 *FPGA*

The FPGA is a set of silicon chips located in the RT chassis that read and write signals to monitor and control biplane hardware. They are configured through a compilation of LabVIEW code which produces a bit file. The bit file configures the logic of the FPGA. The FPGA does not run an operating system as it is hardware that is configured to directly run the specified code. It has a

limited amount of memory for storing code and saving data. Because commands are directly executed on the hardware, it is much faster than the UI and the RT, and can deal with highly parallelized tasks. Separate sections of the FPGA are designated for specific parts of code so the different parts can be run completely independent of each other. This makes it suitable for deterministically reading and writing data synchronously for many channels.

FPGA Main Loop: The FPGA only has one loop running with a state machine architecture. The states that the FPGA can inhabit are Safe State, Static Capture, and Dynamic Capture. There is an outer while loop that keeps the FPGA running and in the data capture states there is an inner while loop. The inner loops are slightly different and are explained in detail in the appropriate sections below. The overall flow of the FPGA can be broken down into two steps. The first action of the FPGA is to complete the state defined in the last iteration, and the second step is to determine the state and inputs for the next iteration. The determination of the state comes second for a couple of reasons. The first is to minimize the amount of variables carried over between iterations. Another reason is to help enforce data flow and speed. There are three points in which the state can be changed. They are, in order: 1) if there was an error in data collection to go to the safe state, 2) when ending a data capture state the FPGA is forced to the safe state, and finally 3) there is an input from the user to change the state to one of the three desired.

The first state to describe is the default mode called Safe State. This is the default state where the fluoroscopes are off and all the other devices are put into a dormant state. Some signals maintain a value during this state that is equal to the off value during data acquisition so there are no discontinuities between state changes. It is the state the FPGA goes to when waiting for an input, and when the FPGA first initializes. It will also go to this state if there is an error during data collection, data collection finished, or the user can force the system into this state.

The second state is Static Capture. This state is used to capture data when the user wants the data capture to start at and run for a specified amount of time, without being triggered by the IR gates. Examples of when this state would be used is during data acquisition for localization or distortion correction, or when taking static data of a subject. The FPGA goes into this state only from user input. After predetermined times the pretrigger, fluoroscope, and trigger signals turn on for a predetermined duration and then shut off. These parameters are what populate the "FPGA Control" cluster on the front panel of the UIMain.vi. Data acquisition begins when the "execute current mode" button is pressed.

This capture sequence utilizes a while loop to collect data for a predetermined period of time. The data capture in this loop takes place over two inner loop cycles. A wait function is used to ensure data are taken at specified intervals of every 0.5 ms or 2000 Hz. First a reference time is created for the loop which is important in timing data, and stopping the loop. The input parameters of the "FPGA Controls" are read. These parameters then go into subVIs which create single square pulses at predetermined times and for predetermined durations for each of the pretrigger, fluoroscope, and trigger signals. The inputs and outputs are synchronously read and written. All of the output and input signals along with some timing data are then appended into an array which is sent to the FIFO buffer. More about this data transfer is described in the Communications Section FPGA to RT. Some of these signals are also sent to indicators that are then displayed on the front panel of the UI. The loop stops after a predetermined amount of time after the three outputs (fluoroscope, pretrigger, and trigger) have all switched back to their off states. This allows for some post trigger data at the end of the capture to be present so the user can ensure that no important data were clipped from the end.

The Dynamic Capture state is used for capturing data when a subject is walking through the system. It can also be used for any other event that relies on some unknown start time when the first IR gate is broken, and will occur for an unknown period of time. The Dynamic Capture state is a series of two phases, the first being a wait mode for the first IR gate to be broken, and the second is for data acquisition. The user selects the "Execute Current Mode" button to put the FPGA into the Dynamic Capture state in the waiting phase. At this point, the system is waiting for the subject to break the first IR gate's beam to initiate data collection. It will stay in this phase until the first beam is broken or the trial is aborted through a switch on the UI front panel.

When the IR beam is broken, the gate 1 input triggers the system to go into the acquisition phase of the Dynamic Capture state. This phase is very similar to the Static Capture mode in setup, data acquisition and reading and writing of signals; only the differences between the states will be explained below. The primary difference is that the fluoroscope fire signal and camera pretrigger and trigger signals are now set by IR gate trips. Specifically, the FPGA creates a single square wave at a predetermined amount of time after the first IR gate is tripped instead of after the "Execute Current Mode" button is pressed for the fluoroscope fire voltage; the camera pretrigger signal is similarly sent by the FPGA. The trigger signal, still a single square wave for a predetermined duration, is now produced after IR gate 3 at the end of the walkway is broken, not at a predetermined time as in Static Capture mode. The trigger signal can be delayed by a specified time after IR gate 3 has been tripped. The fluoroscope is shut off either after the specified duration, or once the subject breaks IR gate 3. This avoids extra radiation after the subject passes through IR gate 3, which would not benefit the data collection since the subject is out of the field of view. The dynamic data capture acquisition phase ends at a predetermined time after the trigger signal turns off, or if the user presses a button on the front panel to terminate the trial early.

3.4.7 *Timing of Camera and Bridge Module*

The FPGA collects data at the interval of 0.5ms, or 2000Hz. This time was chosen to allow the LabVIEW data rate to be an integral multiple of the Phantom camera image capture rate, which is currently set to 1000Hz. The strain data are collected through a Wheatstone bridge module which has its own on board clock running at 12.8MHz. It can only be operated at specified sample rates ranging from 1.613KHz to 50KHz. A sample rate of 2KHz was chosen since it was a multiple of the camera data rate to more easily align data in post processing while having better temporal resolution. This would allow two data points per frame to determine if heel strike or toe off occurred. The next highest multiple of the frame rate is 5KHz. While this would offer better strain temporal resolution, the additional amount of collected data (and accordant increase in file size) was considered unnecessary and an inefficient use of computer memory, since the camera acquisition rate was capped at 1000Hz and thus the tracking in the fluoroscope system can only be resolved to a 1ms rate.

3.4.8 *Intra and Inter System Messaging*

The UI and RT use messages to communicate between loops within each system and between systems. Messages are a fast and clean way to transfer data between two loops and allow the OS to complete other tasks when not called. This section highlights the details of the messaging scheme on the UI and RT systems for communication between both loops on the same component and loops between components.

3.4.8.1 Message Map

The messaging used for communication inside and between the three components is set up in a pyramidal fashion. This allows the user to have many choices for predetermined states while simplifying and compressing states on the lower memory sized components such as the FPGA. The messages that are sent between the three systems can be organized as a tree (Figure 3.2). This structure was created so that the user can have many options in selecting a state, and collapsing the message structure as the messages get to the FPGA. This strategy allows for flexibility in the number of states on the UI, where memory is substantial, but reduces to only a limited set of states on the FPGA, where available memory is more limited. It is important to have many states for the user to choose from to allow for a unique predefined setting for each one. An example of this would be the Localization and Distortion modes. Both take static shots of a single object in the field of view, but may require different setting or durations to collect the appropriate image data. Having predefined settings allows the user to complete the same task multiple times without having to worry about human errors being introduced when entering parameters multiple times.

All data capture is grouped into static or dynamic data capture modes on the FPGA. Static data capture is meant for taking any image capture in which the start time and duration are both known and can be predictably completed. Examples include: imaging the localization block or the distortion plates, which are a single static object in the field of view, or when an object is dynamically moved through the field of view based on a user defined start time and for a specified duration (ie. A short dynamic trial where the user predicts (or determines) when an object will be in the field of view, like dropping a rubber ball on the platform). The dynamic data capture is used when the start and end time of the image capture are not known prior to the test, but rather will start and end with the IR gates, such as a subject gait trial. With all of the selectable data capture

modes compressing into two modes on the FPGA, this greatly reduces the amount of logic required on the FPGA.

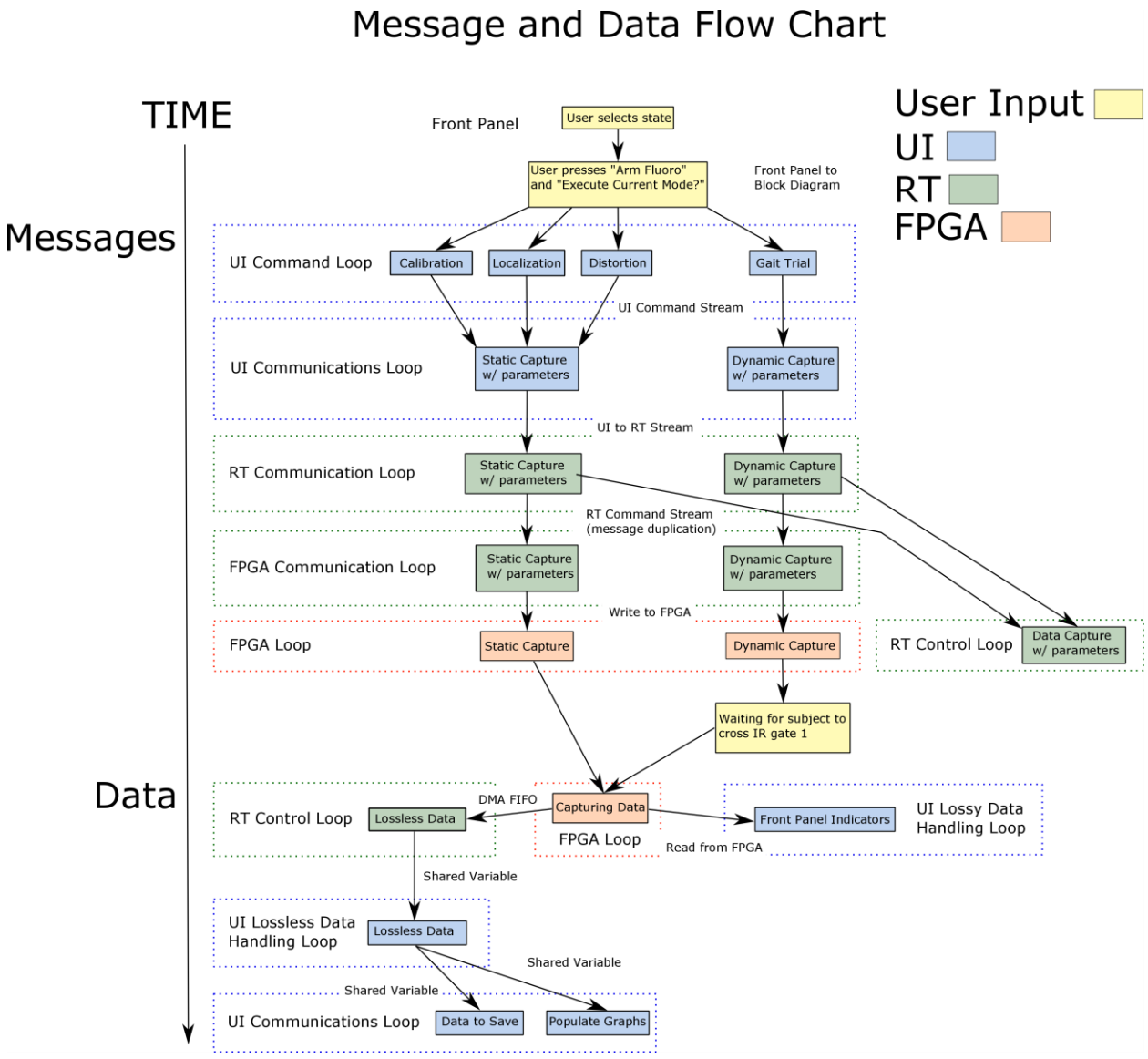

Figure 3.2. A messaging map for a static or dynamic trial.

3.4.8.2 Messages

Messages are comprised of two types of data to be sent between different loops on the same or different component. They are typically used to control state machines or send data between loops. The first piece of data are a single string, used as a title or identifier. In the state machine architecture this is used to define the particular case to use in the structure. The second set of data are called a message. The message can consist of any type of data or combination of data (boolean, string, numeric, etc.) sent between loops. The data are packaged into a data type called a variant before it is sent. To use a variant, the user must define the format first. The order, type of data and bit depth of each element have to be specified during the writing and the reading of the message. In the current version of the software a single cluster is used to define the format of the parameters sent to change the FPGA state. A custom type definition is used for easy creation and modification of these parameters. The type definition can be changed and all the variables that are based on the type definition will have their format changed as well.

The enqueue message VI is used in three different loops, the UI Command Loop, the UI Communication Loop and the RT Communications Loop. The enqueue message VI packages the string and message into the variant and sends it to the message stream. The message stream is a first-in/first-out (FIFO) queue. The dequeue element VI reads the messages in order from the queue and populates the case and variables with the title and message data. It only reads one message per loop iteration. The loop cannot proceed forward until a message is read since the dequeue element VI pauses the loop until there is a message to read from the FIFO.

The current system utilizes a one-to-one ratio of enqueue to dequeue message VIs. This is the simplest model to create and maintain. There are other methods that can allow for more than one enqueue or dequeue VI but those will not be discussed as they are not used in the current setup.

3.4.8.3 Shared Variables

Shared variables can be read or written in any loop on either the UI or RT components and the data can be transferred between loops and components. The shared variables have to be fully defined in size, type, and bit depth, and this is done so when they are added to the block diagram when creating the VI. Communication issues can occur when the variable is written to more than one place. This could create a race condition. To avoid this, only one shared variable write and read was used in the system. It is used to transfer the analog inputs and outputs read from the DMA FIFO from the RT to the UI.

3.4.9 *Intra Device Communication*

3.4.9.1 UI

The UI communicates between its various loops using messages which originate from the user via input from the front panel. On the UI there are currently two independent message streams used for communication. One message stream prepares messages for the RT and FPGA, or manipulates the data that is sent back to the UI from those systems. The other message stream is used to control the cameras, which is handled entirely within the UI component.

3.4.9.2 RT

The RT system receives messages from the UI through the RT communications loop. The UI to RT stream has a single enqueue VI; however, the RT needs two messages: one to control the FPGA and another to control the RT, both with slightly different inputs. To maintain a one-to-one enqueue/dequeuer structure, the RT communications loop duplicates the message and sends them to two different streams. One message sends the message identifier and required parameters to the

FPGA control loop and the other sends the appropriate variables to the RT control loop for data acquisition.

3.4.9.3 FPGA

The FPGA has a much more simplified control scheme than the other two components, as the messaging architecture is more complicated than what is needed in this situation. It instead uses a simple state machine, where a single enumerated constant is used to maintain or change its state. The enumerated constant passes through a shift register at the end of each loop to be carried over to the next iteration. The FPGA would change its state when the enumerated constant is changed either through user input or by preset state changes. At the end of the loop, or earlier if there is an error in data capture, the state is forced to go to the Safe State by default. The last way the FPGA can change its state is through user input. The user can put the FPGA into the safe state, or either of the two data capture modes. The state is passed to the next iteration and the appropriate case structure is selected. Besides the state there are a handful of other variables that are passed on to the next iteration through shift registers also.

3.4.10 *Inter Device Communication*

3.4.10.1 UI to RT

The UI uses messages to send data to the RT. The message is populated with the inputs from the user's interaction with the front panel. The messages are then collapsed in the communications loop to simplify the commands going to the RT and ultimately the FPGA. The RT and FPGA have limited memory, and the simplification of messages was necessary to match the simplified states on both systems. The RT exists in only two states: data acquisition or safe state. All data acquisition tasks, whether static or dynamic, are handled on the RT in the same manner.

3.4.10.2 RT to FPGA

The RT controls the FPGA through a read/write VI. The RT sends a cluster of variables which are then used to populate the appropriate controls on the FPGA. The FPGA can only have a variable written to it if the variable has a control of the front panel. As mentioned before the read/write VI is a lossy data transmission method where it may not transfer all of the data if data are sent in multiple iterations. This is not an issue in this usage since all of the parameters to change and control the FPGA state are sent at once in one variable. If the FPGA does not read these variables in the current iteration they are sent, then they will be read the next iteration that is half a millisecond later.

3.4.10.3 FPGA to RT

The FPGA communicates with the RT system by DMA. This method was chosen to transfer large amounts of data, in a specified order, and to keep the data organized in time. This data transfer type tends to have larger overhead to start the transfer, but is faster than a read/write command during transfer. The read/write is explained further in the FPGA to UI section where this type of data transfer is heavily used.

The FPGA only has three DMA channels, which would not accommodate all of the signals sent to the RT if each signal was assigned its own DMA channel. To bypass this problem, the FPGA interleaves the data into an array for each time step, as per National Instruments-recommended practice. The FPGA is currently configured to capture 12 channels of data at 2000 Hz, and interleaves the data into a single array. At each iteration, the data (12 elements) is always placed in the array in the same order. After the array is populated, it is passed on to the next loop iteration through a shift register. The array is then written to the DMA FIFO buffer (from here on referred to as FIFO) on the subsequent loop. This twostep process is called pipelining. Both the

acquisition of data and the sending the previous loop iteration's data to the FIFO occur in parallel, reducing the loop execution time.

The FIFO is set to 16384 elements long when the VI is initialized; this FIFO size can be configured by the user to a size of 2^N (where N is an integer). The RT should read elements from the FIFO in groups of 12 to insure that when the data are decimated from the array each channel is in order and has the appropriate content. The RT read size is determined by the wait time of the RT Control Loop multiplied by the number of samples per millisecond multiplied by the number of channels. The current settings yield a 200ms wait, 2 samples read per millisecond (2000Hz), and 12 channels, so the data read size is 4800 samples. The FIFO size was chosen to be about 3 times larger than what would be needed in a data transfer. This would ensure that the FIFO would not overflow if the data were not read once or twice. While completing this calculation before a data read, a wait function is used to delay the RT so there will be 4800 elements to be read on the first iteration.

The loop is set up for the RT to first read the number of available elements for transfer. If the amount of available elements is greater than 4800, then the RT reads the first 4800 elements from the FIFO. If it is less than 4800 elements, then it reads 0 elements and proceeds to the next loop iteration, which starts with waiting another 200ms. During this wait period, the FPGA is filling the FIFO with more data. On the next iteration, all of the previous data points not read would still be in the FIFO, and all of the new data points collected are appended to the end of the 1D array. The 4800 data points that have been in the buffer the longest are then read from the FIFO (removing them). This is the definition of the FIFO, data that is first placed first into the buffer (by the FPGA) is the data first read out of the buffer (by the RT). When the RT reads the data from the FIFO, it then uses those values to populate a 1D array. Every subsequent read from the FIFO is

appended onto the shared variable in order. This loop continues until the FPGA switches back to safe mode. During the last iteration the RT reads the rest of the data from the buffer, which may be less than the 4800 elements. This last iteration occurs after the FPGA has stopped filling the FIFO with data, ensuring that no data will be left in the FIFO after the RT stops reading data. The RT saves the 1D array to a shared variable. The array, and the shared variable are very long 1D arrays (for example, a 5000 ms long trial contains 12 channels x 2 data points per ms x 5000 ms = 120,000 data points). In summary, the FPGA places a little bit of data (one data point from 12 channels) in the FIFO very quickly (every 0.5ms) which utilizes the ability of the FPGA to complete many tasks in parallel. The RT reads (emptying) the FIFO at a much slower rate (every 200ms), but reading many times more data than the FPGA utilizing complex data transfer methods available on the RT system. The data transfer rates of each system should be equal over a large period of time so that the FIFO does not overflow or underflow. The FPGA transfers 24,000 data points per second (12 data points at 2000Hz) so the RT should also read 24,000 data points per second (4800 data points at 20Hz). The FIFO size should also be an appropriate size to prevent a FIFO overflow, but not use excessive amounts of memory.

3.4.10.4 RT to UI

Data are transferred to the UI from the RT through the use of a shared variable. This single variable is a 1D array that contains all of the signals from the FPGA in an interleaved fashion and tends to be over 100K elements long. After the data are transferred to the UI, in LabVIEW terminology, it is decimated into the twelve original signals. A graphical illustration of the interleaving and decimating is shown in Figure 3.3. Multiple pieces of data are read at the same time (AI Channels 1,2,3). They are then ordered and appended to the end of an array (in the FIFO and RT system

memory). When the array is transferred to the UI the signals are then reorganized to back to their original channels and can be processed.

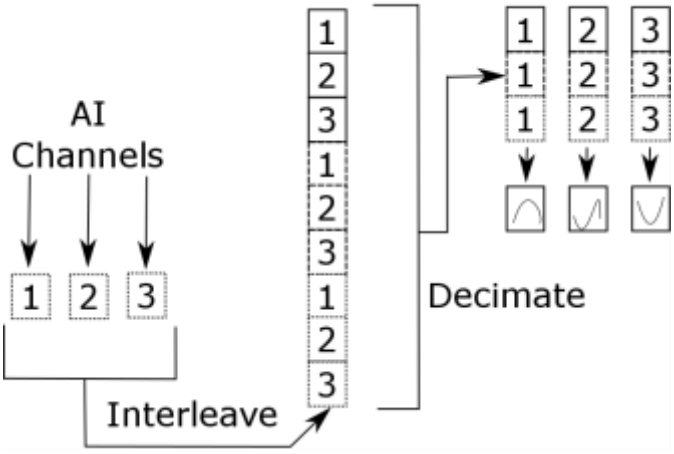

Figure 3.3. A graphical illustration of an example data set with data interleaving and decimating with three data channels. At a given iteration the FPGA reads a number of samples at a given time. The data are interleaved into a single 1D array for data transfer. Once transferred, the data are decimated into their individual signals for data processing.

3.4.10.5 FPGA to UI

The FPGA also sends some data directly to the UI without using the RT as an intermediary. Data are transferred directly to the UI by the read/write command which requires very little overhead to start, and is quick. It is best used for transferring single points of data from one system to the other, like in displaying the voltage across and IR gate to determine if it is tripped or not. This is a lossy data transfer method, as the read/write command only displays the most recent value of the data. It can miss data on any iteration depending on the loop speed and the amount of data to read/write. This method is currently used for boolean, numeric or string indicators to display the current state of the FPGA. A moderate length wait is used in the UI loop that reads the indicators (50ms) to give it enough time to read all of the appropriate data. The wait duration was chosen to provide

enough time for the UI to complete the read/write command, and allow the indicators to update of the front panel in a visually smooth manner (i.e., an update rate of 20 value updates/sec). Larger delays (100ms and higher, causing frame rates of 10 value updates/sec or lower) make the indicators appear to be jumpy to the user.

3.5 HARDWARE AND SOFTWARE SPECIFICATIONS

This section lists the major hardware and software components used in the system. It describes the design and configuration of the circuits for the IR gates, pretrigger, trigger and fire fluoroscope signals (Figure 3.4 and Figure 3.5). The placement and testing of the strain gages are also described.

3.5.1 *Hardware*

A. Arduino – Custom designed implementation of off-the-shelf Arduino parts, and custom programming
B. Analog Input Module – National Instruments NI 9201 Analog Input Module
C. Analog Output Module – National Instruments NI 9263 Analog Output Module
D. Bread Board - Jameco ValuePro
E. Camera – Phantom V5.2 (Qty 2)
F. Computer – Dell Precision 390 w/ Intel Core 2 Duo
G. Fluoroscope (Emitter and Image Intensifier) – Philips BV Pulsera (Qty 2)
H. IR Gates – Banner Q45VR3LP
I. Network Hub - Cisco SG 100D-08

J. Network Switch - NetGear ProSafe 8 Port Gigabit Switch

K. Power Strip - Belkin

L. Power Supply – National Instruments NI PS-15

M. Real Time Chassis – National Instruments NI cRIO-9064

N. Strain Gage Module/Wheatstone Bridge – National Instruments NI 9237 Bridge Completion Module with a 37-pin DSUB

O. Strain gages – Micro-Measurements 350 **Ω** biaxial strain gage

3.5.2 *Software*

1. Windows XP
2. LabVIEW 2015
3. Phantom 675.2

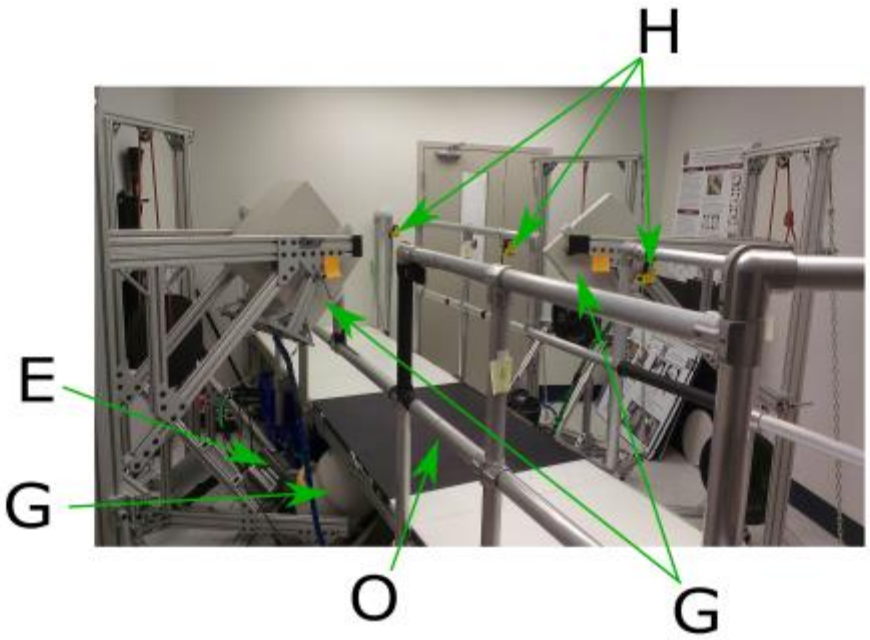

Figure 3.4. Hardware components along the biplane walkway. The following letters correspond to the described parts: E – High speed camera, G – Fluoroscope (emitter and image intensifier), H – infrared gates, O – strain gages on bottom side of carbon fiber panel

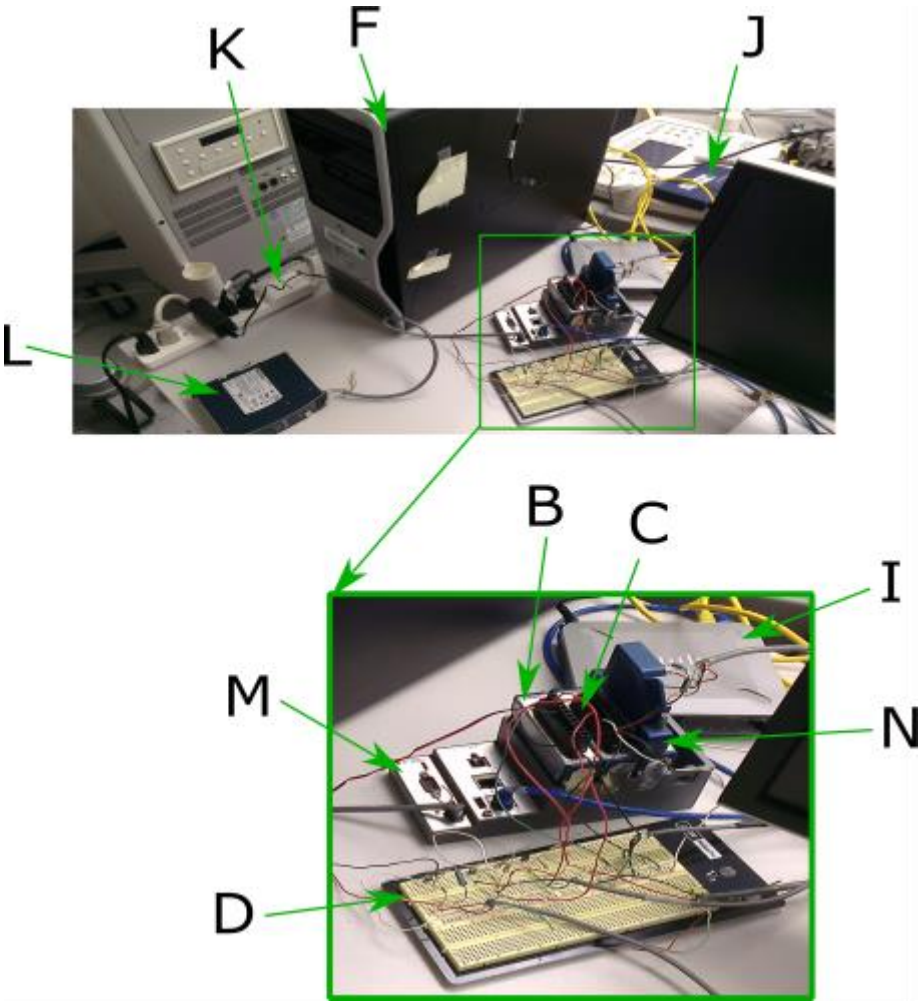

Figure 3.5. Hardware located on the desktop. The following letters correspond to the described parts: B – analog input module, C – analog output module, F – desktop computer, I – network hub, J – network switch, K – powerstrip, L – power supply, M – real time chassis, N – strain gage module

3.5.3 *Current Inputs and Outputs*

AI0 – Fluoroscope Voltage between the hot and ground

AI1 – IR Gate 1 Voltage - Normally 5V and goes to 0V when object blocks gate

AI2 – IR Gate 2 Voltage - Normally 5V and goes to 0V when object blocks gate

AI3 – IR Gate 3 Voltage - Normally 5V and goes to 0V when object blocks gate

AO0 – Fluoroscope Control Signal - Signal to fire fluoroscopes

AO1 – Pretrigger Signal - Switches cameras to recording mode and starts capture buffer

AO2 – Trigger Signal - Marks the zero frame and stops recording after the specified number of post-trigger frames have been captured

AO3 – IR Gate Voltage for all gates - Sends out the constant voltage needed by the IR Gates

Bridge 1 – One of the strain gages on the biaxial strain gage used

Bridge 2 – The other strain gage on the biaxial strain gage used

3.5.4 *Wiring Configurations*

There are two circuit configurations used three times apiece to control and read the various signals of the biplane system. One wiring configuration is for the IR gates (read), and the other is for the pretrigger, trigger, and fluoroscope signals (Figure 3.6). The current implementation uses half of a breadboard.

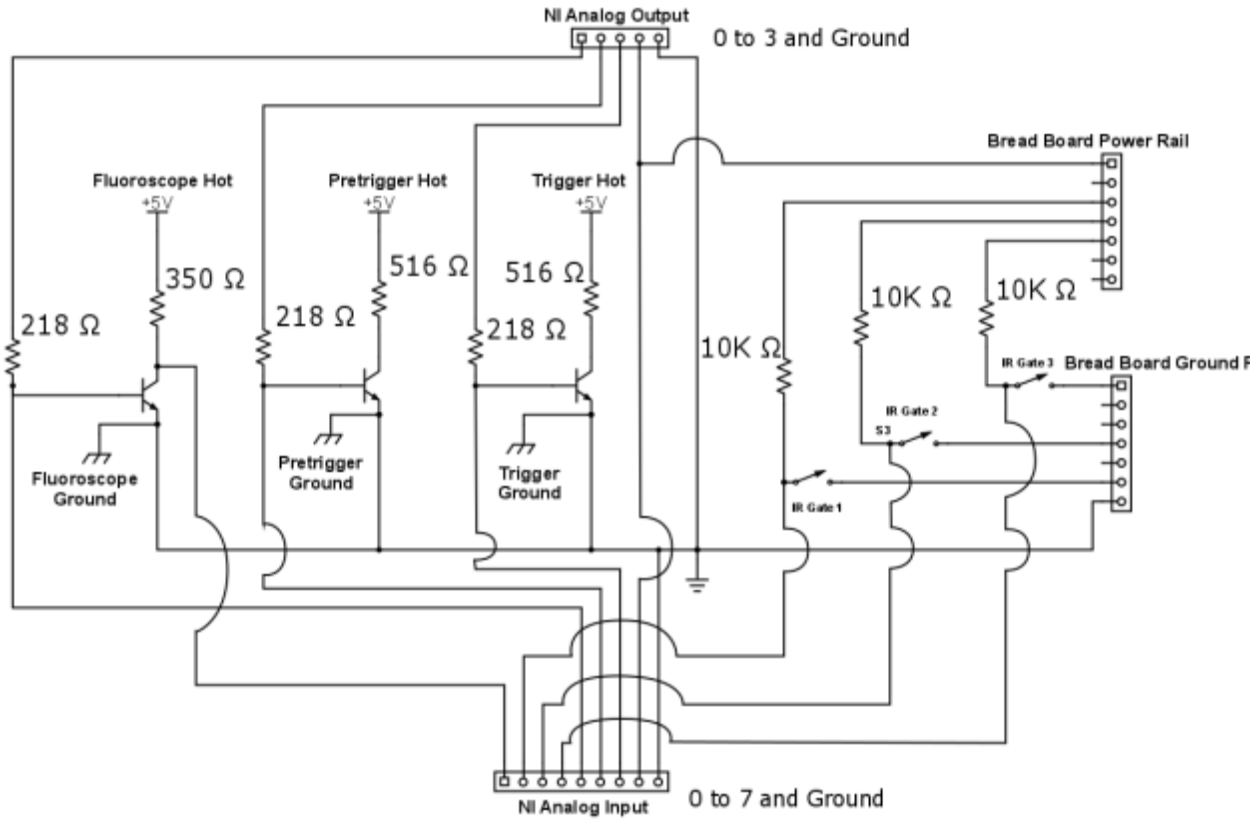

Figure 3.6. The full circuit diagram to the biplane control system.

3.5.5 *Inputs*

Each IR gate operates as a normally-open switch connected between a supply voltage and ground; interrupting the infrared beam shorts the voltage to ground. To supply this voltage, the analog out channel 3 is used, sending a constant 5V to the breadboard hot rail. A 5V signal is used as it is within the limits of the voltage output of the AO module and offers a fairly wide range between on and off voltages for the AI to read. From the rail a 10k**Ω** resistor is used to minimize the current through the gate circuit. The resistors used in these three circuits have a ¼W power rating, which is much higher than the calculated power of 2.5mW. After the resistor is an analog input lead, and the IR gate hot lead. The circuit continues through the switch (normally open) and the IR gate ground is connected to the breadboard ground which is the common ground to the system. This

configuration measures the voltage drop across the IR gate, with 5V present when there is nothing blocking the IR beam (open), and 0V when an object breaks the beam (closed). The IR gates can alternatively be configured to be normally closed, thus reversing the logic. There is no benefit to this, so the method used in the past was carried forward of a high off signal is used.

3.5.6 *Outputs*

The three signals that are controlling the biplane system utilize transistors to act as switches. The cameras are set up to receive a single pretrigger and trigger signal synchronously. The fluoroscopes are set up in a master/slave configuration through a custom circuit board designed and installed by the manufacturer, so only one signal has to be sent to the system and both fluoroscopes fire synchronously. The original manufacturer's foot pedal switch for the fluoroscope was custom-modified to allow for an external signal to emulate depressing the pedal, in turn firing the fluoroscope. The camera voltage is around 4.8V and the fluoroscope voltage is about 5.0V between the hot and ground leads. A similar circuit was used to control each signal, with only the resistor sizes being different. The fluoroscope or camera hot wire is attached to a resistor, which in turn is attached to the collector of the NPN transistor (Figure 3.7). The emitter of the transistor is attached to the breadboard ground which is also the common ground for the entire system. The base of the transistor is attached to another resistor which comes from an analog output channel that controls the state of the transistor.

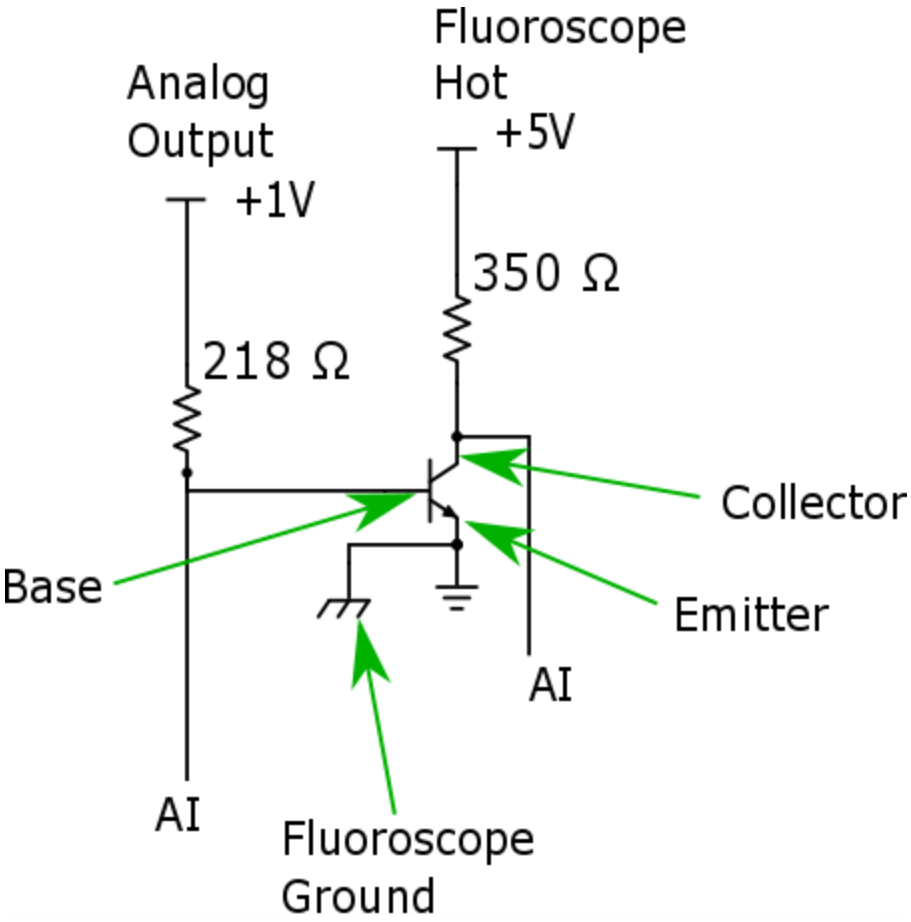

Figure 3.7. The transistor circuit diagram for the fluoroscope.

In this project, transistors are used as on/off switches to cause camera triggering and fluoroscope firing. There are four states a transistor can be in: cutoff, saturation, forward active, and reverse active. A transistor has three terminals: the collector, the base and the emitter (Figure 3.7) . The collector and emitter are used for the primary signal to pass through, and the base is treated like a switch in the present set up. The cutoff region is when the transistor acts as an open switch with little to no current going from the collector to the emitter. This is achieved by having a base-to-emitter voltage V_{be} less than a value V_{be0} specified on the transistor's datasheet (V_{be0} is typically around 0.60 to 0.95 V). Saturation mode is where the transistor acts as a near short circuit where any increase in the base current yields no increase in collector to emitter current. For the transistor

to be in saturation mode, V_{be} has to be greater than V_{be0}, and the base current I_b multiplied by the gain (**β**) is greater than the collector current I_c. In forward active mode, the emitter current is proportional to the base current. V_{be} is greater than V_{be0} and the base current multiplied by **β** is not greater than the collector current. Reverse active mode is when the transistor is biased in the opposite direction of the active mode, producing the opposite signal as forward active, but still acts proportionally.

First the minimum current required to fire the fluoroscopes and pretrigger/trigger the cameras was found. That is, the minimum current for the fluoroscope to recognize that the pedal was depressed, and the minimum current for the camera to recognize a trigger signal, was identified. To do this, a single resistor was connected to the hot and ground of each device's signal wires. The first resistance used was 50k**Ω** and then was incrementally decreased. The cameras' signal for the (pre)trigger changed to the on state at 700**Ω**, but did not change at 1000**Ω**. The fluoroscopes changed at 350**Ω** but not 500**Ω**. This would give a needed current of 6.9mA for the cameras to pretrigger or trigger and 14.2mA for the fluoroscopes to fire. The resistor leading to the collector with the camera signal was chosen to be516 **Ω** so it would be under the 700**Ω** found to cause a trigger even with the added resistance of the transistor which was found to be around 30K**Ω**. The transistor emitter was directly attached to ground so the minimum base voltage needed to put the transistor in saturation would be 1V. The next step was to determine the base resistor so that the base current times the gain would be greater than the collector current. A resistor of 218**Ω** was chosen to allow for a base current times gain (**β**=100 for this transistor) to be about 8 times the collector current. When using transistors as a switch it is not uncommon to introduce an overdrive factor pushing the transistor well into the saturation range, with some circuits going up to a factor of 10 or higher. All of the resistors chosen had a power rating of ¼ or ½W depending

on what sizes were available and all of the power in the circuits is well below the maximum rating for the resistors. The fluoroscope circuit was designed in a similar manner as the cameras utilizing different size resistors to suit this circuit. See the Appendix for relevant calculations, example problem, and specifications to the circuits.

3.5.7 *Camera and Infrared Gates*

The cameras receive pretrigger and trigger signals when the first and third IR gates, respectively, are crossed. These signals control when the camera saves the images to memory. Each of the two high speed cameras is able to hold 1996 images at its maximum resolution of 1152 x 896 pixels. The camera software has a circular buffer that is initiated after the pretrigger signal is received. The image buffer fills up with the first 1996 images, and when the buffer is full the newest image replaces the oldest image in the buffer. This can occur indefinitely and only the most recently-acquired 1996 images are stored in memory. When the camera receives a trigger signal, it marks the next frame as the zero frame. The camera then continues to take images until the amount of specified post trigger frames are taken, and stops recording.

The amount of frames before and after the trigger is set to 1986 and 10 respectively. There are many more images taken before the trigger frame because IR gate 3 is physically placed after the field of view. Thus, the events of interest occur before the trigger signal is sent. The cameras are configured to acquire images at 1000 Hz with a shutter speed of 990ns to reduce motion blur and allow enough light into the camera for good image contrast. There are ongoing studies determining the optimal camera and X-ray parameters to obtain images of optimal brightness and contrast.

3.5.8 *Strain Gage*

Because determining stance phase timing from imaging alone proved difficult, it was desired to have an instrument independent of the imaging to determine stance phase timing. Determining heel strike and toe off during data capture is important to metrics such as duration of stance phase and to be able to quantify the timing of events during stance phase. During image capture, only the part of the foot of interest may be in the field of view. A trial where the hindfoot is biased toward the center of view to better image the calcaneus and talus may exclude the hallux and part of the first metatarsal from the image. In this case heel strike could be roughly calculated but the toe off time would not be able to be quantified since there is no data on the kinematics of the hallux and possibly first metatarsal. Another modality with finer temporal resolution than the images themselves to measure foot contact would be beneficial so that a single frame can be determined as the closest frame to contact. By analyzing the images alone, the exact frame cannot be determined – instead only a small range of frames can be selected that contain heel strike or toe off.

Some of the modalities evaluated to detect foot contact were: a force plate, IR beams located above the floor, or foot contact switches. All modalities except the strain gage were excluded due to degrading image quality from being in the field of view, adding mass (or volume) to the subject's foot, no feasible way to capture both heel strike and toe off, or being cost prohibitive. A strain gage was determined to be the easiest and simplest method to determine when the subject's foot is in contact with the X-ray-transparent floor plate. At first the strain gage was placed in an arbitrary position within 5cm from the field of view. This arbitrary position was near and almost aligned with a diagonal line that went from corner to corner. It was also on the side closer to the subject's start position so it would be closer to where the heel would strike the plate.

Strain gages are designed to output a raw voltage signal proportional to strain of the sensing element. However, the raw voltage signal is generally too small to be perceptible, and are typically configured in a Wheatstone bridge to amplify the measured signal. In this study, biaxial strain gages, containing two separate sensing elements arranged orthogonally, were used. Both of the elements on the biaxial rosette produced a more negative voltage when the plate was loaded by a subject. Wheatstone bridges can be configured so that the voltages across the sensing elements can either be added together or subtracted. The NI bridge completion module used does not allow a configuration that will add the signals of each element together. These two elements were configured in two separate bridge completions so the signals could be added together later during signal processing to produce a stronger signal. The strain gages used are not calibrated to record the actual strain of the plate. The output of the strain gages used to determine foot contact is the difference in voltage between the two sides of the Wheatstone bridge.

Initial testing determined that the strain was sufficient to determine heel strike and toe off. The strain curve followed the same pattern as a ground reaction force measured by a force plate during walking (Figure 3.8). The strain curve began to rise as expected at the impulse of heel strike, and exhibited a double hump pattern typically seen in the ground reaction force of a gait trial. The strain in this case is not indicative of the magnitude of the ground reaction force, as the gage was not properly calibrated to do so, and the magnitude of the strain greatly depended on where the subject contacted the plate. This was not a problem, however, as the gage was only intended to provide stance timing, and not force magnitude.

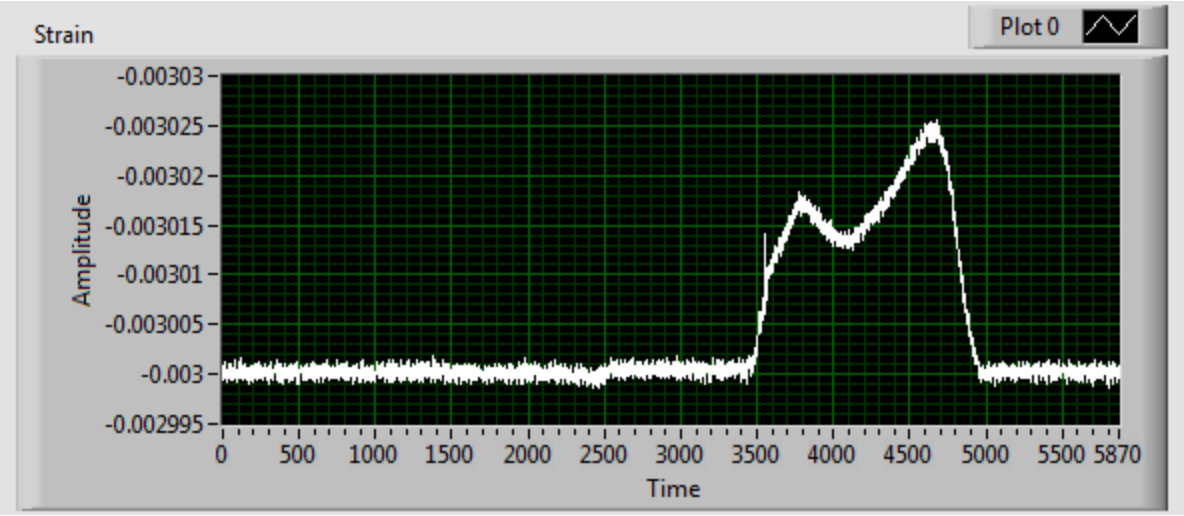

Figure 3.8. Typical strain measured on the bottom of the plate during a gait trial.

A model was created to determine an optimal placement of the strain gage on the bottom of the X-ray transparent plate to yield a strain curve that rises and falls more quickly when the plate is loaded. The strain gage would produce a better curve if the strain changed abruptly enough to easily differentiate the signal from the noise. To do this, the gage should be placed closer to higher strain areas. In order to find higher strain areas, a finite element model was generated. The objective of this model was to provide a qualitative understanding of the strain distribution along the bottom face of the plate under a static loading condition.

All of the models were created and analyzed in Ansys version 16.2 (ANSYS, Canonsburg, PA). A single layer of shell 181 elements were used to simulate the plate since they are designed for transverse loads acting on planar surfaces. This element type is also meant for thin structures, with the thickness being less than one tenth of its length or width. The element can also be split into an odd amount of layers of differing thicknesses. The shell 181 elements allow for each layer to have different material properties and thicknesses. The amount of integration points through each layer was set to 3. The transverse strain was not an outcome of interest, so the default amount

integration points was used. The model was created as a plate with the length and width set to that of the real plate, and each element to have the thickness of the real plate. One element was used since the strain through the thickness was not a concern as the strain gages would only be applied to the surface. Also the model would undergo small displacements which would avoid stiffening of the model due to element locking. The mesh size was chosen to create a roughly square element in the plane of the top and bottom surface of the plate (24.7x24.4 mm) and more than 20 elements were used along any in plane direction to give a fairly high spatial resolution of strain. The model size was not a concern for computer processing time since the model was relatively small and it was a static analysis. No analysis on an optimum element size was completed as this simulation was intended for qualitative, not quantitative analysis.

Multiple versions of the model were created in increasing complexity to better simulate the plate and multiple boundary conditions were tested to more accurately constrain the model. The first version of the model did not take into account the complex structure of the plate. The real plate consists of a layer of foam sandwiched on all six sides by carbon fiber. The threads of the carbon fiber are laid perpendicular to each other. The plate measures 61.0cm by 91.5cm and 3.5cm thick. However, the initial model was created from a single homogeneous material, with the same geometry, and a modulus of elasticity chosen to be between that of the foam and carbon fiber (19.5MPa). Poisson's ratio was chosen to be 0.3. This model was then modified to be slightly more complex, with a less stiff material in the center to simulate the foam, and material on the top and bottom that was much stiffer to simulate the carbon fiber. The modulus of elasticity for each material was 275MPa and 68kPa and thicknesses of 1.5 and 32mm for the carbon fiber and foam respectively and a Poisson's ratio of 0.3 for both materials. The exact material properties of the

plate were unknown, so similar materials were found in a commercial parts store and those properties were used as an estimation.

Different boundary conditions were tested in the models due to the complex carbon fiber plate contact with the walkway. The real plate rested on four beams about 2.5cm wide around the perimeter. It is tightly fit between two adjacent floor panels along its long edges (i.e., at faces A and C in Figure 3.9), and it is tightly fit between vertical aluminum plates on each of the short edges near the corners (faces B and D). When the plate is under load, it may have some angular displacement (i.e., shear strain) along its edges due to bending. This press fit constraint would allow the long edges to contract but not expand between the confines of the adjacent panels. The short edges would also be able to contract and not expand where the plate was between the vertical aluminum supports, but where the short edges were not confined, it could rotate freely. The model was created two times with two different boundary conditions. The first condition had a zero translational displacement boundary condition on faces A, B, C, and D in the X, Y, and Z directions (Figure 3.9).The second model had all of the previous boundary conditions in addition to faces A, B, C, and D having a zero angular displacement boundary condition. Both models did not take into account that faces A, B, C and D could move inward (a press fit only constrains in the outward direction). Faces A and C were constrained in translation along the whole length of the plate in the model while the real plate is only constrained where the vertical aluminum supports contact the plate. The same was true for rotation of faces A and C.

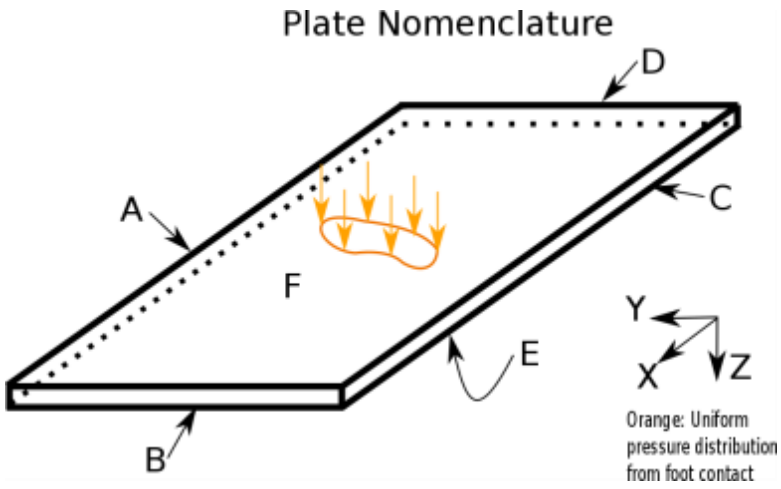

Figure 3.9. The labeled faces of the carbon fiber plate model.

The load on the plate was simulated by a rough approximation of a person standing static on the plate with one foot centered over the middle. The foot pressure was placed roughly in the shape of a foot centered on face F, the top of the plate. A uniform pressure distribution was assumed in the rough shape of a foot (24.4 x 7.41cm), and the magnitude of the pressure was roughly equivalent to a 36 kg person standing on one foot with a size 8.5 shoe (Figure 3.10). The body weight and shoe size of the person were chosen to be a worst-case scenario for producing strain: The lighter the person is and the larger the surface area that their weight is distributed over, the less strain would be seen by the plate. The load was also held low to ensure that the plate did not have large deformations which may void the model's validity.

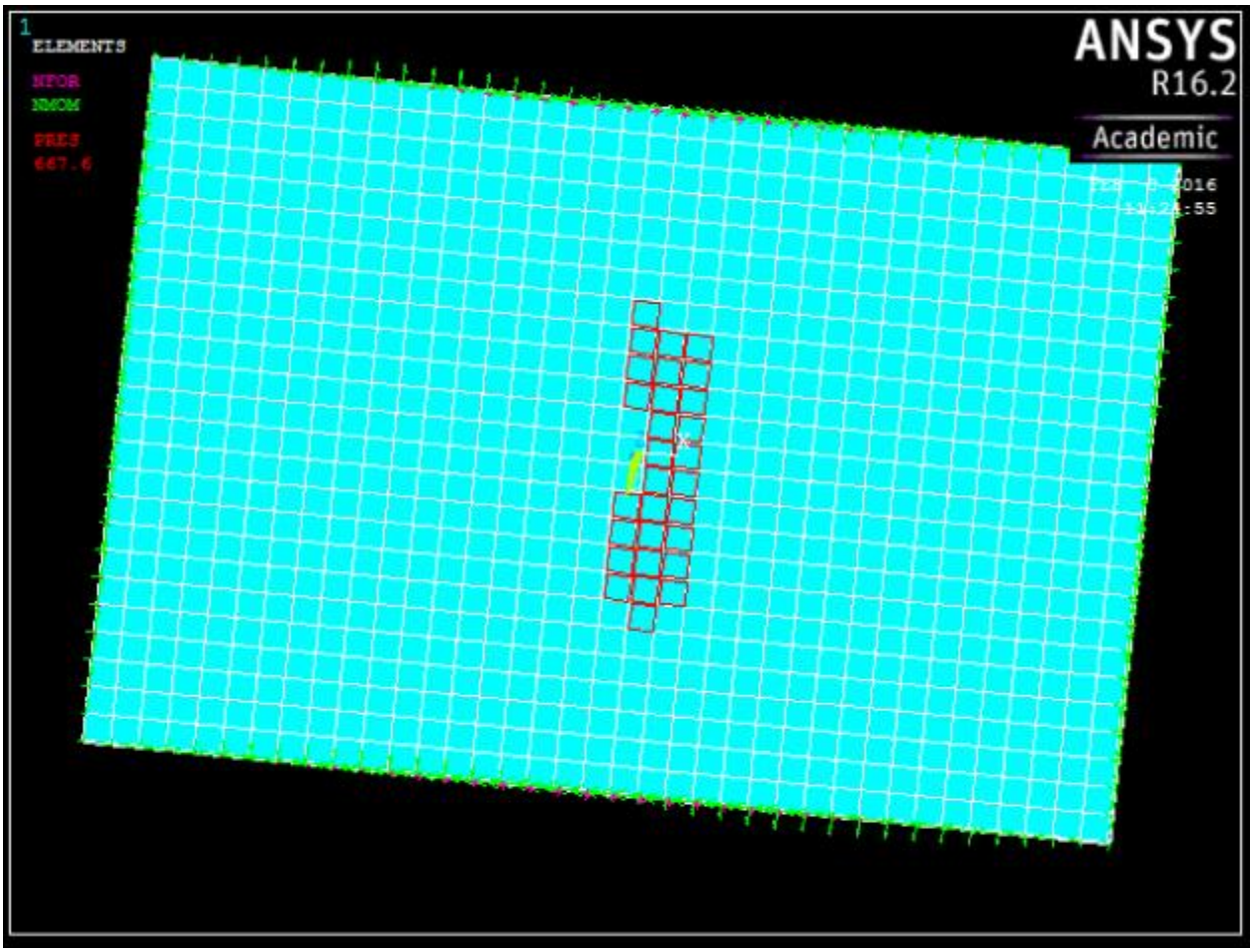

Figure 3.10. A top view of the model with the loading and boundary conditions displayed.

A plot of the Y direction strain (parallel to the short edge of the plate) shows a circular tensile strain distribution centered about the middle of the plate for the plate with all of the translation and rotation boundary conditions. There are two half ellipses centered on the long edges for compression (Figure 3.11). The highest tensile strain would be in the field of view which would not be a good location for the strain gage as the lead wires are visible in the imaging. The area under compression along the long edge of the plate would be outside of the field of view and has an equal but opposite magnitude of strain as the center of the plate. Placing a strain gage near the

center of the long edge may be better to measure strain of the plate than the location along the diagonal (located at the X) due to the higher strain concentration.

Since biaxial strain gages were used, strain in both the X and Y directions were considered in this analysis. The X direction of strain has a similar shape but it is rotated 90 degrees (Figure 3.12). This strain direction also has a high tensile strain near the center of the plate. The strain concentration also radiates outward to the center of the long edge which is higher than where the diagonal strain gage is located (located at an X). This analysis demonstrated that the in-plane strain components may be higher in the middle of the long edge of the plate than where the current strain gage is located. A second strain gage was mounted to the plate in the middle of the long edge to be more sensitive when a subject walks over it.

The validation tests later would be used to determine which gage location would be more sensitive to the foot contact. The orientation of the strain gages was not a concern because they are both biaxial strain gages. The signal from each element is combined in a way to produce the largest positive signal. The orientation of the strain gage would only change the magnitude of each element, not the total strain measured.

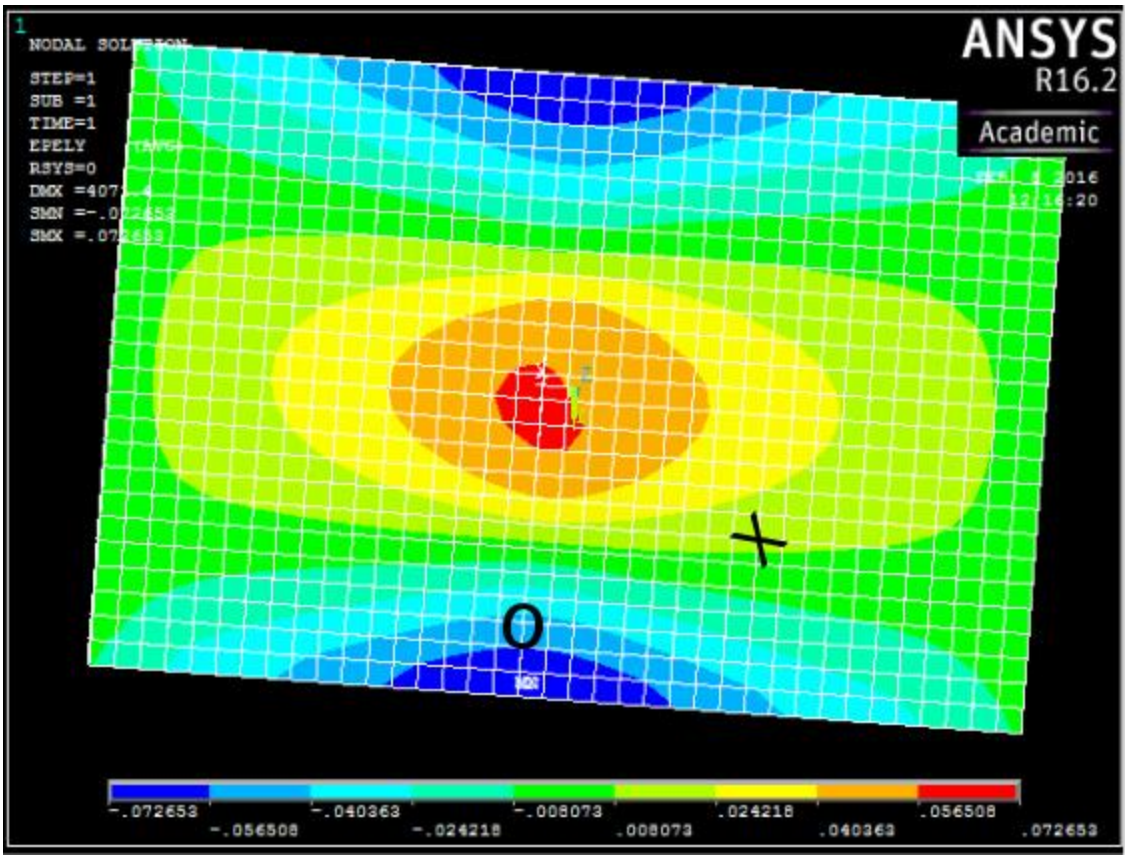

Figure 3.11. The Y direction (parallel to the short edge) strain magnitude of the underside of the plate with all of the translational boundary conditions (X,Y, and Z) and fixed rotation about the edges, with the approximate location of the strain gages.

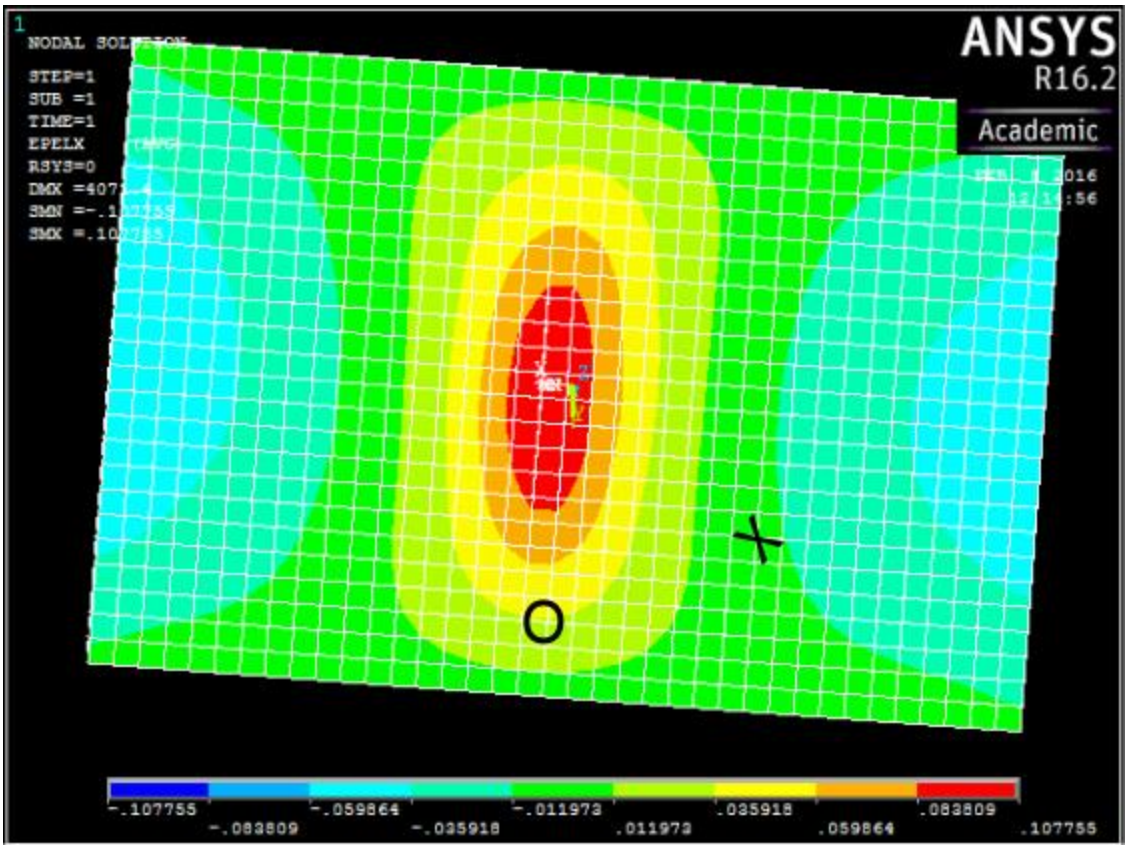

Figure 3.12. The x direction (parallel to the long edge) strain magnitude of the underside of the plate with all of the translational boundary conditions (X, Y, and Z) and fixed rotation about the edges, with the approximate placement of the strain gages.

3.5.9 *Determination of Strain Gage Placement*

Two strain gages were placed on the bottom side of the plate. One is along the diagonal, approximately located and oriented in the FE analysis figures by a black “X” on the bottom of the plate. Another strain gage was placed about 4cm toward the center from the middle of the long edge on the bottom of the plate denoted by the “O”. According to the FE model, the strain in this area would be greater than at the location of the diagonal strain gage. A validation experiment was completed to test which of the two strain gages would produce a better signal to detect heel strike

and toe off. The noise was quantified along with the strain difference between the loaded and unloaded position.

A simple static experiment was devised to measure strain for a period of time with the platform unloaded and loaded by a subject. The difference between in the strain in the loaded and unloaded conditions could then be compared to determine which gage was more sensitive to the loading. The strain was measured for 2500ms at 2000 Hz with no mass on the platform. A subject then stood with two feet on the center of the platform where one would step during a gait trial and strain was once again measured for 2500ms. The lead was then changed to the other strain gage and data were recorded once again. Then the subject stepped off the platform and with no load, the final measurement was taken. This yielded four measurements, one for each of the two gages in a loaded and unloaded position. The subject stood on two feet instead of one to increase stability and reduce sway as data were collected. The two-footed stance may change how much strain the plate had, but it was the same load in the same location for both trials. The movement of the lead wires could cause added or decreased strain between measurements of the different gages but the lead wire would be in the same place for the loaded and unloaded trials for each position. The only change would be the strain read by the strain gages.

The difference in strain and the signal change to noise ratio were calculated. The signal is the average value of the loaded plate minus the average value of the unloaded plate. The uncalibrated strains were 1.40×10^{-5}V and 1.28×10^{-5}V for the diagonal and long edge strain gages respectively. The signal change to noise ratio was 2.89 and 3.95 for the diagonal and long edge strain gages. The gage on the diagonal was more sensitive, but had much more noise. The strain gage on the long edge had a much cleaner signal and would be used in future data captures. The

larger noise could be from the application of the strain gage. Another strain gage could be applied to the bottom of the platform along the diagonal and the test could be redone.

Subsequently, the plate was oriented 180 degrees from its original position to move the strain gages further from the subject's starting position. As heel strike produces a much more abrupt change in strain than toe off, it was desired to orient the plate such that the strain gage was more sensitive to toe off than heel strike. This change could improve the ability to differentiate more of the toe off signal from the noise.

3.6 Validation Procedure and Theory Through Impulse Testing

A validation was completed to test the temporal accuracy of the strain gages for versions 2.1.2 and 3.1.1. The goal of the validation was to determine if the software and hardware configuration could detect when a hard plastic ball made contact with the plate through the use of a strain gage within 1 ms of when the high speed images recorded contact. The procedure is listed as follows, and the results are in the appropriate sections below. Version 2.1.2 did not have precise enough timing to detect when the impact occurred, so it did not undergo testing with a human subject.

3.6.1 *Rod Drop Testing*

3.6.1.1 Procedure and Theory

A timing test was created to determine the temporal accuracy of the strain gage measurements to the images recorded on high speed camera. The objective was to determine if the increase in strain occurred when a rigid object appeared to be in contact with the plate determined by analysis of the high speed camera images. This test was a clean way to detect contact with both modalities. In

future tests, the strain gage alone would be used to determine contact due to multiple difficulties in determining when a foot/shoe is in contact with the plate through image analysis. Some of the issues with determining foot/shoe contact are overlapping bones, soft tissue compression, and part of the foot being out of the field of view. Heel strike defines the start of stance phase and the heel may not make contact with the plate in the field of view if a forefoot imaging gait trial is taking place due to the small image capture volume. The same could be true with toe off when a hindfoot imaging trial is completed. The strain gage would be used as an independent measure of contact.

The test consisted of dropping an aluminum rod (830 x 30mm) with a very dense plastic ball (40mm diameter) rigidly attached to its end into the field of view onto the carbon fiber plate while recording its movement with the high speed cameras. The dense plastic ball provided a high contrast to the aluminum rod and air around it for better image registration. A template matching algorithm was used to register the centroid of the ball in each fluoroscope frame, and the direct linear transform (DLT) was then used to locate the ball centroid in three-dimensional space, given the known fluoroscope geometry (determined from system calibration). A person manually released the rod/ball allowing it to fall ball side down under gravity and bounce off the plate once. The rod was long enough for the user to remain outside the field of view while releasing and catching the rod to minimize radiation exposure. The rod was dropped from a height of about 300mm to create a large enough impulse to track using the strain gages without damaging the plate. This was determined through a series of pre-validation trials which consisted of dropping the rod at increasing heights until the strain profile became large enough to easily differentiate from the signal noise. The images were recorded at 1000Hz while the strain and trigger signals were recorded at 2000Hz. A reference time was needed to be able to compare the strain contact and image contact timing. The trigger signal sets the current camera frame to zero when it is sensed

by the camera. All of the other frames are marked with their relative times to this frame. The time between the trigger signal and the frame that captured contact is known. The strain signal is captured on the same time base as the trigger signal. The time before the trigger signal that the strain signal increases is then known. The relative time from the trigger signal to contact for each measurement (strain and image) can be compared. The strain gage time of contact was defined as when the strain signal was outside of its steady state noise range. The definition of contact for the image analysis was when the ball's velocity began to increase (positive acceleration) greater than its noise range. For the system to successfully be able to determine contact through strain, the time at which the strain gages sensed contact and the time at which image that captured contact was to be less than 1 ms.

3.6.1.2 Rod Drop v2.1.2 Scan Frequency 2000 Hz Results

Version 2.1.2 was tested in the validation as it was one of the simplest VIs, only reading data from the strain gages and Arduino. Version 2.2.1 was being constructed when this test occurred, and it added more complexity because signals were being read and written. If v2.1.2 passed the validation, then v2.2.1 would have been tested. Three trials were conducted and the strain lead the image of contact by 92ms, and 119ms, and another trial the contact image lead the strain by 24ms. The temporal accuracy was well outside of the tolerance specified of 1ms and furthermore the temporal shift was not constant or repeatable. The prototype was thus assessed to not be able to accurately or reliably detect when an object was in contact with the plate.

After further evaluation and research there were two main reasons for the discrepancy in timing. One was a programming error and the other is a limitation of the hardware. The programming error involved the read functions that are used to convert the hardware signals (analog input and strain) into data points. There were many iterations of this software but the one

tested contained two read functions. One read VI was for the analog input signals which read all of the signals in and out of the Arduino (fluoroscope firing, pretrigger, trigger, IR gate one and two). The other read VI was for the strain gage signals. The read VI is a blocking function, meaning LabVIEW can only complete one of the two VI executions (function evaluations) at a time (the write VI also a blocking VI). The read VI takes in the hardware signal at the specified data collection frequency and sends it to a buffer. The data points are then passed from this buffer to the rest of the program. If a single function were to be used, it would execute the whole time with no interruptions. This would ensure that the data points would be read in sequential order with no gaps. Only one of the two read VIs can execute in the same while loop which would cause the other one to pause. If a function is paused for a period of time, it does not have any inputs to tell when and how long it was not collecting data. When it starts reading data again it would not take into account the time it was inactive, possibly creating gaps in the data. These gaps would be unknown to the user since all of the data points fill an array with no indication of when each data point was taken. One way to fix this problem would be to put the two read VIs in different loops. The timing of the loops can then be synchronized, and the data could be appended into a single array after execution. This option was not explored any further because the hardware limitations would still be a predominant problem that would not allow the needed temporal accuracy of 1ms. The hardware limitation is that the program is running on a desktop computer with many other applications and programs. The operating system does not and cannot prioritize LabVIEW data collection over other processes that may appear. This will introduce latency and data collection will not be completed in a deterministic fashion with the 1ms timing accuracy required. The solution was to purchase a RT system with FPGA for data collection. This combination can read and write multiple signals to multiple locations simultaneously without latency.

3.6.1.3 Rod Drop v3.1.1 Scan Frequency 2000 Hz Results

The same rod drop test was completed with v3.1.1. Two trials were completed with images captured of the hard plastic ball contacting the plate while strain data were collected. For one of the trials the original impact is captured over 3 frames. The duration of the strain impulse measured by the strain gage lasted for 3.5ms, matching the strain gage duration, followed by 7.5ms of ringing artifact (Figure 3.13). The maximum strain occurred at the same time as the minimum position of the centroid of the hard plastic ball. Similar results were found for the one other trial with the strain lagging the image data by 1ms. The velocity of the rod was calculated and plotted with the strain data (Figure 3.14). The velocity passes through zero when the strain is at its maximum, as would be expected from the position and strain plot. The moment of contact could be determined by the increase in velocity of the rod as it contacts the plate. Through the image analysis, the rod greatly changes velocity at time -982ms, and the strain begins to rise at -981ms. The strain data lags the image data by 0.5 to 1ms, as the strain data at -981.5ms did not greatly change. This small discrepancy in timing could be due to a small deformation of the plate and/or plastic ball. For 0.5ms, the deformation could be small so that the strain gage was not sensitive enough to measure this change in strain. Another reason for the strain latency could be that the impact of the rod caused a wave of deformation through the plate. Some amount of time must elapse between the impact and the propagation of that impact to the strain gage (located on the underside of the plate), so the strain gage will necessarily measure the strain change after the impact. An upper bound for this propagation time was estimated. Under the assumptions of the wave speed in the plate is equivalent to the speed of sound in air (34,300cm/s) and the distance from the impact to strain gage location is 26cm (from physical measurements), the wave would take 0.7ms to reach the strain gage. This is an over estimation of time since the wave would propagate faster in the carbon fiber because it is much denser than air. A third source of error could be the timing delay between

when the trigger signal was sent out and when the zero frame was taken. The trigger signal could mark the next frame up to almost 1ms before the zero frame is taken. A greater strain sampling rate could offer more information to characterize the delay in the strain so another test was proposed with the strain scan frequency at 5000Hz. The results of the current test do show that the abrupt change in strain can predict the contact of the ball with the plate. This data suggests that when the strain increases above the noise band, the previous frame of the imaging sequence should be chosen as the frame of contact.

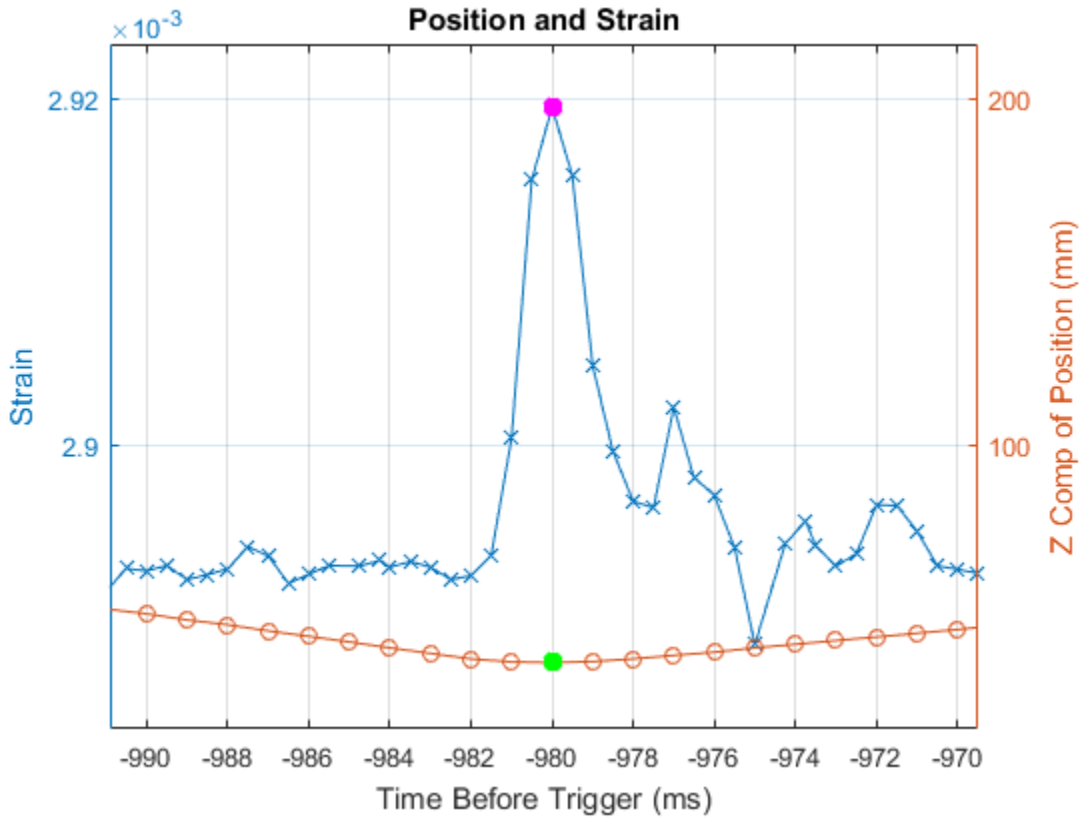

Figure 3.13. A representative plot of the vertical position of the plastic ball and plate strain while completing the rod drop test with the minimum vertical position highlighted in green and the corresponding strain highlighted in magenta on the biplane control setup v3.1.1 and a scan frequency of 2000 Hz.

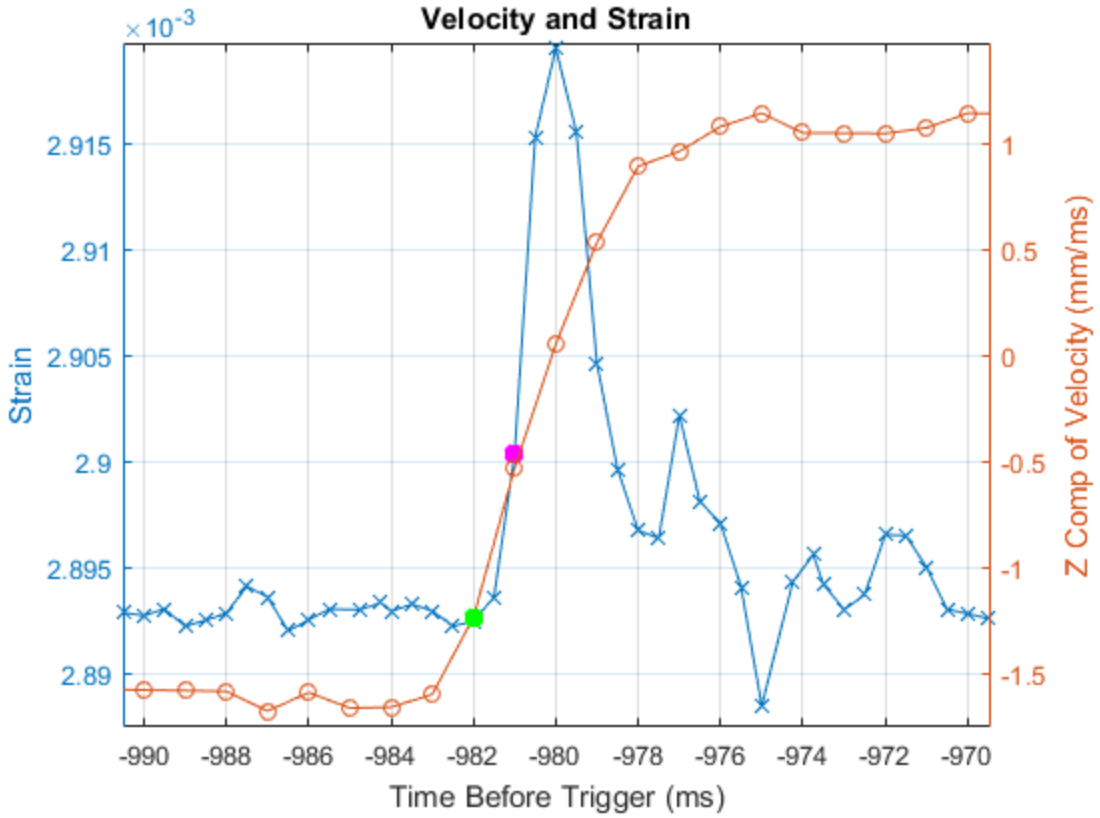

Figure 3.14. The velocity and strain during a representative rod drop trial with the first frame indicating a large change in velocity highlighted in green, and the first data point indicating a large change in strain highlighted in magenta on software v3.1.1 with a scan frequency of 2000Hz.

3.6.1.4 Rod Drop v3.1.1 Scan Frequency 5000 Hz Results

The strain data during the rod drop testing consisted of less than half a dozen points characterizing the strain impulse. A finer temporal resolution was used to more accurately determine the strain impulse when the ball made contact with the plate. Three trials were completed with the strain scan frequency of 5000Hz. The first goal was to determine if the temporal accuracy would increase if the scan frequency was increased. The bridge completion module filters the strain before it is sent into the LabVIEW software and this filtering creates a calculable delay. A secondary goal was to verify that the strain delay at the new scan frequency was the duration stated by the given

formula (3.6) from the manufacturer. and that there were no other latencies that could be accounted for.

$$\frac{38.4}{\text{Fs}} + 4.5e^{-6} = Input\ Delay \qquad (3.6)$$

For a sampling rate of 2000Hz, this delay is 19.2ms and was used in the timing calculation of the previous validation test, and the current test was conducted at a scan frequency of 5000Hz, and the calculated delay was 7.8ms. Both of these scan frequencies were used because they are integer multiples of the camera frame rate.

The position and the velocity of the ball were calculated over all of the video frames where the ball was completely in view. The ball reached its lowest position 0.4ms before the strain reached its peak (Figure 3.15). An abrupt change in velocity should correspond to the increase in strain, as that is when the ball first contacts the plate. The velocity begins to increase at time -849ms, while the strain begins to rise at time -848.4ms (Figure 3.16). This result shows that strain data taken at a scan rate of 5000Hz can better predict the contact of the ball to the plate than at 2000 Hz but still contains some latency as the current test had 0.6ms delay opposed to the 2000Hz test which had a 1ms delay. The other tests had similar results with the strain lagging the image data by 0.6 and 0.8ms. Even with the higher scan rate, the image taken before the strain has an appreciable increase should be marked as the frame displaying contact.

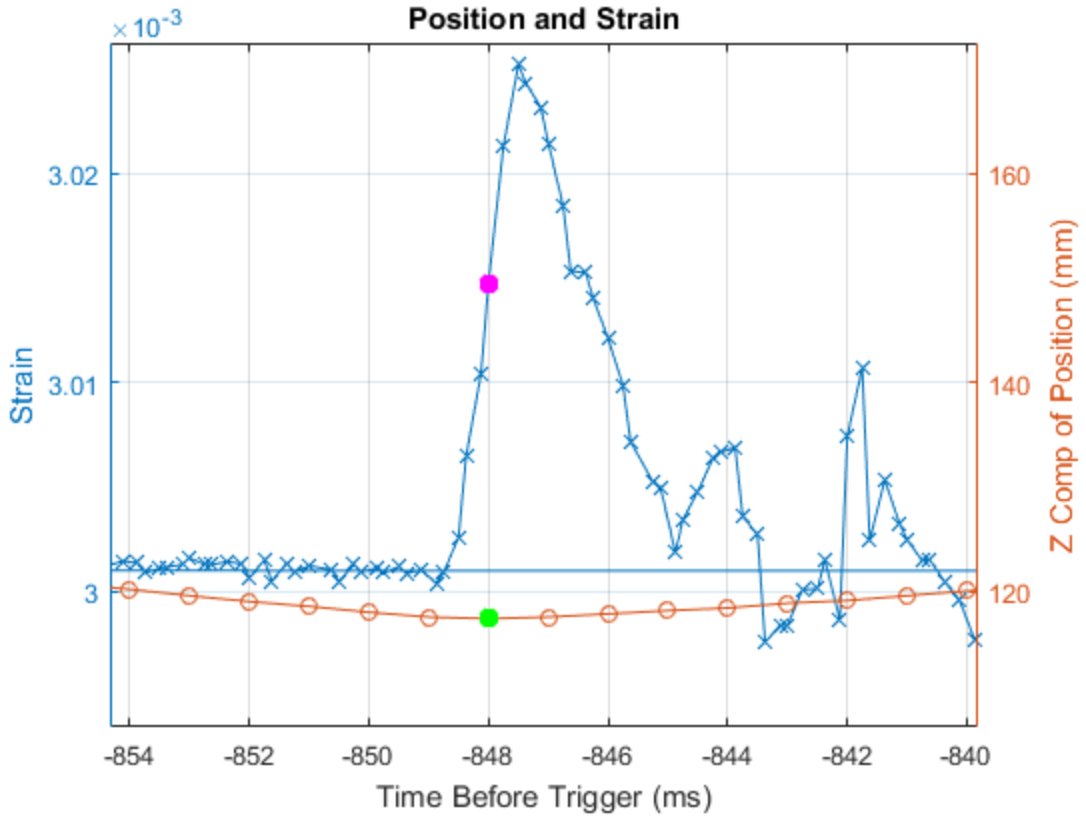

Figure 3.15. A representative plot of the vertical position of the plastic ball and plate strain while completing the rod drop test with the minimum vertical position highlighted in green and the corresponding strain highlighted in magenta on the biplane control setup v3.1.1 and a scan frequency of 5000Hz.

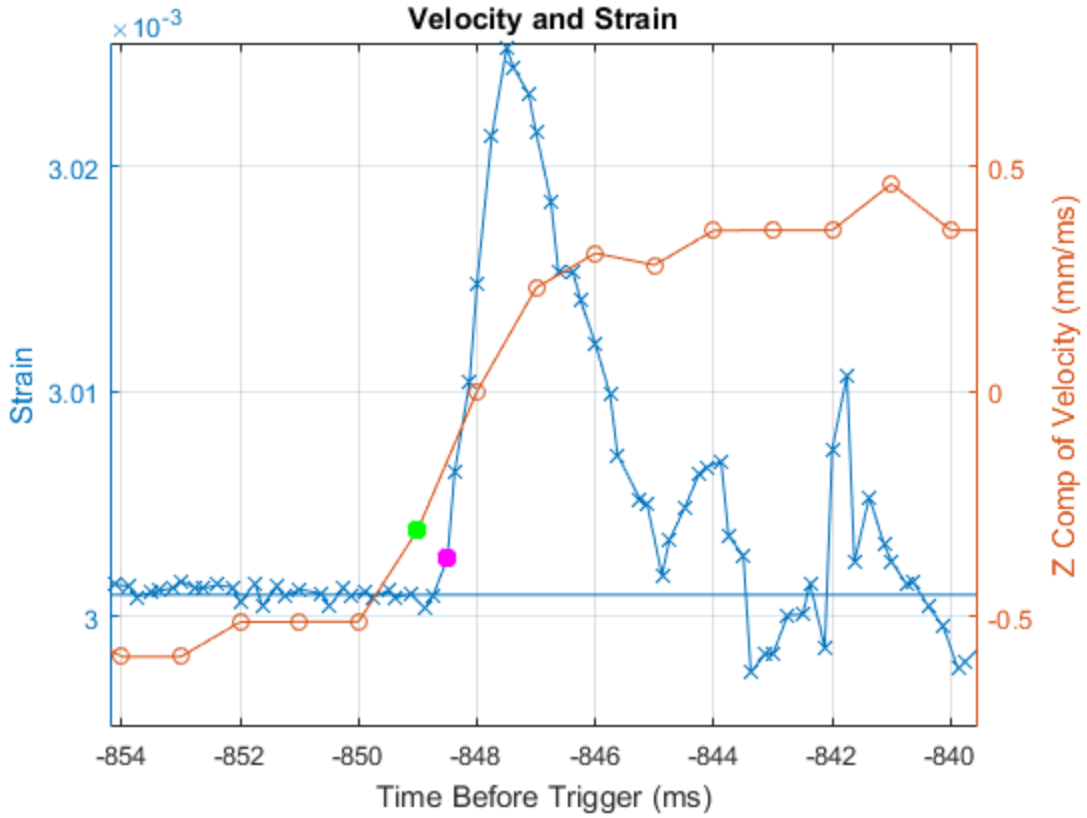

Figure 3.16. The velocity and strain during a representative rod drop trial with the first frame indicating a large change in velocity highlighted in green, and the first data point of indicating a large change in strain highlighted in green on software v3.1.1 with a scan frequency of 5000Hz.

3.6.2 *Barefoot Subject Walking*

3.6.2.1 Procedure and Theory

The purpose of this test was to compare bone images of relatively high quality taken during a gait trial to the strain gage data. The gait trial was focused on the hind foot, which consisted of a gait trial where the subject's foot was biased so that the heel was closer to the center of the field of view during midstance. The bone image data are considered high quality because it is from a healthy subject, with good bone density, walking barefoot. This creates the highest contrast between bone and soft tissue, allowing for the cleanest bone tracking kinematics. Both the

geometric centroid and the closest point on the surface of the calcaneus to the walkway were tracked from the very end of swing phase (prior to heel strike) and through stance phase until the calcaneus exited the field of view (after heel rise, but not toe off). It was determined that the centroid is not an ideal point to track due to the rotation of the calcaneus as the foot goes to foot flat after heel strike. To get a better estimation of when heel strike occurred, the lowest vertical point on the calcaneus (the closest point on the surface of the calcaneus to the floor) was tracked for all points in time. This lowest point will change over time since the bone is rotating and has irregular geometry. The lowest point will move along the bottom surface of the bone, and will not be as affected as the geometric centroid to calcaneal rotation. The moving point on the surface of the calcaneus will be closer to the axis of rotation of the calcaneus as it goes to foot flat (axis is located external to the bone, at the heel pad and floor interface). The position and vertical velocity of the centroid and the lowest point on the calcaneus were tracked over time and compared to the strain of the plate to determine the temporal accuracy between when the images and strain showed contact.

3.6.2.2 Results

The centroid of the calcaneus was tracked first in the analysis. The position of the calcaneus was tracked as it entered the field of view noted by the sharp downward slope of the red line (Figure 3.17). The calcaneus left the field of view before stance phase finished denoted by the end of the red line before the strain returned to its pre-contact value. The strain follows a double hump pattern, but the second hump is much larger due to the placement of the strain gage which is closer to where the toe landed on the plate. The calcaneus had a two part downward trajectory. The first part is when the foot is moving closer to the floor. The second is after the heel pad initially contacted the floor and the foot is advancing to the foot flat part of stance phase denoted by the abrupt rise

in strain. The centroid continued downward but at a slower rate. During this time the heel pad is compressing and the calcaneus is pivoting forward on a more posterior point than the centroid. This would cause the centroid to pivot downward as the foot goes to foot flat. The centroid starts to rise halfway through stance phase as the heel lifts off the ground.

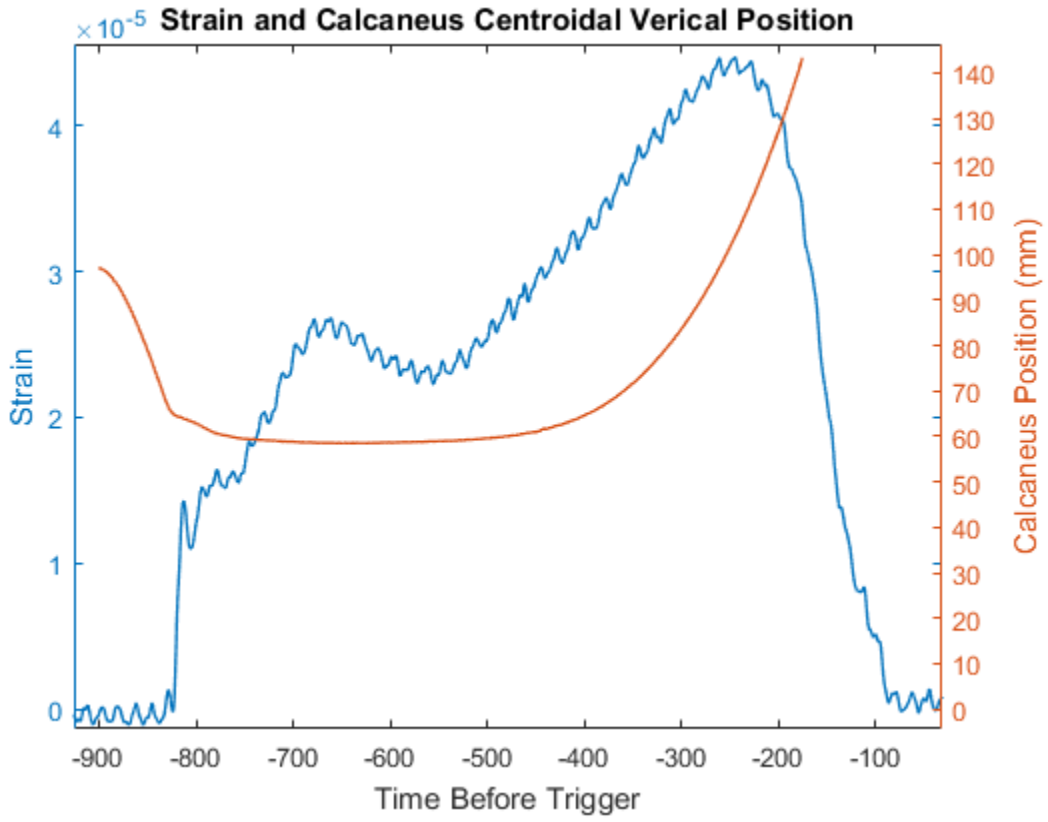

Figure 3.17. The vertical position of the centroid of the calcaneus and strain during a barefoot gait trial.

The position of the centroid of the calcaneus in the vertical direction was differentiated once to give the vertical velocity of the centroid, and was plotted against strain (Figure 3.18). The steep rise in strain lags the rise in velocity by around 8ms. The heel pad is much softer and compresses much more than the hard plastic ball used in previous validations so some lag is expected. The heel would compress some before there was an appreciable rise in strain. This test

was used more as more of a sanity check, as the strain and the determination of contact would have to be tuned for each and every subject, as the strain would lag by different amounts due to heel pad softness. Many walking trials could be completed with the same subject and this lag could be quantified. A different lag would be calculated for each different subjects due to the differing heel pad thicknesses and compressibility.

Overall, the strain provides an accurate and reliable method to calculate contact with the carbon fiber plate shown through the rod drop testing, and checked with the human subject test. There are some variables such as wave propagation, and sensitivity to low strain when a heel first contacts the plate. These could amount to 8ms of time difference between the actual and measured contact time.

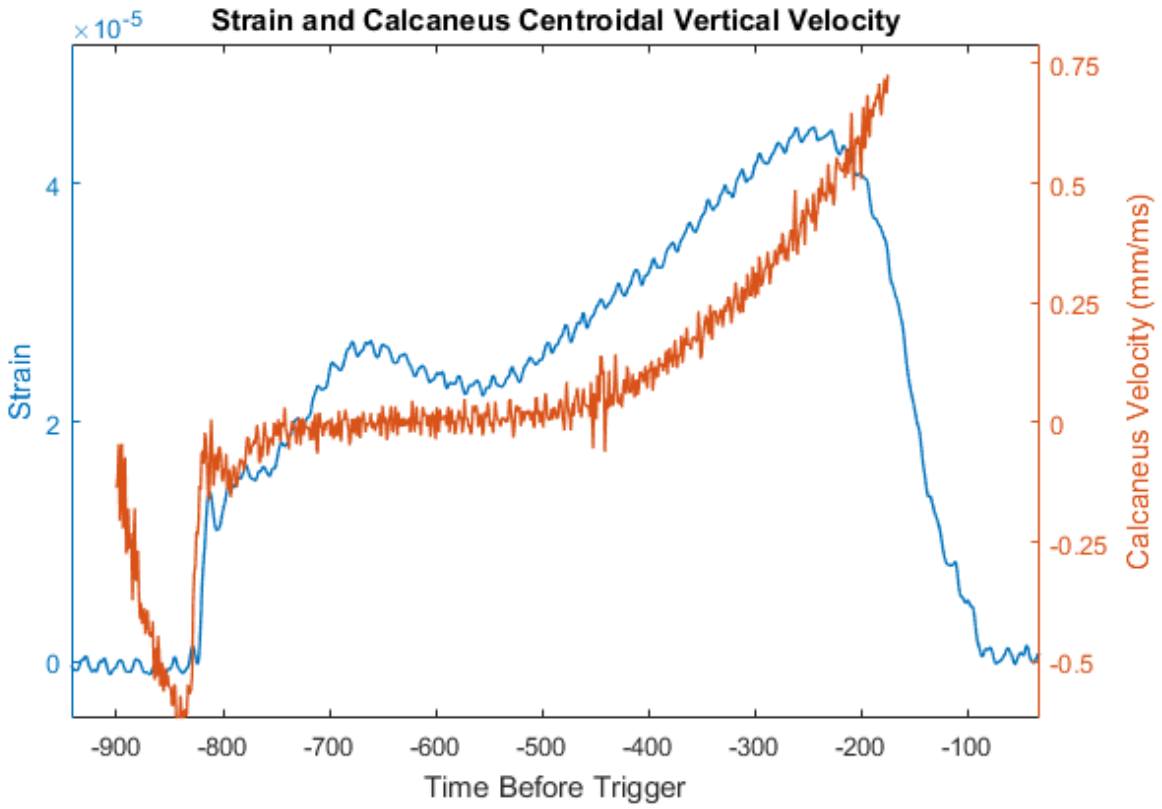

Figure 3.18. The centroidal vertical velocity of the calcaneus and strain during a gait trial.

3.7 DAILY USE

This section covers how the system would be used in its current form in routine data collection. The Phantom software is used to capture and save the image data. LabVIEW sends out signals for the pretrigger and trigger events for the cameras.

3.7.1 *Procedure*

3.7.1.1 Start up

1. Plug in Real Time hardware, network switch, and turn on infrared (IR) gates, cameras, and fluoroscopes. Configure the fluoroscopes to their desired imaging settings. Note: this guide will not cover detailed fluoroscope settings and adjustments.
2. Open ***Phantom 675.2*** software to control the cameras.
3. In the Phantom pop-up windows configure the time if desired. Afterwards the time should be reset in both cameras using **Acquisition>Camera Clock>Set Time** then **Close**. To synchronize the other camera's clock, select **Acquisition>SetUp and Recording…** and select the other camera from the pull down menu in the top right of the pop-up, and follow the previous step to **Acquisition>Camera Clock>Set Time**, as this will set both cameras to the same time. This step ensures synchronous timestamps in the two videos.
4. Set the proper parameters by starting in the top menu **Acquisition>Camera Clock>Set Time**
    a. A live feed will be displayed with the parameters on the right. Select the appropriate ones for the data capture, and then click **Current Session Reference** to take a black reference.

b. The **Im. proc…** button may be needed to configure the saturation, brightness and other video settings.

5. Open ***LabVIEW 2015 (32-Bit)*** software, and place *Phantom* windows on right computer monitor, and *LabVIEW* on the left (wider monitor).
6. Select ***BiplaneControlGroundUp.lvproj*** from the Recent Files subwindow, or search for it through **File>Open**.
7. A project window will open and the ***UIMain.vi*** and ***RTMain.vi*** need to be opened by double clicking them in the project window.
    a. It may be necessary to expand or collapse certain folders in the project manager to find the desired files.
    b. OPTIONAL: The ***FPGAMain.vi*** can also be opened for the user to see the variables as they populate the FPGA, but running this VI is not necessary and all indicators will be redundant to the UI.
8. In the top left of both VI windows that opened, press the **Run Once** button which is a single white arrow pointing to the right, start with ***RTMain.vi*** then the ***UIMain.vi***.
    a. If run in this order the UI will automatically connect with the RT, if not the connect button will need to be pressed on the ***UIMain.vi*** front panel.
    b. It will take a couple of seconds for the VIs to deploy.
    c. The ***RTMain.vi*** front panel can now be minimized.

3.7.1.2 Using the VI

1. First a dialogue box will prompt the user to change the file path and the file name. An arbitrary file and name are preset. Before going onto the next step it may be beneficial to change these fields after **OK** is pressed.
    a. The *Full File Name* will not populate until the data are saved.
2. If the ***RTMain.vi*** was not started before the UIMain.vi, press the **Connect** button near the top center of the front panel to connect the UI to the RT, and the *Connected?* light next to the button will light up.
3. Scan all of the other lights to make sure that they are off. Only one other light should be on, *Fluoro Switch On* or *Fluoro Switch Off*.
    a. If the fluoroscopes are not powered, then the *Fluoro Firing?* Light will be on as well. The signal is at 0V with the fluoroscopes turned off which is the same voltage as if the fluoroscopes were firing.
4. Use the arrows or the pull down menu on the **State** control to choose a state for the FPGA to go into.
5. Make sure the fluoroscopes are at the proper settings for Scan Type and KV/mA.
6. Toggle the emergency cutoff switch which is on the BNC cable from the FPGA to the fluoroscopes if the *Fluoro Switch Off* indicator is illuminated.
    a. This will allow the FPGA to control the fluoroscopes.
7. Make sure the *FPGA Controls* indicator is populated with the desired parameters.
8. In the Phantom software window *Camera:Preview*, make sure the cameras are in the state *Preview Waiting for Pretrigger…* in the bottom most text bar of the window. If not press **Capture** or **Abort cap.> Yes** until the state is displayed. WARNING: make sure the other camera is in the *Preview Waiting for Pretrigger…* state.

9. Press **ARM FLUORO** then **Execute Current Mode?** to start the data capture. WARNING: fluoroscopes will fire.
    a. At this point the protocol deviates slightly depending on whether the trial is considered static (user input starts capture) or dynamic (IR gate 1 trip starts capture).
    b. Static – *Recording Data* light turns on along with *Firing Fluoro?* and possibly *Pretrigger* and *Trigger* lights.
        i. *Pretrigger* and *Trigger* may not turn on if they stay on less than a loop iteration time on the UI, as their states change faster than the UI can read it. This does not affect the timing of the pretrigger and trigger signals themselves, but only the graphic display on the UI.
    c. Dynamic – The *Waiting for Subject to Start* light is illuminated, along with the *Recording Data* light. This indicates that the system is armed and the subject should now start walking and trip IR gate 1 to initiate data collection. The rest of the lights will light up as mentioned under the static case.
        i. The system can wait indefinitely for the subject to trip IR gate 1. Once tripped, the system will only collect at most 10 seconds of data after the IR gate is tripped, and the fluoroscopes will only be on for the specified time.
        ii. The data collection will end either when the subject trips IR gate 3, or if the user presses **Emergency Stop. T**he system will not timeout. If the **Emergency Stop** button is pressed, then **Undo Emergency Stop** has to be pressed to reset the system for future data collections.

iii. The on signal for the fluoroscopes is initiated after a specified delay after the falling edge of IR gate 1 (i.e., when the subject first blocks the IR beam). So a subject who arrives at the field of view 7 seconds after crossing IR gate 1, and the fluoroscopes are set to only fire from seconds 2 to 5 after IR gate 1 is crossed, will not be imaged.

10. After the collection is complete a dialog box will pop-up prompting the user to save the data collected. Press **Yes** to save the data, which also populates the two graphs *Strain* and *Data*.
    a. If the file name/path is not correct the user can select **NO**, change the data fields and then press **Save Data?** or it can be pressed at any time after the collection but before the next collection.
11. Repeat the current section, changing the name and file path, and state as necessary.

3.7.1.3 Shutting Down the System

1. Change the hardware emergency stop switch to the off position.
2. Turn off fluoroscopes (emitters then towers).
3. Click **Exit** on the *UIMain.vi* front panel. The UI VI and RT VI will stop running. If they do not, the **Abort VI** button on next to the **Run** and **Run Continuously** buttons can be used.
    a. Use the **Abort V**I button on the *FPGAMain.vi* if it was started.
4. Close the VI windows, and the VI project.
5. Exit any subwindows and close the Phantom 675.2 software.
6. Transfer any data if necessary (need to unplug RT ethernet cord from computer and plug in internet ethernet cord, switch cords back after data transfer).

7. Turn off cameras and IR gates through power strip.
8. Turn off computer if desired.
9.

3.7.2 *Safety Procedures*

To prevent excessive or unnecessary irradiation of the subject, a number of software and hardware safeties have been implemented to turn off the fluoroscopes. The fluoroscopes will only be on for a specified period of time but they can be forced to stop by the user. There are two ways to manually stop the fluoroscopes from firing during a data capture. One is to press the Emergency Stop button on the front panel of the VI which sends a software stop. The other is to flip the emergency switch on the fluoroscope BNC trigger wire. This hardware stop physically opens the circuit so that the signal will not reach the fluoroscopes to fire the fluoroscope.

3.7.3 *Common Changes to the System*

If the preset parameters are not adequate for the data capture needed, they can be changed on the block diagram. Open the block diagram to the *UIMain.vi* VI; the parameters are in the uppermost loop. The event structure should be changed to *state*, and then the proper state should be selected in the case structure (**Error! Reference source not found.**). Next to the while loop is a list of the ariables in order along with units. Change the variables to the desired values, then save the VI. Go back to the front panel and click run once, and the new parameters will be used when the appropriate state is selected. The calibration state is meant to be used for any data capture where the user wants to fully control when and how long a data capture occurs. The localization state should not be changed unless it is to obtain a better image of the localization block. The same is

true for the distortion state except that it is meant to be optimized for the distortion correction plates.

3.7.4 *Helpful Hints*

The emergency switch (physical one connected via BNC) can be turned to the off position if the user wishes to collect data (including sending the fluoroscope firing signals) but without the fluoroscopes actually firing. This can be used without changing the parameters in the software (Static or Dynamic Capture modes).

This can also be used to run a static trial once if the data did not transfer properly from the FPGA to the RT in the previous trial. During a normal data transfer with no errors, all of the signals will be between 0 and 5 V, with one signal captured per channel. If the signals switch channels (signal to channel indexing error) causing an error in data transfer, the index or time may be recorded in the y axis, instead of the x axis. The graph is set to automatically change its bounds to fit the data. These two signals have a max around 5,000 and 10,000 respectively, and would push the bounds of the graph up to those numbers. The graph would appear to have only two lines that grow in a linear fashion. By running one static trial, the user can be sure that all of the old data are cleared out of the DMA FIFO so that subsequent trials do not contain spurious data.

One additional issue can arise for subjects walking particularly quickly (> 1.8m/s). The fluoroscopes require, as a safety precaution, for the on signal to persist for at least 500ms prior to firing. As this 500ms period can begin no earlier than the IR gate 1 falling edge (as that is what's used to start the 500ms delay), this can cause the subject to pass through the imaging field of view prior to any fluoroscope firing. To work-around this, IR gate 1 can be tripped externally (for

example, by a hand) and then a period of time can elapse before having the subject proceed down the walkway. This will ensure the fluoroscopes are firing when the subject is in the field of view.

3.7.5 *Front Panel Controls and Indicators*

The front panel is where the user interacts with the VI to control the biplane system. There are many controls and indicators to interact with and this section will describe how to read and use them.

3.7.5.1 Indicators

Data – This graph contains all of the AI and AO signals collected during the last trial (single state where data were collected, as in a gait trial), and is populated afterwards.

DMA Time Out? – This illuminates when the DMA FIFO is full which may cause data to be lost.

Connected? – Illuminated if the message stream between the UI and RT is working.

Firing Fluoro? – Shows whether or not the FPGA is sending out a signal that would cause the fluoroscopes to fire. A light on means fluoroscopes should be firing.

Fluoro Switch On (Off)? – One of these two lights is illuminated depending on the position of the hardware switch located on the BNC cable. On signifies that the fluoroscopes would fire if the signal was sent to them.

FPGA Controls – This cluster is populated with all of the parameters that will be sent to the FPGA when the Execute Current Mode? control is pressed.

FPGA State – The current state of the FPGA. This variable updates every 50 ms or however long between lossy iterations of the lossy data loop on the UIMain.vi.

Full File Name – The path and file name to be saved; this is populated after the file is saved.

IR Gate # Tripped? – Shows whether or not the respective (1,2,3) IR Gate's beam is broken.

Strain – After a trial has completed, this graph populates after a data collection has finished with the strain measured from the gage under the carbon fiber platform for the whole duration of the data collection.

Must Press Arm Fluoro First – An indicator designed to let the user know they pressed the Execute Current Mode? button without pressing the ARM FLUORO button first.

Press Undo Safe Mode to Continue – Indicates that the user pressed the Safe Mode button and safe mode needs to be undone by pressing Undo Safe Mode before capturing more data.

Walking Speed – The average speed at which the subject walked between IR gates 2 and 3, and is populated after any data capture. Static trials tend to yield Inf.

Recording Data – The RT is polling the Target to Host DMA FIFO, or it is reading data from the FIFO.

Safe Exit – Illuminates when the exit button is pressed to signify that the UI and RT were stopped and the FPGA was placed in Safe Mode.

Save Error? – Displays whether there was an error in saving data or not with the appropriate error code and description.

Waiting for Subject to Start – A gait trial has been started and the subject has not yet passed in front of IR gate one. The subject should proceed down the walkway tripping IR gate 1 to start the data acquisition.

3.7.5.2 Controls

Arm Fluoro – The first of two button presses needed to allow the fluoroscopes to fire and data acquisition to begin.

Comments – Add additional comments to the save file to note

Connect – Open communication between the UI and RT.

Emergency Stop – Stop the FPGA in the middle of data collection, including the fluoroscope firing, and places the FPGA in Safe Mode.

Execute Current Mode? – The second of the two button presses needed to fire the fluoroscopes and collect data.

Exit – Stop the UI VI and RT VI, while putting the FPGA in Safe Mode. Communication streams are also closed, and will not be opened until LabVIEW is restarted.

File Name – The name of the file to be saved. It is auto-incremented if the file already exists.

File Path – The path of the file to be saved. If the specified folder does not exist, it is created.

State – Choose a state for the FPGA to execute. These are all of the different data collection modes that are preset, each with their own unique parameters.

Undo Emergency Stop – Resets the stop commands sent to the FPGA when Emergency Stop was pressed. This has to be completed to take data after Emergency Stop was pressed.

Zero Strain Gage – Takes a single sample of strain and saves it. The strain is then subtracted from this value so that the new strain is around zero.

3.7.6 *Compiling the FPGA*

If any of the code is changed in the *FPGAMain.vi*, then the FPGA has to be compiled. Reasons for a compilation or recompilation include the user changing the code of the source file for the FPGA, which can be as little as changing the value of a constant, or even changing the path of a wire. Sometimes a The LabVIEW graphical code is transformed into a bit file that determines the state of all of the gates in the FPGA to run the code through the Xilinx compiler built into LabVIEW.

Currently the compilation process completes in about 15 to 35 minutes. All of the current build specifications are listed in the project window under *RT CompactRIO Target > chassis (CRIO-9064) > FPGA Target (RIO0, cRIO-9064) > Build Specifications*. The file with the green box around the icon is the default build. All of the builds can be right clicked and select *Properties* for more information about the builds and configure how they will be compiled. On the new window in the *Source Files* tab a file can be selected to determine the code that will be run on the FPGA. The tab labeled Xilinx Options offers different ways in which the file can be compiled which include but not limited to optimize power and reduce compilation time. These different options utilize the FPGA in different ways behind the scenes to bias one or more parts of its functionality over others. Some may be much more memory intensive than others. Once the source file and optimization implementation strategy are chosen, then the build button on the bottom of the window can be selected.

A new window will pop up, and there are some initialization procedures that it completes, like starting the compilation engine, which if prompted, the local engine on the computer should be chosen as that is the only one present at this time. It will then do some file conversions. When the progress bar is green and the status of *Synthesizing* is displayed by the bar, the process does not need further user input and can be left to work on its own.

Every build in the *Build Specifications* subfolder should reference a different set of LabVIEW code for its source code. This will make switching between FPGA builds clean and efficient. It will also differentiate builds so that different parameters or functionality will not have to be changed manually every time the user wishes for new/different actions from the FPGA.

3.8 IMPROVEMENTS FOR THE FUTURE

There are many improvements that can be made to the system to increase usability, streamline the software, and make the system more modular for future improvements that are not known yet. The improvements are listed hardware or software changes, with a short explanation why this would improve the system and a basic guideline for how to complete the implementation. They are listed in no particular order within the two groups.

3.8.1 *Hardware*

The RT and FPPA have a shared internal clock and the cameras share another clock. The timing difference of these two clocks should be characterized so that the difference in time of the trigger signal and the zero frame can be determined. When the cameras obtain a trigger signal, the next frame is the zero frame in the image sequence. The FPGA sends the trigger signal to the camera and the time from which the signal is sent out (known on the FPGA) and the time until the next (zero) frame captured is unknown. In our current setup, the assumption is that the trigger signal and the zero frame occur simultaneously, not accounting for this delay. The time bases of both systems should be synchronized, or run off of the same time base so that the difference in time can be more accurately determined.

A voltage source could be used to power the signal for IR gate 3. This is a constant voltage that can be transferred to another piece of hardware to free up another AO channel that could be used for controlling anther component. The voltage source would be plugged into an outlet, and the circuit would be split three ways to go to the hot and ground of each of the IR gates.

A smaller breadboard can be used to contain all of the circuits, and the wires could be soldered in. Strain relief is also necessary so that no wires are pulled out accidentally. The unit

could be contained in a box with a set of screw connectors on the outside that attach to the circuits inside.

Two biaxial strain gages can be used to detect strain with the signal of all four gages added together. One biaxial gage could be located near heel strike and the other could be placed near where toe off occurs. One of the gages would be more sensitive to the rising and the other to the falling edge of the strain. Some testing would have to be completed to determine if the noise became too great with four signals added together. This would be worth experimenting with since the amount of strain sensed by the gage is proportional to how close it is to the load application. The bridge completion module would be set up in the same way that it currently is except with two biaxial gages instead of one. The signals would need to be added together on the software side. the strain gages themselves need to have long foil leads so that any soldering (to a lead wire or connector) would be out of the field of view, since copper and solder are almost radiopaque.

The placement of the gages could also be optimized by orienting the gages with the principal strain and placed in areas of higher strain. The gages do not appear on the fluoroscope images, so if a set of gages that had leads long enough leads could be purchased, they could be mounted inside the field of view, under the contact area. The leads would have to be long enough to reach outside the field of view because any soldering or wires in the field of view shows up on the images.

The computer RAM and hard drive space on the computer can be increased. This would allow for faster run times, and to store more data on the computer. Now there is a constant worry about having enough room to store the video image data.

Multiple emergency stops and better buttons to press. Currently there is one toggle switch used to physically interrupt the fluoroscope fire signal from the RT chassis to the fluoroscope. The

toggle switch should be changed to a push button, that latches in each state, with the depressed mode being the off state, like most emergency stop buttons. Two other buttons of the same type should also be on the same circuit and placed at the start and end of the walkway. This would allow the subject to stop the fluoroscope from firing if needed. All three buttons should be on the same circuit, so if any of the three were pressed, the fluoroscopes would not fire.

3.8.2 *Software*

In initialization of the UIMain.vi, link the scan frequency here to the scan frequency used in in "FPGA Controls" so these do not have to be changed independently.

In the two camera loops other cases could be added to change the camera settings and parameters using the Phantom VIs. This would allow only one software program to be used during data capture. Other parts like saving image data could also be added, and through chaining cases together could automate some steps. The basics of camera control are already laid out on the UIMain.vi, loops five and six. The Phantom VIs are fairly self-explanatory and have help files to go with them.

All of the major loops listed can be made into subVIs like the RT communications loop. This would clean up the block diagrams. Block diagrams are supposed to all fit on one screen, and this would help collapse the programming. This was not completed as there were many changes occurring on multiple loops at once, and every sub VI would need a new window. That would've decrease the troubleshooting ability since so many windows (>12) would be opened at once. Now the code is fairly static this may increase the ability for new users to understand the code.

The dynamic data capture should time out and go back to safe mode after the 10 seconds maximum capture duration has passed. This would be completed through ending the data capture

on the FPGA in the dynamic case similar to how it ends in the static case. An “or” would have to be used to add another condition to stop the inner while loop. That may also stop the RT, but other measures may need to be taken to get the RT back into safe mode. A timeout may have to be completed here too, where if the loop time is greater than “x” a variable goes to true which then in turn goes to an “or” and then the stop command. These two stops would then have to back populate the UI Main front panel. The front panel controls are originally meant to only control, not have their state set by the RT or FPGA. The logic to do this is not clear at this point in time but could be completed.

There could be another type of indicator to show that a file has been saved. Currently if a file does not save there may not be an error, so the user cannot assume the save was successful due to no error showing. This could be as simple as if the save occurred a true constant is created which then illuminates a light on the front panel. The light can then be changed to false when the “Execute Current Mode” button is pressed, resetting it for the next data capture.

There could be another state for static and dynamic motion capture that the user can manually input the parameters on the front panel in the “FPGA Controls” variable instead of stopping the VI and going into the block diagram to do so. This could be accomplished by creating another case in the state case of the UI command loop to include these variables. The new cases would have to contain controls instead of the constants that are currently used. A sub VI could be created with the same format as the type definition that is currently utilized, and the VI would stand in for the constants in each case. The inputs to the VI would all be constants for states with predetermined settings. For the ones the user should be able to control on the fly, the constants should be controls. The VI then packages these into the form of the type definition to pass to the execute mode state. This would still have the “FPGA Controls” indicator present and would have separate controls that

would be redundant to the information displayed by the indicator. Currently there is no known way to be able to have the type definition indicator change to accommodate controls inside of it, there would always have to be a control with redundant indicator on the front panel.

The save VI could be made more modular by taking an input of headers instead of defining the headers inside the VI. This would make it more flexible and be able to be used for other application.

A watchdog timer could be utilized on the UI, RT and FPGA. This addition to the LabVIEW code would add an extra loop to each system that would make sure all systems are running and communicating as they should. It would also help with error detection and management. The user would have to start with the LabVIEW examples in the help section to set it up properly.

The error streams could be improved by linking and merging error of all of the VIs and subVIs. Now there are just enough errors to tell when major problems occur, and is not always readily accessible to the user. The error nodes should just be connected between VIs, and more error indicators on the front panel would be needed.

Vertical lines on the strain graph should be created after every data capture to mark events such as the fluoroscope turning on and off, and when IR gates are tripped. An index of these events is already found in the lossless data processing loop. The data just needs to be added to the strain graph. The easiest way would be to create two data points, one at the index and the index after the event. Then fake data should be created so it would appear as a vertical line on the graph. This should then be inputted into an append to array VI, and then all the signals can be displayed on the graph.

The DMA FIFO sizes could be optimized for better performance. As of now most of the numbers were chosen so that the buffer read and write were the same size. It was not optimized to have a particular wait duration or read duration. The RT could wait 400 ms instead of 200 and that may be more efficient, but no tests were completed.

The “reset emergency stop” button should also send a message to read all of the data from the FPGA and RT FIFO buffers. This would remove the necessity to complete a static trial to remove all data from the buffers after the last trial was aborted due to the emergency stop button. If the data are not read and removed from the buffers, it is at the beginning of the next trial which could potentially misalign the data in time.

The UIMain.vi should allow for the fluoroscopes to fire in either the high or low mode for each data collection type. A toggle control could be created on the front panel which would then be inserted into the “FGPA Controls” variable to be sent to the FPGA to control the firing mode. This would best be completed in the UI Command loop, in either the “state” or “execute current mode” case. On the FPGA, a case structure could then be used to send the fluoroscope fire signal to the proper analogue output channel (a write to channel VI in each case). One analogue output channel could be used for the fluoroscope high radiation fire signal, and another for the low radiation fire signal as these are two separate circuits going into the fluoroscopes.

An average strain could be used instead of a single data point to more accurately determine the baseline strain. The baseline strain could also be implemented on the lossless data to negate the offset that currently exists.

3.9 BIPLANE CONTROL APPENDIX

3.9.1 *Adding a New Channel to the Data Capture*

Additional channels may need to be created in the future to acquire additional data or send additional signals to the RT or FPGA. The steps to complete this will be listed by whether it is a control (user specified) or an indicator (data collected), and by the component.

3.9.1.1 FPGA Indicator

1. Complete 3x, once in each case Static Capture, Dynamic Capture true, and Dynamic Capture false. Add new channel to the *Read* block, add channel to *Append Array* block and wire appropriately. This will ensure the data are passed to the RT.
2. Change type definition of *FPGA Indicators.vi* by the *Bundle Indicators* block, this sends indicator information to a bundled variable for the UI to read. A new indicator can be created on the front panel so that this indicator can be read by the Lossy Data Loop on the *UIMain.vi*. The new variable will then have to be wired appropriately to the new indicator or control.

3.9.1.2 RT Indicator

In the Data Acquisition Loop two constants have to be changed. The initialization array length should be recalculated, # channels x 2 (reads per second) x 10000 (length of max trial in milliseconds). The number of channels should also be increased to the appropriate amount.

3.9.1.3 UI Indicator

1. In the Lossless Data Loop the *Decimate Array* block should be expanded to include the additional channel, along with the *Append Array* block going to the *Save Data* graph, along with the *Display Data* graph depending on whether or not the data should be saved and/or displayed. Appropriate wires should be connected to ensure data flow.

2. The number of data channels on the left of the loop in the data trimming code should also be changed to reflect the new number of channels.

3. If an indicator is desired on the front panel and a corresponding indicator was created on the front panel of the *FPGAMain.vi*, then the *FPGA Read/Write* should be expanded and the new variable added. The appropriate indicator should then be created with the proper logic in this loop.

4. The block diagram to the *Biplane Save VI* should be changed to include the header for the new data. A similar format to the other channels should be created, and should be used as a template.

3.9.1.4 FPGA Control

1. Change the type definition of *FPGA Controls.vi* which is located outside the loop on the left for initialization, and on the right side of the loop in the state determination logic.

2. Unbundle the new control on the left side of the loop after the shift register and wire the new control appropriately.

3.9.1.5 RT Control

Nothing has to be completed on the RT for a control as the control variables are just transferred through the RT.

3.9.1.6 UI Control

The type definition for the *FPGAControlsUI.vi* should be updated to reflect the new control added. This populates throughout the UI Control Loop as constants and values have to be entered for each state.

3.9.2 *Common Issues and Their Solutions.*

These errors came up when the software was being created for the first time, and the solutions used in these particular instances are presented.

Will not connect - Restart LabVIEW and try again, if network stream between RT and UI is closed (EXIT command used), it will not reopen until LabVIEW is restarted - check if ethernet cable is connected to the RT and computer, check if RT power is plugged in, check if network hub has power.

Error -1950679034 - No good value for shared variable - to fix this the shared variable has to be initialized properly. Right click on the variable in the project window and select "deploy variable", as it may not be deployed on the RT system. Sometimes the variables do not automatically deploy. If that does not work, go to the project window, drag and drop the shared variable from the project window to the block diagram and rewire the new one to the old wires. The old one may not be in the library, or LabVIEW cannot find it, and delete the old variable from the block diagram. The string in the "connect to RT" VI could also have a typo, in the variable name, or in its path. The path should correspond to the folder structure in the project window.

One good resource is the "interleaving DMA" VI found in the examples section of the help menu.

3.9.3 *Circuit Design*

The diagram for this particular problem is given in Figure 3.19.

V_b = Voltage input to base

V_c = Voltage input to collector

V_e = Voltage output (ground, for easiest calculations)

$V_{control}$ = User defined voltage output by the NI system, user defined and given for the example

$V_{hardware}$ = Hardware defined voltage from the signal hot lead (fluoroscope or camera)

i_b = Current into base

i_c = Current into collector

i_e = Current output

R_1 = Resistor on wire to base, when calculated, may want to use a value that is less than calculated value, as the transistor adds to the overall resistance. The calculated value is the maximum possible circuit resistance that should be used.

R_2 = Resistor on wire to collector

$V_{be(sat)}$ = Voltage from base to emitter w/ saturated transistor

$V_{ce(sat)}$ = Voltage from collector to emitter w/ saturated transistor

h_{fe} = DC current gain

minimum i_c = minimum current needed for the hardware (fluoroscope or camera) to sense an edge. This was found by completing the circuit from hot to ground of the signal wires with a large resistor (>50K**Ω**) incrementally using smaller resistors. This is an assumed constant for the example.

Explanation of steps:

1. The resistor (R_1) and transistor load the circuit in series (additive resistance). The resistance of the transistor is not known but the voltage across it is known from manufacturer specifications. Since V_e equals 0, and V_{ce} is 0.20V, then V_c equals 0.20V. The voltage and current across R1 is known, so the resistor size can be calculated. This will ensure the current is large enough to trigger the hardware. The user may want to decrease the resistor a little more to ensure that the current is large enough to trigger the system.
2. i_b controls the percentage of i_c that goes into the transistor through the proportionality $i_b \, x \, h_{fe} \propto i_c$. If $i_b \, x \, h_{fe} > i_c$, then saturation occurs since i_c cannot become any larger. This step

determines how large i_b should be to put the transistor into saturation. The overdrive factor is used to ensure the transistor is in saturation and is commonly increased to a factor of 10, this example uses 5.

3. R_2 has to be chosen so that the current i_b can be large enough to put the transistor in saturation. In this example another requirement for saturation is not calculated, but is met through the hardware specifications. $V_{control}$ and thus V_b must be sufficiently large so that V_b is greater than V_{be}. If not the voltage bias will not be correct for the transistor to go into saturation. Power through each resistor should also be calculated so that the resistor is not burned out. This has to be less than the rating for the resistor, and resistors in the lab are ⅛ to 3W.

Transistor Circuit Calculations

Manufacturer Specifications

Vbe(sat)	0.85 V
Vce(sat)	0.20 V
hfe	10 ma

Example Hardware Specification

Minimum ic needed	25 ma
Vhardware	5.00 V
Vcontrol	1.00 V

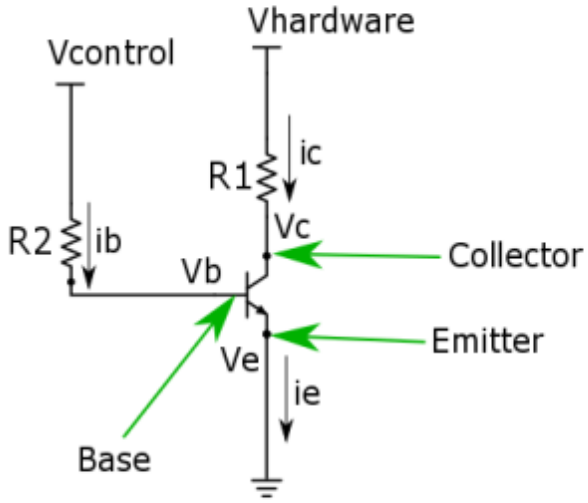

1. Find R1 to so that ic is satisfied
   R1 = (Vc-Vce(sat))/ic = 192Ω
2. Determine the current needed into the base to cause saturation (ib x hfe > ic)
   ib = ic/hfe = 2.5e^-4 2.5e^-4 x 5 = 1.25 ma
3. Determine R2 so that ib is large enough to put the transistor in saturation
   R2 = (Vcontrol-Vbe(sat))/ib = 120Ω

Figure 3.19. An example circuit diagram with corresponding example specifications and steps on how to solve for the resistances needed to put the transistor in saturation.

Chapter 4. HINDFOOT KINEMATICS OF HEALTHY SUBJECTS USING LATERAL WEDGE INSOLES IN A BIPLANE FLUOROSCOPY SYSTEM

4.1 INTRODUCTION

Tibiofemoral osteoarthritis (OA) is one of the most prevalent forms of osteoarthritis in the world. It causes discomfort and stiffness in the knee, and affects 12.5% of the population worldwide [1]. Higher joint pressure has been correlated to increased OA of the knee [6], with repeated high loading theorized to break down articular cartilage over time. OA is a progressive disease with knee arthroplasty being an end stage treatment. Non-invasive treatments are typically pursued to delay the onset of surgery. One non-invasive treatment used to slow the progression and reduce the symptoms of OA is the prescription of lateral wedge insoles (LWIs). LWIs are orthoses with a thicker lateral than medial aspect and are meant to modify the pressure distribution in the knee during stance phase. In particular, LWIs are intended to shift body weight support from the medial compartment towards the lateral compartment, reducing medial knee loading.

Measuring joint pressure directly is not feasible for typical biomechanical studies as it would be a very invasive procedure. The preferred indirect and non-invasive measure for quantifying medial loading of the knee is the external knee adduction moment (EKAM) [2,3]. The EKAM is the product of the ground reaction force (GRF), which runs medial to the knee, and the knee moment arm. LWIs tend to shift the GRF laterally, decreasing the moment arm, and thus the EKAM. The EKAM has been shown to be a reliable surrogate for measuring the load on the medial condyle [2,4] and correlates with the progression of OA as indicated by radiography

[6]. LWIs tend to lower the EKAM in the majority of the subjects tested [61], but some subjects have no change in EKAM, and some even have an increase [8,9].

LWIs are a treatment for the knee that act through the foot and ankle. It is unclear what (potentially deleterious) effect these LWIs may have on foot kinematics. Abnormal hindfoot kinematics may lead to increased loading of the talocrural or subtalar joints which could increase the likelihood for the development of ankle and foot OA. Previous studies have found that LWIs may lead to a more everted hindfoot [8,21,23,33] by lumping the tibia to calcaneus angle into one joint. It is unclear how LWIs may change the kinematics of the talocrural and subtalar joints, as this has not been well studied. Also the lack of benefit seen by some subjects when using LWIs may be related to differences in hindfoot excursion.

Typical motion capture studies utilize systems that track retro-reflective markers placed on the skin. These systems have a number of weaknesses when studying foot bone motion. First, skin motion artifact can occur, which is especially prevalent around joints such as the ankle. Another issue is that bones like the talus have few bony landmarks that can be located to accurately define marker placement. There are many small, closely packed bones, which can make it difficult to place enough markers on each bone to adequately characterize the motion. Additionally, since the markers are placed on the skin and need to be visible to multiple cameras at once to be tracked, unmodified shoes cannot be used. Some studies have used shoes with windows cut out so the markers can be attached on the skin directly [15], but the effect of these modifications on the shoes is unclear.

Biplane fluoroscopy images the bones directly, even through shoes, eliminating the issues with standard optical motion tracking on the foot. This technique has been used to image other joints such as the knee and shoulder. Most studies involving the foot have completed quasi-static

data capture [62–64], while one study has tracked dynamic bones *in vitro* [65] and one study has tracked dynamic bones *in vivo* barefoot and shod [66].

The effectiveness of the LWI intervention for OA may depend on the kinematics of the hindfoot, but traditional optical motion tracking may not be adequate to characterize these hindfoot kinematics while using LWIs in their intended manner, i.e., while wearing shoes. As such, the individual kinematics of the talocrural and subtalar joint with the use of LWIs have not been quantified. Most studies lump these two joints into a single measurement, largely due to poor fidelity of the foot models used. A better understanding of the mechanics of the hindfoot may help to determine why LWIs are effective in reducing the EKAM for some subjects and not others. The purpose of this study is to conduct a pilot study to show the feasibility of biplane fluoroscopy to quantify hindfoot motion in normal subjects while wearing LWIs of various wedge angles.

4.2 METHODS

For this pilot study, three subjects ([mean ± SD], age 51.3 ± 9.2 years, height 1.77 ± 0.12m, weight 81.5 ± 24 kg) with no joint replacements, or lower limb musculoskeletal or neurological problems, were recruited. All subjects provided informed consent according to Department of Veteran Affairs IRB policies before participation.

After consent, each subject completed four walking trials in a 20m hallway to determine their self-selected walking speed in their own shoes. Each insole condition was randomly assigned and placed in a laboratory shoe (New Balance 577) that matched the subject's preferred shoe size. Subjects completed a five to ten minute long accommodation period consisting of

walking down a hallway before each condition was tested. The four insole conditions were: 5 degree laterally wedged, 10 degree laterally wedged, a neutral insole whose thickness is the average of the two wedged insoles, and shod which consisted of the stock insoles from the manufacturer (Figure 4.1). The 5 degree, 10 degree, and neutral insoles were custom-constructed from EVA by a local orthotist, and were sized to match the subject's shoe size.

The subjects were then taken to the biplane fluoroscopy laboratory. The system consists of two BV Pulsera C-arm fluoroscopes (Philips Medical Systems, Best, Netherlands). Each fluoroscope was disarticulated and mounted to a pair of gantries straddling a raised walkway. On one gantry, the X-ray generator was mounted, while on the other gantry the 30cm image intensifier (II) was mounted; a high-speed camera (Phantom V5.2, Vision Research, Wayne NJ) mounted behind each II was used to capture the fluoroscope images. The X-ray generators operated in continuous mode at about 68 kV, and fluoroscope data was captured synchronously at 500 Hz. Previously-published papers describe the accuracy of the system, the calibration protocol to localize the fluoroscopes in laboratory space, and to remove the effects of image distortion [67,68].

Figure 4.1. Insoles used in the study. From left to right: 10 degree LWI, 5 degree LWI, Neutral, manufacturer's insole.

A strain gage (Vishay Precision Group, Wendell, NC) mounted beneath the walkway was used to determine stance phase timing; this gage was sampled by a real-time control system (CompactRIO, National Instruments, Austin TX) that was used to synchronize the cameras and fluoroscope.

One foot was imaged for all dynamic and static trials; this was randomly determined before the start of the study. Subjects were asked to walk through the system at their previously measured comfortable self-selected walking speed for each of the insole conditions. The subjects' third step was imaged due to walkway length constraints. Previous studies [69,70] have shown that subjects can achieve steady state velocity by the second step, so the third step would be representative of steady state gait. The subjects completed enough gait trails for three successful imaged trials per insole condition. Prior to each set of walking trials, a static fluoroscope acquisition was taken of the subject's foot in each condition; additionally, one set of images while the subject was barefoot while barefoot.

In a separate visit, a computed tomography (CT) scan (Discovery CT 750 HD, GE Healthcare, Chicago, IL) was acquired of both of the subject's feet and lower shank (up to mid-tibia). A slice spacing of 0.625 mm and an in-plane resolution of 512x512 pixels (~0.89 mm per pixel) were used. The CT was taken with the subject's foot placed in a custom fixture to load the foot to 20% of body weight in a neutral position to simulate partial weight bearing. The calcaneus, talus, fibula, and tibia were segmented from the CT scans using Mimics (Materialize Inc., Leuven, Belgium), creating a voxelized model of the bones in CT space. The voxel models were then introduced into a virtual representation of the biplane fluoroscope laboratory, based on the known configurations of the X-ray generators and image intensifiers determined through calibration. The pose of the models of the tibia, talus, and calcaneus were then located in laboratory space at each frame by a semi-automated tracking algorithm [71] which matches digitally-reconstructed radiographs (DRRs), or virtual X-ray images, to both fluoroscope images simultaneously. The true pose of the bone in lab space was defined as the pose whereby the pair of DRRs best matched the corresponding pair of fluoroscope images. User input was required for

two consecutive initial positions per bone, and subsequent initial positions for each frame were defined from a linear extrapolation of the previous two positions; a numerical optimizer then determined the true position of the bone. To reduce computational time, each fluoroscope video was decimated to 100Hz for bone tracking.

Bone to bone kinematics were defined by the relative position and orientation of two bone-embedded coordinate systems. Embedded coordinate systems were applied to the talus, calcaneus, and tibia-fibula complex. For the tibia-fibula, the $\overrightarrow{SI}$ axis was directed from the most lateral point on the lateral malleolus to the most superior lateral point on the fibula. A dummy axis $\overrightarrow{D_1}$ was directed from the most lateral point on the lateral malleolus to the most medial point of the medial malleolus. The anterior-posterior axis ($\overrightarrow{AP}$) was defined as $\overrightarrow{SI} \times \overrightarrow{D_1}$ with the origin being the midpoint between the malleoli, and the $\overrightarrow{ML}$ axis was $\overrightarrow{AP} \times \overrightarrow{SI}$. For the talus, the $\overrightarrow{AP}$ axis was directed from the trigonal process of the talar body to the lateral point of the talar head. The $\overrightarrow{SI}$ axis is $\overrightarrow{AP} \times \vec{D}_2$ where $\overrightarrow{D_2}$ is a vector from the trigonal process to the medial point of the talar head. The is $\overrightarrow{ML}$ axis is $\overrightarrow{AP} \times \overrightarrow{SI}$, with the origin of the talus at the centroid of its volume. For the calcaneus, the $\overrightarrow{AP}$ axis is the vector from the most posterior/superior point of the calcaneus to the most superior/anterior point at the calcaneocuboid joint. The $\overrightarrow{SI}$ axis of the calcaneus is $\overrightarrow{AP} \times \overrightarrow{D_3}$ where $\overrightarrow{D_3}$ is a vector from the most posterior/superior point of the calcaneus to the sustentaculum tali. The $\overrightarrow{ML}$ axis is $\overrightarrow{AP} \times \overrightarrow{SI}$.

For each subject, a set of reference joint angles were defined as the angles between the bone embedded coordinate systems in the static data capture for the shod condition. For each insole condition, the reported joint angles were subtracted from these static joint angles. As only 3 specimens have been collected and analyzed, no statistical analysis was performed.

4.3 RESULTS

The average unfiltered hindfoot kinematics of all subjects were calculated as the talus relative to the tibia (ankle joint), calcaneus relative to the talus (subtalar joint) and the calcaneus relative to the tibia for the duration of stance phase captured (Figure 4.2 to Figure 4.10). All three bones were in the field of view for approximately 5% to 75% of stance phase. For all conditions the talus relative to the tibia tended to become more dorsiflexed (Figure 4.2) and inverted as stance phase progressed (Figure 4.3). There was no apparent trend for the ankle joint in the transverse plane. Relative to the talus, the calcaneus had no consistent trends for motion in the sagittal or transverse planes, but did evert throughout stance phase. The calcaneus relative to the tibia tended to become more dorsiflexed (Figure 4.8) and inverted (Figure 4.9) as stance phase progressed, with no trend in motion in the transverse plane. For the limited number of specimens tested, there were no strong trends between any of the conditions.

The average kinematic curves of each condition for each of the three subjects, in the sagittal, frontal and transverse planes for each bone to bone pair were calculated (Figure 6.5 to Figure 6.31). The neutral condition of the calcaneus relative to the tibia in the sagittal plane for subject 3 may be more plantar flexed through the duration of stance phase. Also the shod condition with the calcaneus relative to tibia in the frontal plane tends to be more inverted through stance phase. These were the only two notable differences between the insole conditions in the measured kinematics.

All three subjects tended to dorsiflex as stance phase progressed for the talus relative to the tibia. In the frontal plane of the talus relative to the tibia, subjects 1 and 3 had a more inverted talus as stance phase progressed, while there was no trend in motion from subject 2. Subjects 1

and 2 tended to have a talus that externally rotated as stance phase progressed, and subject three did not have a trend in motion.

The sagittal plane motion of the calcaneus relative to the talus trended differently for all three subjects, with subject 1 becoming more plantar flexed, subject 2 with no trend and subject 3 becoming more dorsiflexed as stance phase progressed. The three subjects' kinematics also trended differently in the frontal plane, with subject 1 becoming more inverted, subject 2 with no trend and subject 3 becoming more everted as stance phase progressed. There was no trend in motion for all three subjects in the transverse plane.

Subjects 1 and 2 had a calcaneus relative to the tibia that became more dorsiflexed as stance phase progressed, while subject 3 had a calcaneus that became more dorsiflexed, then more plantar flexed as stance phase progressed. Subjects 1 and 2 had a more everted calcaneus relative to the tibia as stance phase progressed, and there was no trend for subject 3. Subjects 1 and 3 had no trend in the transverse plane, while the calcaneus relative to the tibia for subject 2 became more externally rotated as stance phase progressed.

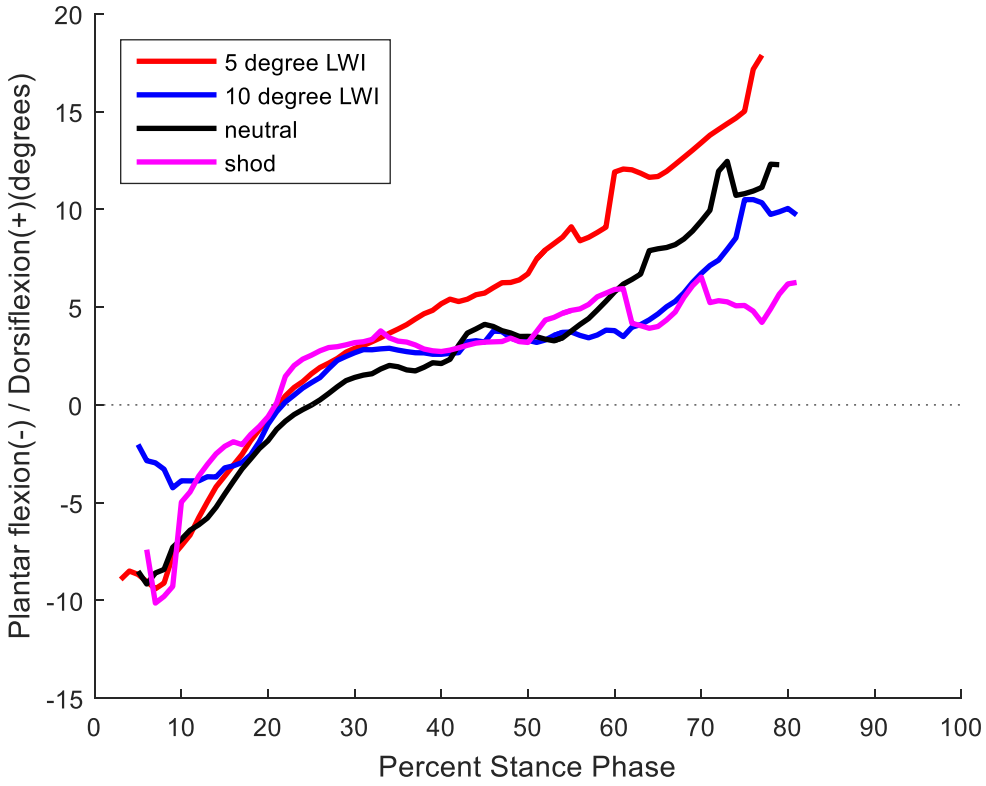

Figure 4.2. Average sagittal plane kinematics for the talus relative to the tibia.

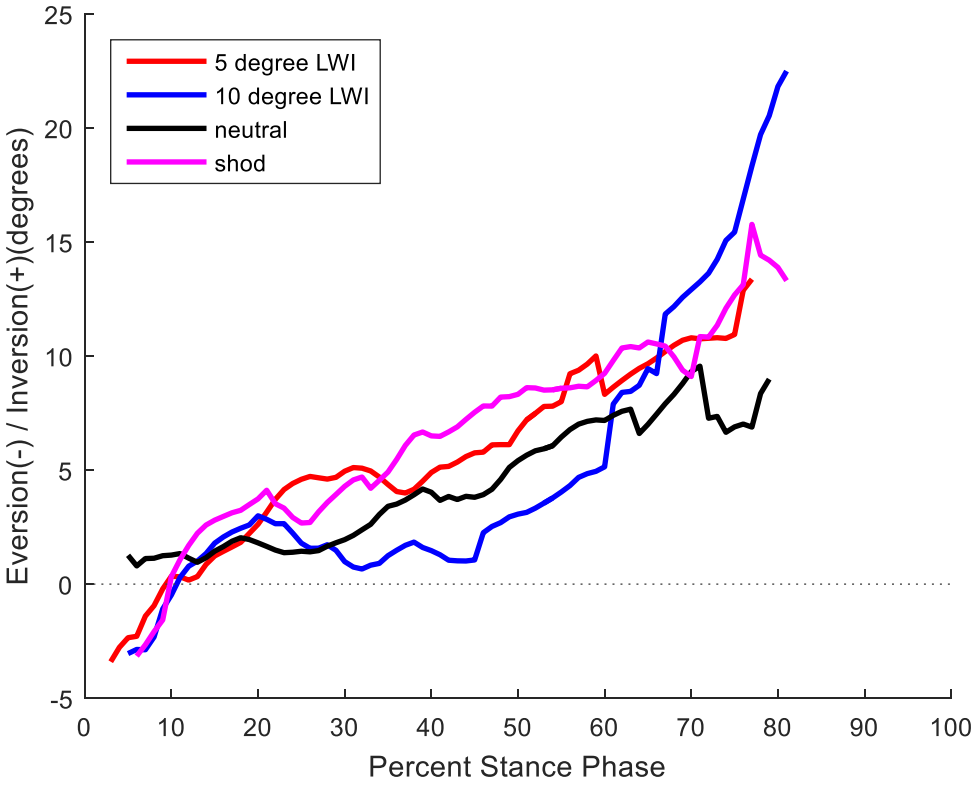

Figure 4.3. Average frontal plane kinematics for the talus relative to the tibia.

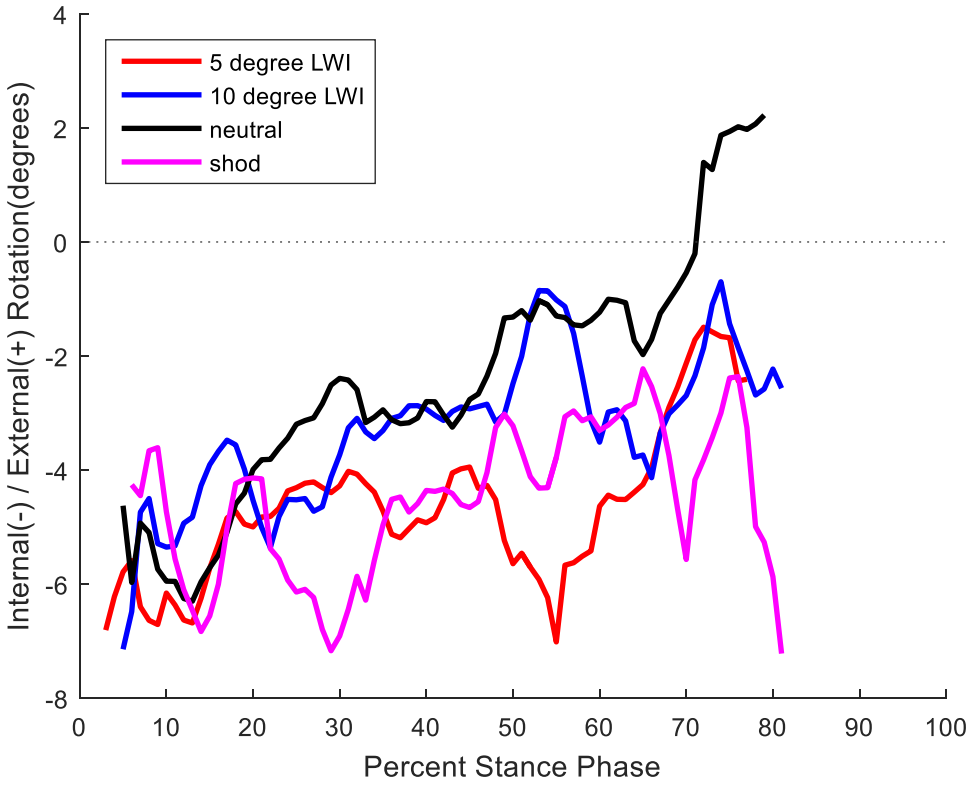

Figure 4.4. Average transverse plane kinematics for the talus relative to the tibia.

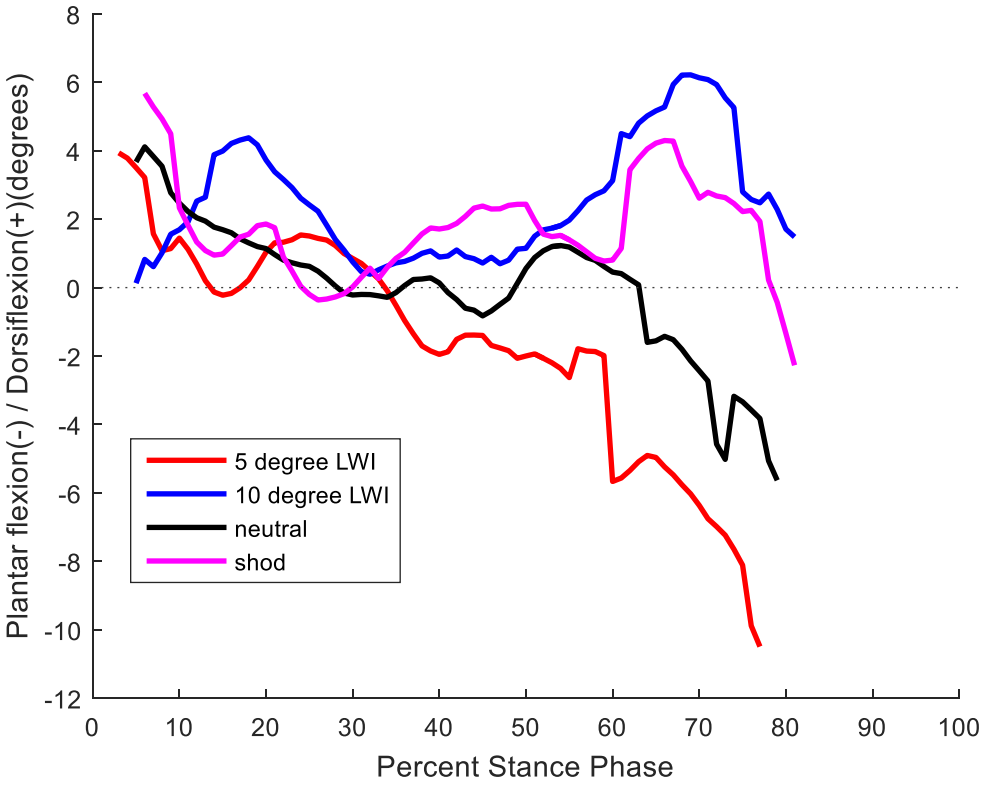

Figure 4.5. Average sagittal plane kinematics for the calcaneus relative to the talus.

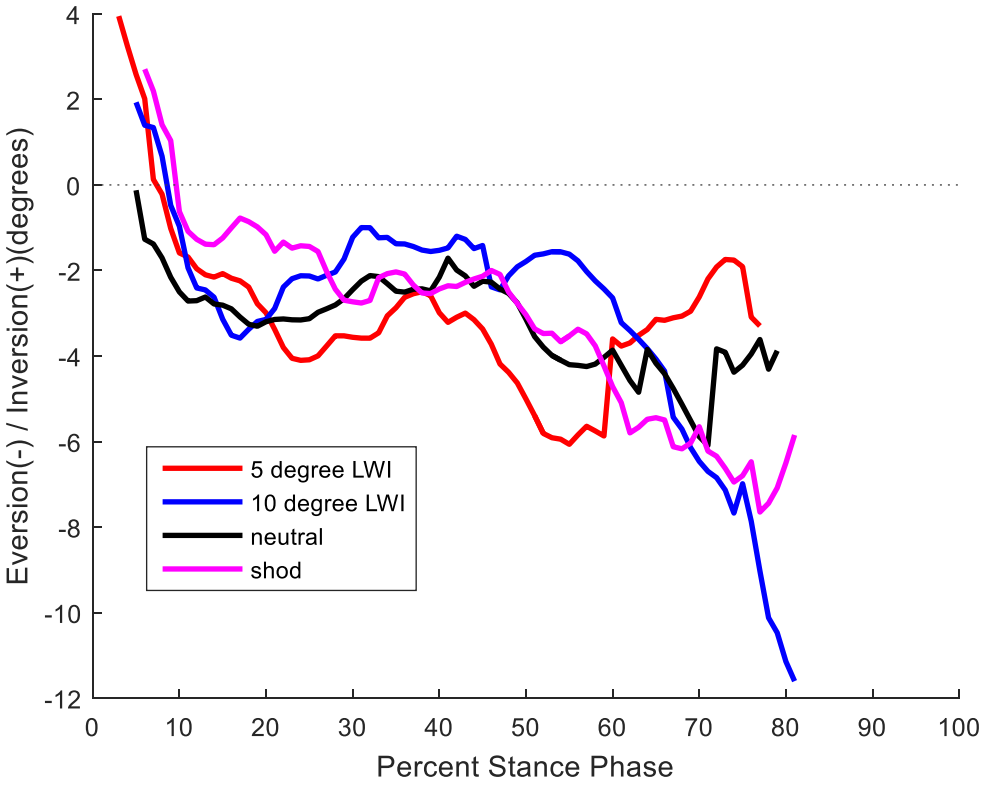

Figure 4.6. Average frontal plane kinematics for the calcaneus relative to the talus.

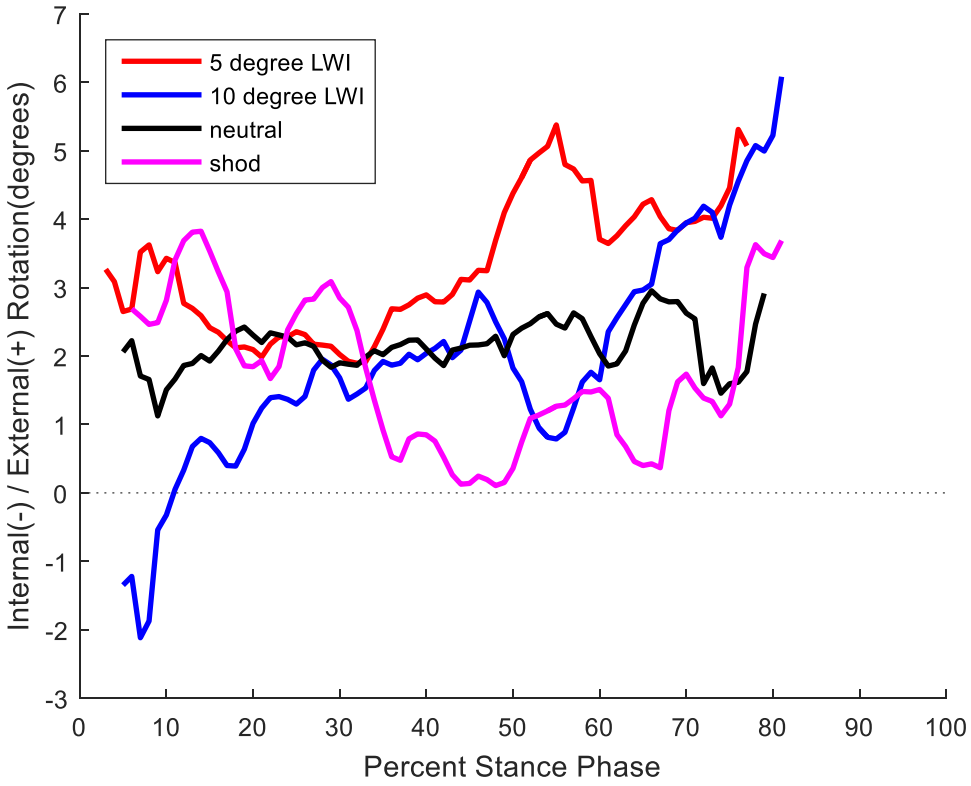

Figure 4.7. Average transverse plane kinematics for the calcaneus relative to the talus.

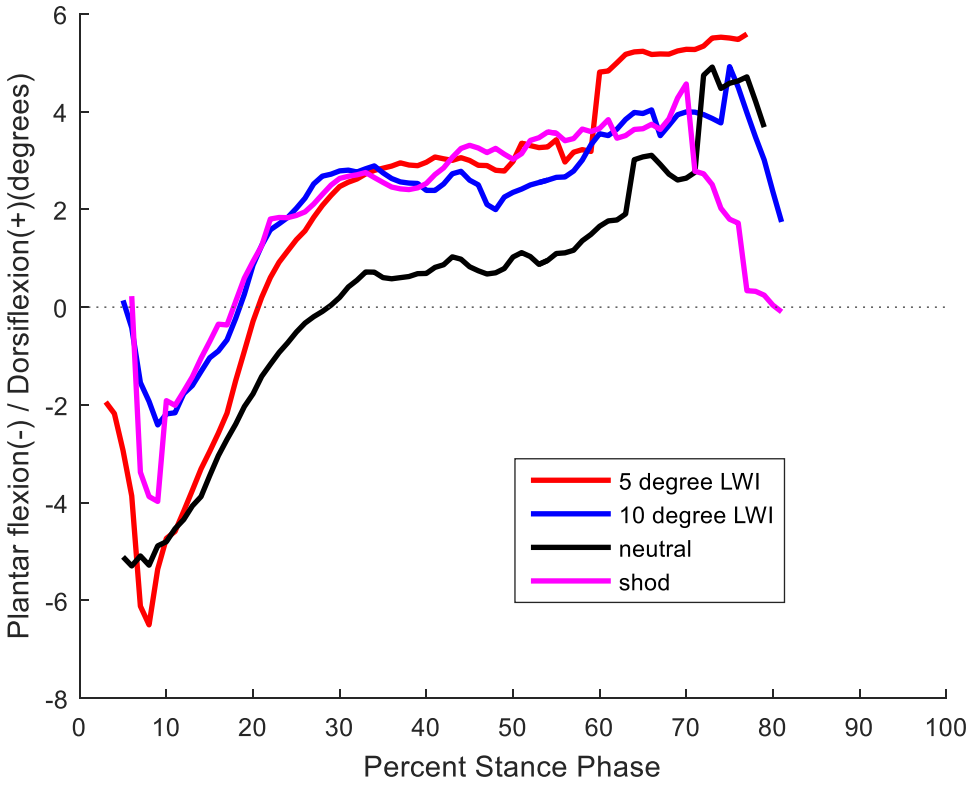

Figure 4.8. Average sagittal plane kinematics for the calcaneus relative to the tibia.

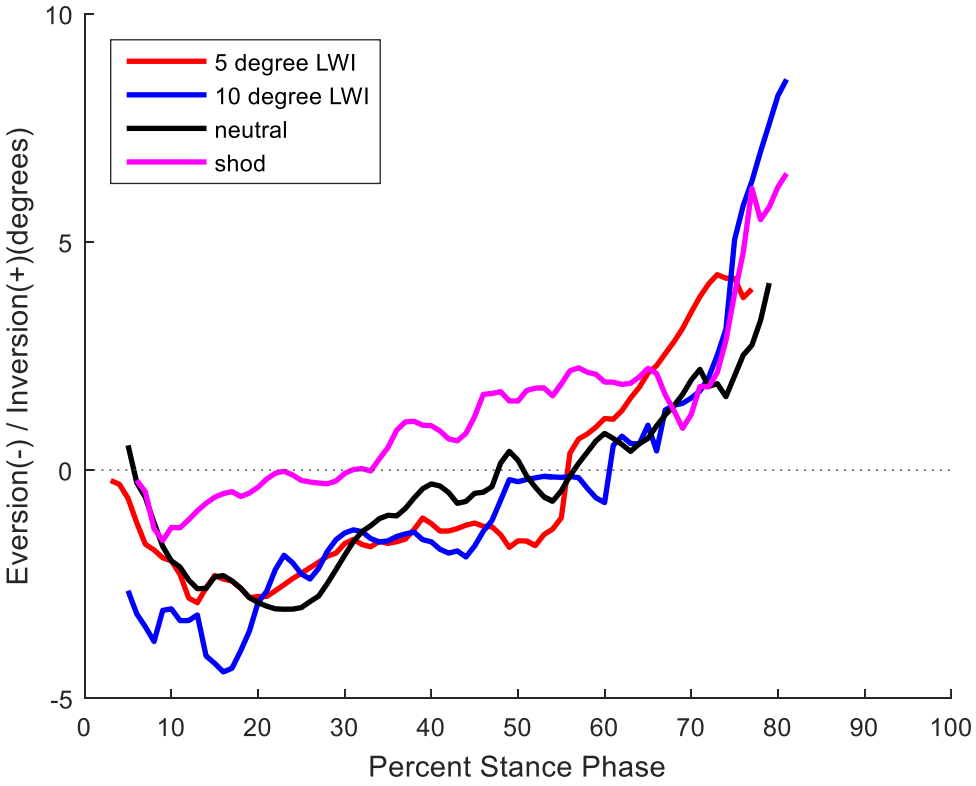

Figure 4.9. Average frontal plane kinematics for the calcaneus relative to the tibia.

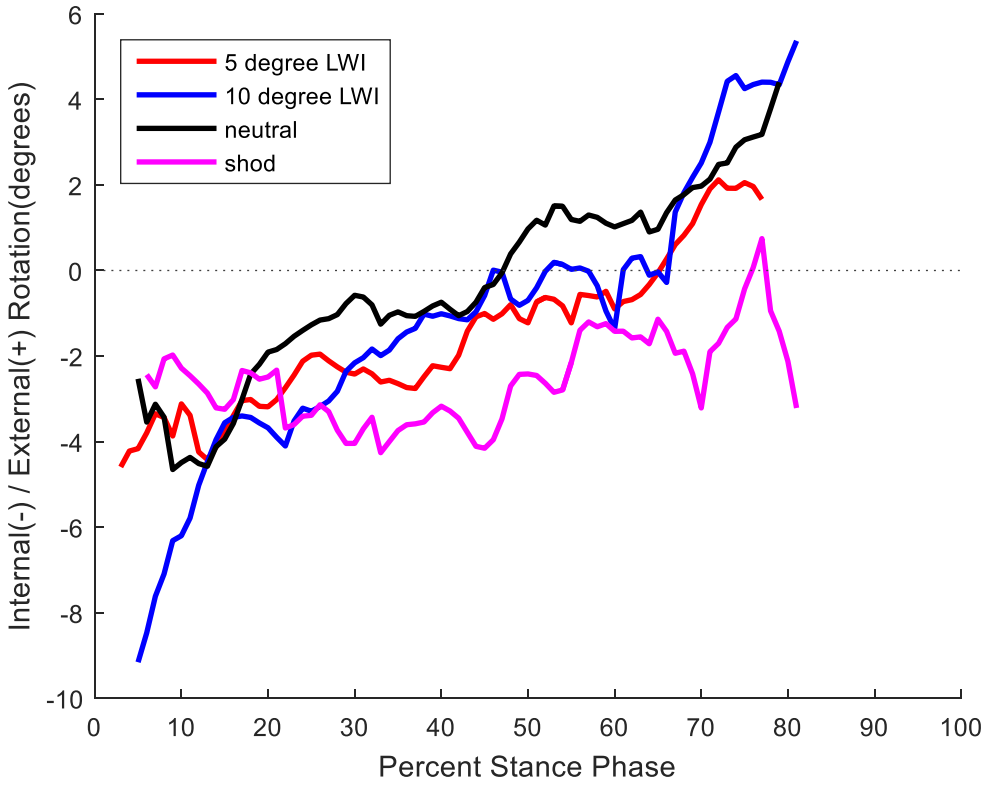

Figure 4.10. Average transverse plane kinematics for the calcaneus relative to the tibia.

4.4 DISCUSSION

The purpose of this pilot study was to obtain and analyze hindfoot kinematics of healthy subjects using LWIs in our biplane fluoroscopy system. LWIs are used as a non-invasive treatment to slow the progression of medial knee OA, but their effects on hindfoot kinematics is less well-understood. Abnormal motion of the hindfoot may change the loading pattern onto the ankle, which could lead to harmful effects such as ankle OA. While hindfoot motion using LWIs has been studied to a limited extent with optical motion capture, there are several inherent limitations (skin motion artifact, inability to instrument each bone of interest, and required shoe modification) to that method. This study demonstrated a methodology for data collection and analysis which can be extended to a larger sample size in order to determine the changes in hindfoot kinematics of healthy or OA subjects using biplane fluoroscopy.

A qualitative analysis of the three subjects' kinematic curves in the sagittal, frontal and transverse planes was completed for the talus relative to the tibia, calcaneus relative to the talus and calcaneus relative to the tibia. Some bone to bone pairs had similar kinematics trends such as the calcaneus relative to the talus in the transverse plane with no trend toward internal or external rotation for each subject (Figure 4.11), or the talus relative to the tibia in the sagittal plane, with all subjects becoming more dorsiflexed as stance phase progressed (Figure 4.12).

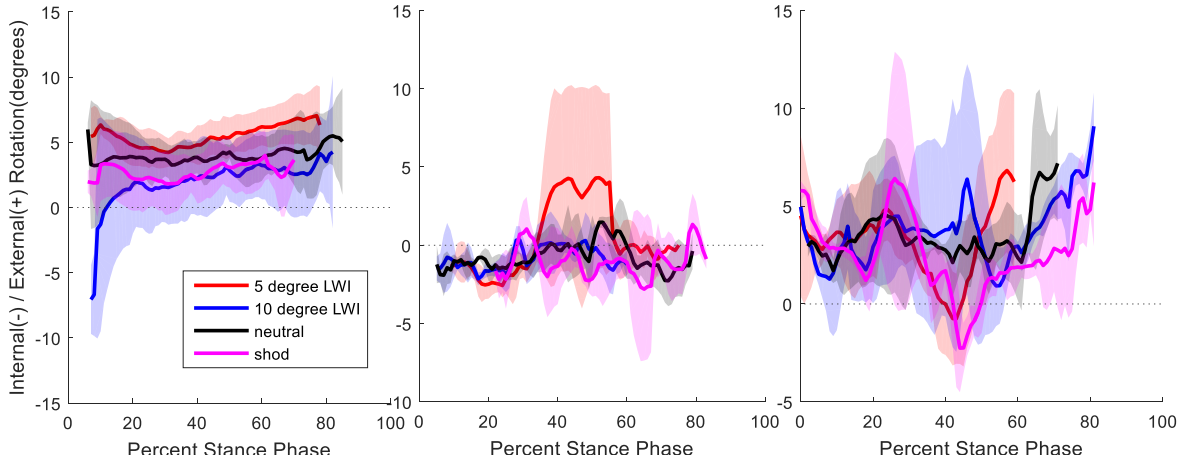

Figure 4.11. The calcaneus relative to the talus in the transverse plane for each three subjects with standard deviation shown as the shaded region for each curve.

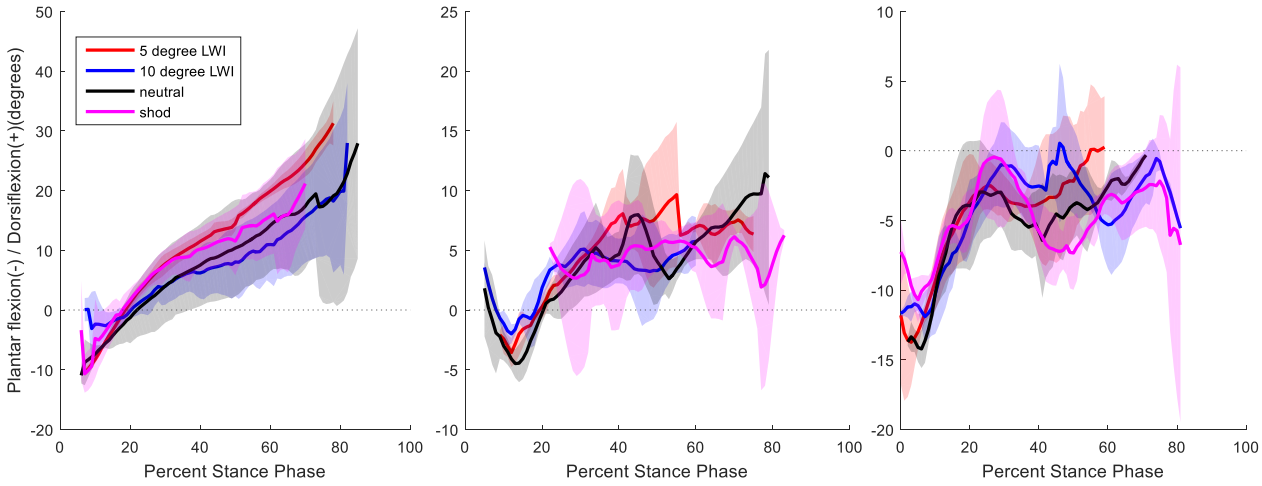

Figure 4.12. The talus relative to the tibia in the sagittal plane for each of the three subjects with the standard deviation shown as the shaded region for each curve.

Some bone to bone pairs trended differently for all three subjects. Sagittal plane motion of the calcaneus relative to the talus in one subject became more dorsiflexed, another became more plantar flexed, and the last subject did not trend in either direction (Figure 4.13). The

frontal plane motion of the calcaneus relative to the talus was also similar in that all subjects had a different trend in motion (Figure 4.14), one everting, one inverting and one not trending in either direction. If all of the subjects' general motion trends in different directions as stance phases progressed, the average trajectory of all the subjects may not accurately represent any of the individual subject's motion. The average trajectory would have no trend in dorsiflexion or plantar flexion with two of the subjects trending in opposite directions. The lack of a trend seen for overall motion in each of the three planes for all bone pairs may be due to this averaging out of motion. This may limit the ability to characterize the trend of a particular joint across this small population and may explain why there were no trends in motion for the majority of the bone to bone pairs in all three planes.

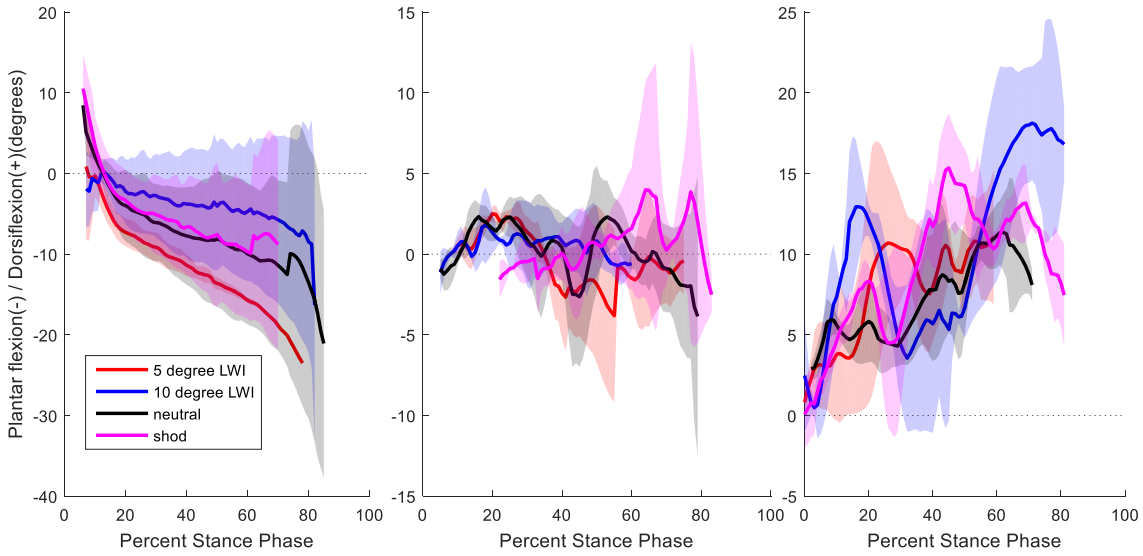

Figure 4.13. The calcaneus relative to the talus in the sagittal plane for all three subjects with the standard deviation shown as the shaded region for each curve.

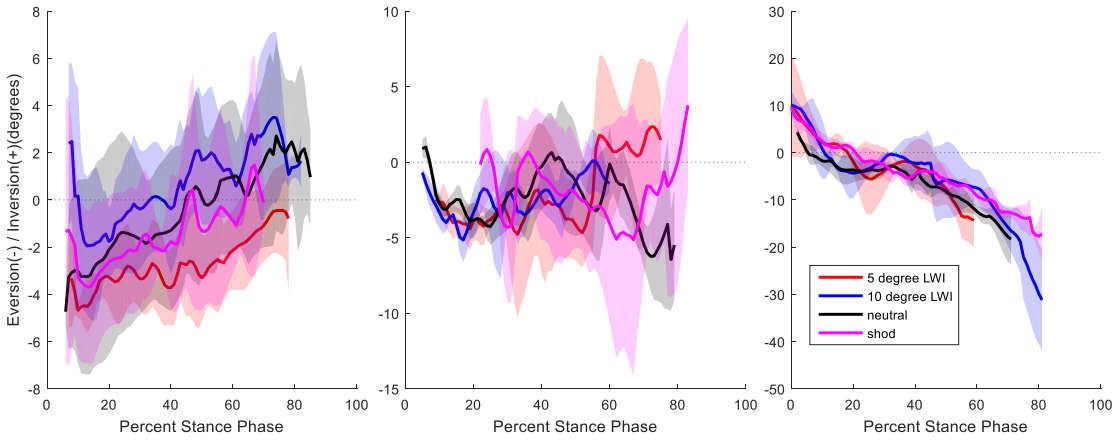

Figure 4.14. The calcaneus relative to the talus in the frontal plane for all three subjects with the standard deviation shown as the shaded region for each curve.

The neutral insole curve of subject 3 in the sagittal plane of the calcaneus relative to the tibia appeared more plantar flexed for all of stance phase (Figure 4.15). The apparent difference from this one subject shifted the average curve of the neutral insole condition of all the subjects to be more plantar flexed (Figure 4.8). A similar shift in trajectory appeared in the calcaneus relative to the tibia in the frontal plane for the shod condition, where it appeared to be more inverted than the three other insole conditions through stance phase (Figure 4.16). This shifted the average shod curve of all subjects to appear more inverted over all of stance phase (Figure 4.9). The other two subjects did not have this shift toward inversion, and the average curve may not represent all of the subjects accurately.

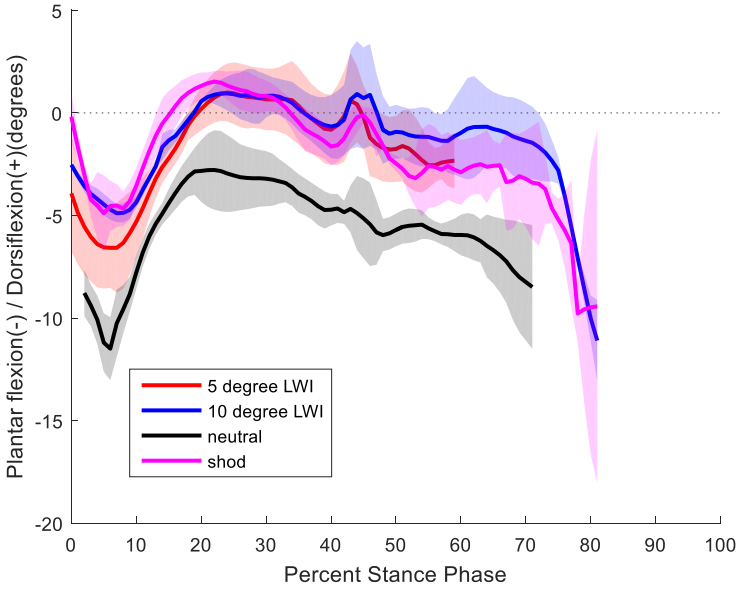

Figure 4.15. The calcaneus relative to the tibia in the sagittal plane for subject 3 with the standard deviation shown as the shaded region for each condition.

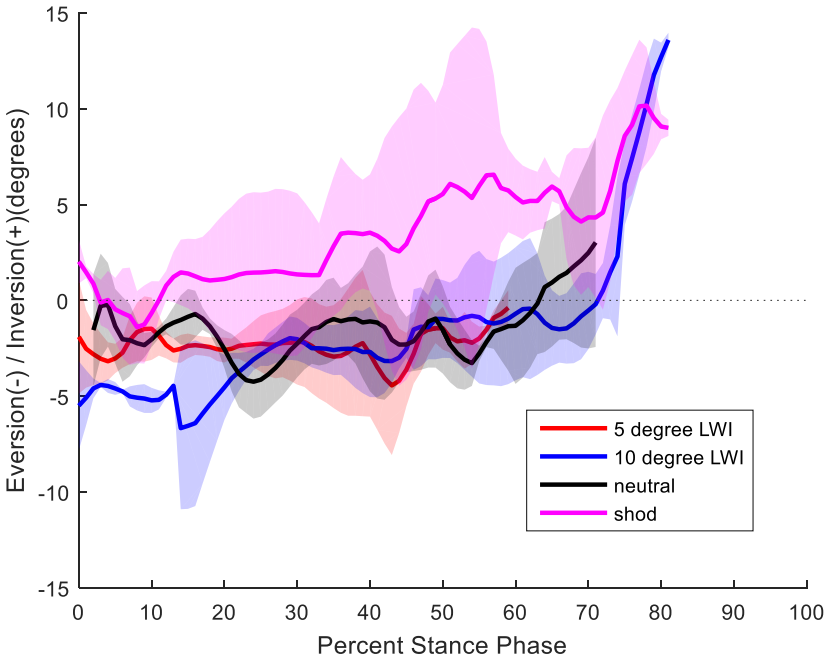

Figure 4.16. The calcaneus relative to the tibia in the frontal plane for subject 3 with the standard deviation shown as the shaded region for each condition.

Due to the small number of subjects in the current study no statistical analyses were conducted, and apparent trends between conditions could not be distinguished. The overall trends of the motion can be noted for some of the bone pairs. It is possible that a larger sample size could reduce inter-subject variability and better elucidate significant findings. Further, the pressure distribution and center-of-pressure between the plantar surface of the foot and the insoles may vary between the various wedge conditions; this could provide additional insight into abnormal loading of the ankle during LWI wear.

Most biplane fluoroscopy studies have measured hindfoot kinematics in various static or quasi-static gait poses [62–64]. One of these studies determined the range of motion of five subjects who posed at heelstrike, midstance and toe off [62]. The previously reported range of motion from heelstrike to midstance is for the three bone pairs is similar to that found in the present study. One limitation to this comparison is that our data does not start at heelstrike, but slightly after (~4% stance phase). The calcaneus relative to the tibia has a similar kinematic trajectory in the sagittal and frontal planes to one study that compared barefoot to shod walking [66]. In both studies, the calcaneus tends to move toward dorsiflexion and inversion as stance phase progresses. Another study decomposed the motion of the tibia, talus, and calcaneus into the ankle joint, subtalar joint, and the tibia to calcaneus [72]. The talus relative to the tibia, and calcaneus relative to the tibia dorsiflexed over time, which is similar to the present study. The relative angles between the calcaneus to tibia are much larger (offset from zero) than in the current study, probably due to the difference in defining the zero position of each joint. They also collected trials to include heelstrike and toe off to compute the range of motion of the selected joints. Our data collection did not capture the hindfoot at toeoff, since the first half of stance phase is where LWIs tend to offer the most benefit in reducing EKAM.

In the previous studies of LWIs, optical motion capture was used to measure the kinematics of the foot and ankle. Even though the imaging modality was different, the frontal plane kinematics of the calcaneus relative to the tibia in our study follow a similar trend of the calcaneus becoming more inverted through stance phase to that shown by Kakihana et al. [7,13,18]. Butler et al. [33] noted a significant difference in hindfoot angle between walking using an LWI and shod, and had a similar trajectory with increasing hindfoot inversion as stance phase progressed.. However, these studies lumped the tibiotalar and subtalar joints into a single hindfoot joint, which does not describe the actual bi-articular motion of the whole hindfoot.

There were several potential limitations to this study. The capture volume for the biplane fluoroscopy system was not large enough to capture the very beginning and end of stance phase; as the entire foot cannot fit inside the capture volume at once. Accordingly, the tibia would dorsiflex into view after heelstrike, and would lift out view prior to toe off. By design, the subjects did not target the center of the field of view, so their positioning may not have been ideal to capture the extremes of stance phase, as a small shift in the anterior/posterior or medial/lateral directions could shift the tibia out of the field of view. Another complication is that, due to the arrangement of the X-ray generator and II on opposite sides of the subject, there was necessarily one set of fluoroscope images in which the contralateral leg swung through the field of view (at around 55% of stance phase). This could worsen the tracking accuracy during this short period, potentially increasing the variability of the joint angles in the midstance phase. The accommodation period was around five to ten minutes. This may not be long enough for the subjects to change their walking pattern to adjust to the insoles. Another potential improvement would be to utilize template matching as an alternative to locating the bony landmarks when

defining the bone-embedded coordinate systems. In the present study, the landmarks were manually chosen by the user—a subjective method which can lead to errors.

The present pilot study demonstrated the feasibility to collect and analyze biplane fluoroscopy data of subjects using lateral wedge insoles. No apparent trends between conditions were found due to the small subject population. The current study had trends of calcaneal dorsiflexion, and inversion as stance phase progressed which was similar to previous studies. These trends may become more apparent with an increased subject population. There are a few improvements to the protocol that should be considered to reduce inter-subject variability in the data analysis. The current protocol can be extended to include more subjects to complete a full study with statistical analysis.

Chapter 5. CONCLUSIONS

The purpose of this thesis was threefold: first, to understand the biomechanical effects of LWIs and specifically motivate the use of biplane fluoroscopy to study hindfoot kinematics with LWIs; second, to upgrade the biplane fluoroscopy system to measure stance phase timing and implement additional features to improve data quality and subject safety; and lastly, to conduct a pilot study using lateral wedge insoles in the biplane fluoroscopy system to show the feasibility of the protocol and data analysis.

The LWI review exhaustively compared over forty LWI studies comparing kinetics and kinematics. In general, LWIs tend to decrease EKAM and increase hindfoot moment, and should have at least four degrees of wedging to significantly decrease the EKAM. About 20% of the population does not exhibit have a reduced EKAM; this may be due to the interaction of the foot and ankle. Quantifying the motion of the ankle and hindfoot while wearing LWIs is difficult using motion capture, but biplane fluoroscopy may provide more accurate measurement of these kinematics.

In order to compare the results from the biplane fluoroscopy system to other results in the literature, it was necessary to express kinematics in terms of stance phase. Accordingly, the biplane fluoroscopy system was upgraded to include a determination of stance phase through a strain gage attached to the walkway. The system can accurately determine heelstrike and toe off within one millisecond, or within one image frame at the highest frame rate our camera supports at full resolution. Additional safety features have also been implemented so that the fluoroscopes only fire when needed. The system is also more extensible, providing the ability to add additional input and output signals and by supporting more sophisticated control logic.

The biplane fluoroscopy experimental study showed the feasibility of the protocol and data analysis for collecting biplane data of subjects using lateral wedge insoles. Hindfoot kinematics including the tibia, talus and calcaneus were measured for the majority of stance phase. Kinematics trends of the calcaneus dorsiflexing and inverting as stance phase progressed could be seen in two of the three bone to bone pairs. Although the trends from the pilot group of three subjects were less clear, collecting data on additional subjects would allow for statistical tests to be completed, which may yield significance in some of the kinematics. While there are some improvements that could be made to the data collection process, this study demonstrates that the protocol is feasible to handle a larger study.

Chapter 6. APPENDICES

This section contains three appendices: 1) a software tool to help determine and check the positions of the two fluoroscope systems of the biplane fluoroscopy lab, 2) a literature review of other biplane fluoroscopy systems that have been validated and used for research purposes and 3) the risk of bias assessment results and questions.

6.1 VIRTUAL BIPLANE LABORATORY

The goal of the virtual biplane fluoroscopy laboratory (VBP) is to recreate the biplane fluoroscopy laboratory (BP) in a virtual environment in order to help determine suitable positions for the X-ray emitters and image intensifiers (IIs) to best image the bones of the foot. Emitter and II placement determine the views of the foot bones captured as they move through the field of view. The emitter and II should be positioned so that the bones of interest have the least amount of overlap and have clearly defined edges, and are in view in most of the video. Ensuring that the bones of interest are well-resolved in the fluoroscope views will maximize the quality of the resulting bone tracking.

6.1.1 *Mechanics of the VBP*

The biplane fluoroscopy system at the VA Puget Sound consists of two disarticulated fluoroscopes mounted on movable gantries straddling a walkway. Each fluoroscope consists of two major components: the emitter, that generates X-rays, and the image intensifier (II), that collects the X-rays and transforms to a visible-light image, which in turn is captured by a high-speed video

camera. The X-rays are emitted downward through an X-ray transparent plate, with the IIs under the walkway (Figure 6.1). This general configuration allows for the least amount of overlap in the foot bones. For the purposes of the VBP, a pinhole camera model is used to represent the image capture of the IIs. The emitter is represented by a focal point (eye) that emits X-rays in a conical fashion toward the II. The II collects the X-rays onto a phosphor plate, which in this model is considered the imaging plane and its location is defined by corner positions (corners). The cameras capture images from the phosphor plate in a rectangular image which is larger than the diameter of the plate. Ideally, the emitter and II will be aligned such that the center of the imaging plane is the principal point with a principal ray defined as a ray oriented normal to the imaging plate and extending from the principal point to the eye.

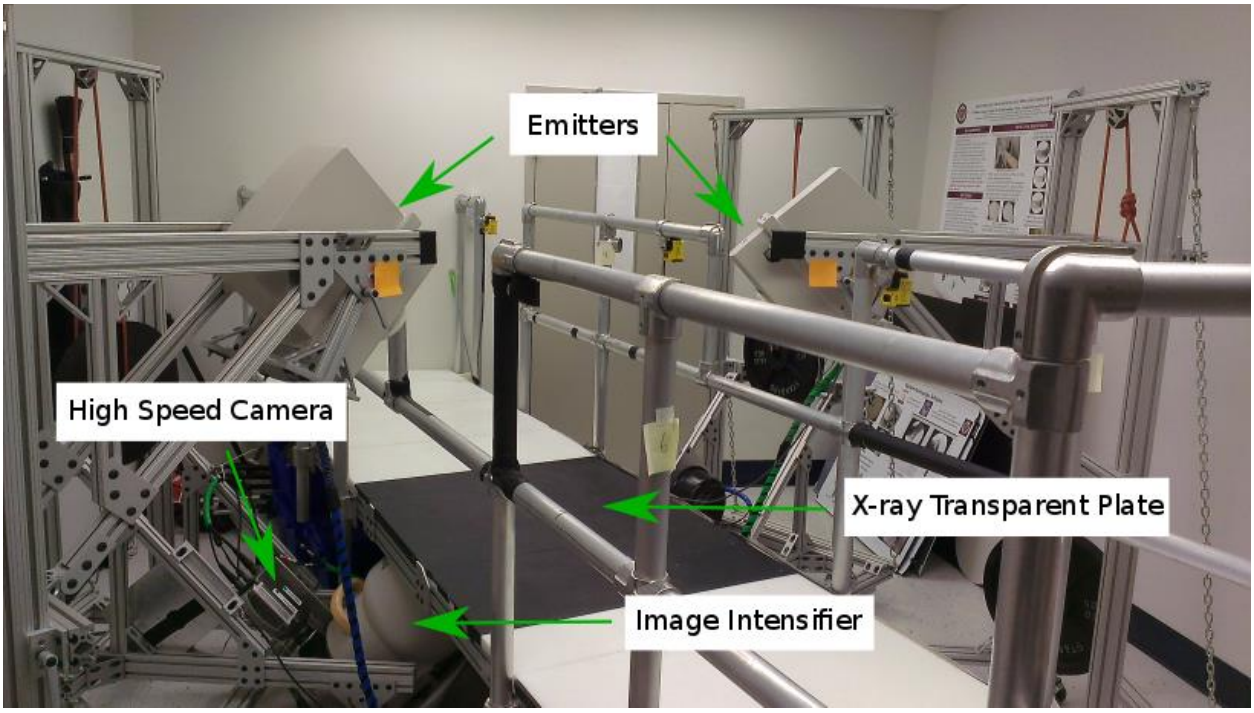

Figure 6.1. The components and general layout of the biplane fluoroscopy laboratory.

A point in 3D space can be mapped to the 2D imaging plane of the II through a direct linear transform (DLT). The DLT assumes that a 3D point can be projected onto the imaging plane by extending a ray from the eye through the 3D point to the imaging plane; the intersection of the ray and plane is the projection of the 3D point in the image. However, reversing the process, i.e. determining the position of a 3D point from one image alone, does not yield a unique solution, as the point could be located anywhere along a single ray (for both emitter/II combinations). The point can be located uniquely in 3D space by determining the closest point (intersection) of these two rays.

Moving the emitters and IIs of the BP is time consuming, cumbersome, and laborious. It is also difficult to determine the quality of the images that will be obtained before the system is moved as the angles are rather oblique and non-intuitive. Once the system is moved, radiation has to be emitted to check the new positioning of the system, which is not ideal as this increases the exposure of the researchers. Further, it is difficult to determine how a moving foot will appear in a given emitter/II position: As we do not currently have a device to "walk" a synthetic foot through the field of view, determining such information would require a living subject to walk through the system, which is undesirable if not also used for data collection.

The VBP allows for the emitter and IIs to be moved virtually to show images from a different system geometry. The positions in virtual space then can be reproduced in the real lab to recreate the virtual set up. The VBP also allows for the determination of infeasible geometries—for example, if two gantries were to collide. Using this system can decrease the time to find a feasible geometry to place the emitters and IIs to obtain better images of the bones of interest.

The walkway, room, emitter and IIs in the VBP were created directly from measurements taken from the BP. Those structures were created as patch objects in Matlab, which are defined by

vertices and are linked together by faces to create 2D surfaces in a 3D environment. To link the VBP and BP, five important reference points were measured in the BP and defined in the VBP. One is the origin of the VBP which is the projection of the center of the carbon fiber plate (the floor panel that is imaged through, reference point E) onto the plane of the room floor. The other four points correspond to the outside corner to the mounting brackets of the vertical supports that hold the walkway up on the floor. Reference points are labeled A-E (Figure 6.2).

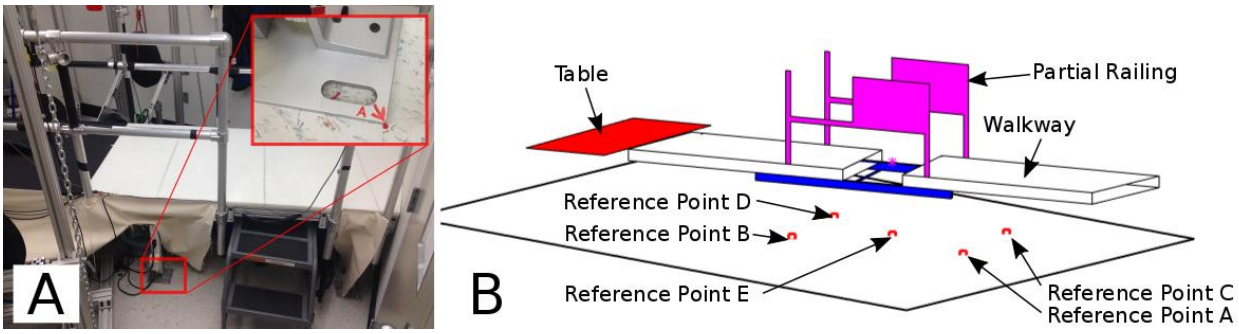

Figure 6.2. A sample reference point of the BP (A), and all of the reference points with the walkway of the VBP (B).

There are also two points of note on each gantry for the emitters and the IIs (markers). In the BP they are the outermost bolts on the backside horizontal bracket of each gantry, and they are defined by vertices in the VBP and projected to the plane of the floor (Figure 6.3). These points are used to match the positions of the gantries in VBP space and BP space. In the BP, the distance between both reference points on the same side as the gantry (either A and B or C and D) and the markers (1 and 2) of the gantry are measured. This produces four measurements (A1, A2, B1, B2) that define the position and orientation of one gantry in space. These measurements can either be

used to check the current position of the BP gantries, or as an input to change the positon of the VBP gantries.

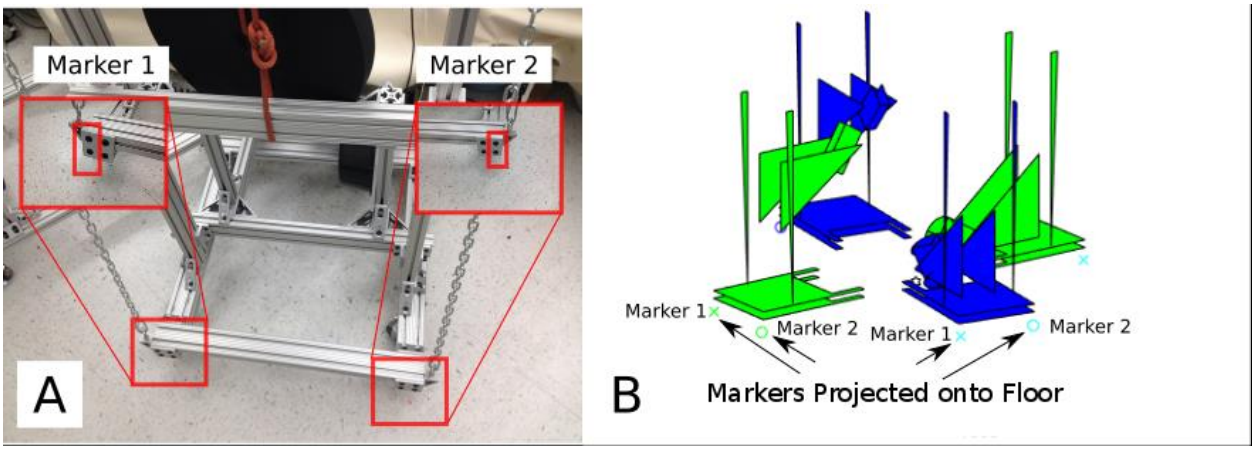

Figure 6.3. The markers on a single gantry in the BP (A) and the markers of an emitter and II gantry projected onto the floor in the VBP (B).

This system has many degrees of freedom which were reduced to eliminate redundancies by assuming a few geometric constraints. The inputs to the VBP are the emitter marker positions in xy space (along the plane defined by the floor) the height of the support structure for the emitter (determining the z coordinate of the emitter), the field of view center (FOVC), and the height of the support structure for the II (z coordinate of the II). The first assumption is that there is a single line connecting the emitter focal point, FOVC and center point of the II screen (principal ray), i.e., the FOVC projects onto the center of the image. The second assumption is that the II screen plane is set perpendicular to the principal ray, i.e., the principal point is the center of the image. These assumptions were made, as it is believed that the highest quality images would result from the emitter sending X-rays centered on the II and not skewed to one side. The pitch of the emitter and II is defined as the angle the device is tilted up or down (similar to an airplane) to align with the principal ray. The position and orientation of the II gantry are linked to the height of the II. Since the II screen center is fixed to move along the principal ray, changing the height of the II moves

the II gantry closer or further to the emitter. The position of the II gantry is defined to be 180 degrees from the emitter gantry enforced by assumptions one and two.

The objective is to link the BP and VBP gantry positions using a measurement system independent of a coordinate system. A variation of triangulation was used to define the marker positions (points on backside of gantries) relative to the reference points (points on floor by vertical support of the walkway). If the VBP is used to determine a position for the BP, the distance between the reference points and markers (for both emitters and IIs) is output from the software so the user can manually position the BP gantries at the specified locations. The opposite can also occur where the user can define the gantry positions in the VBP from measurements taken in the BP. For this case (BP to VBP) the VBP defines the position of the emitter by creating two semicircles around each reference point with radius equal to the distance from the reference point to each marker. The four semicircles (two markers and two reference point distances) are oriented so that they are not under the walkway (infeasible positon in the BP) (Figure 6.4). The position of the marker is defined by where the two semicircles intersect for each marker. By defining both marker positions, the unique position and orientation of the gantry is determined.

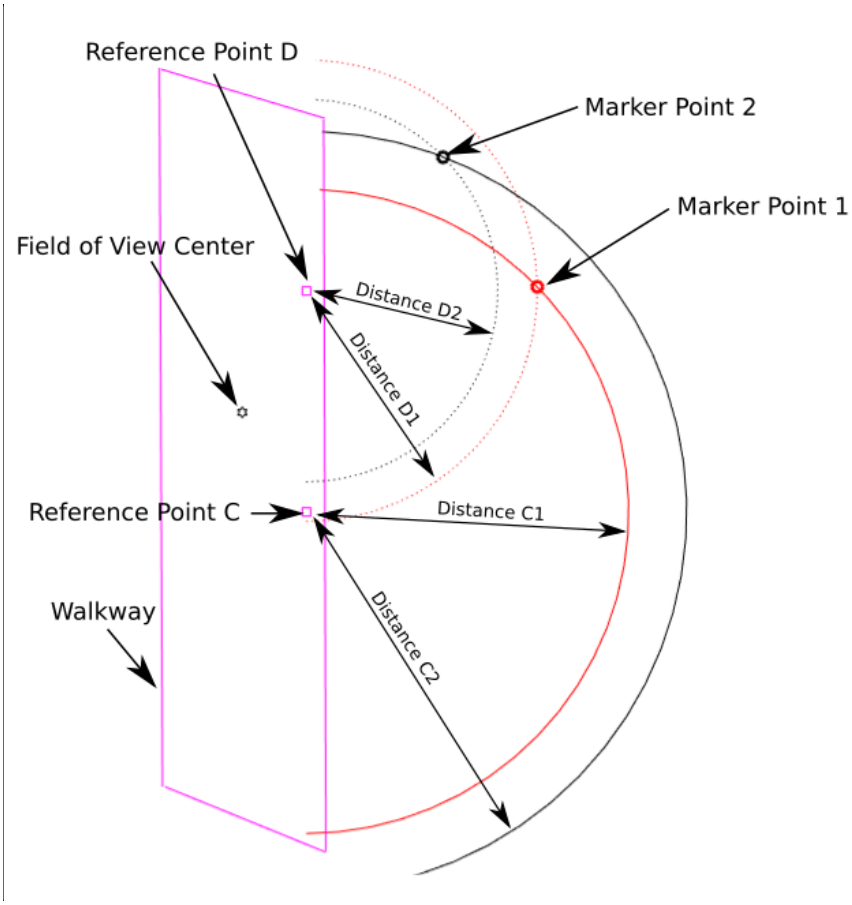

Figure 6.4. An overhead view of the triangulation used to determine the position of the markers of a single gantry.

The VBP displays images of what is captured by the IIs in the specified geometry. Currently, there is no way to quantitatively link the VBP coordinate system to the BP coordinate system (see future work section) through localization. The current method to link the two systems is to transform the BP space into the VBP space by the eye and corner positions. There are five points of interest to determine the imaging geometry. The first is the point from which the X-rays are emitted (eye), and the other four are the corners of the II screen (corners) defining the imaging plane. The goal is to determine an overall transformation, completed in multiple steps, to transform the five BP points to the same location as the five VBP points. The transformation from BP to

VBP is determined in three steps. First the eye of the BP is translated through a displacement vector $\vec{d}$ to the VBP eye, and all the BP corners are also translated by the same amount $\vec{d}$. The second step is to define a vector along the principal ray in both the VBP ($\overrightarrow{r_v}$) and BP ($\overrightarrow{r_B}$). The BP points are then rotated around the eye about an axis defined as $\overrightarrow{r_v} \times \overrightarrow{r_B}$ so that the two principal rays are aligned. The third and last transformation is to rotate the BP corners about the principal rays to match the corners of the IIs (match the lower left, lower right, upper right and upper left corners). A single transformation matrix is created which incorporates these three transformations to transform other points or objects as necessary. Once the imaging geometry is defined, the bones are oriented in the 3D space of the VBP. The bones are also projected onto the imaging plane of both virtual IIs. The virtual emitters and IIs can then be manipulated in the VBP space to refine the projection of the bones on the IIs imaging planes. The marker distances are calculated which can be used to position the real emitters and IIs in the BP through triangulation using the walkway reference points to gantry marker distances.

6.1.2 *Future Improvements to the VBP*

There are changes and improvements that can be made to the VBP software to increase usability and more accurately replicate the BP system.

The current images displayed in the VBP IIs are projections of the bone surfaces (represented as patch objects) onto the IIs while in the BP these are the fluoroscope images. As the fluoroscope images contain interior content and not just the bone surfaces, the VBP images could be replaced by digitally reconstructed radiographs (virtual X-rays) to better match the actual fluoroscope images.

Additional code has to be added to display multiple bones at a time. Displaying multiple bones would allow the user to get a better sense of how bones may overlap or occlude other bones of interest. Also there is an unfinished section of code to input multiple transformation matrices for each bone. This would allow for bones to move through the field of view as if an actual gait trial were taking place.

The purpose of the VBP is to recreate the BP to determine what would be captured in the images of a gait trial in a different imaging geometry. The position of the bone(s) in space and the geometry of the biplane system have to be defined in the VBP for this to occur. The position of the gantries in the VBP is relatable to the position of the BP gantries through the reference point to marker distances. The position of the bone in VBP space should be improved upon from its current form, specifically how the transformation matrix from the BP to VBP space ($T_{bp \rightarrow vbp}$) is defined. Two transformation matrices are needed to place the bone in the VBP space; one is the CT volume space to the biplane lab space transformation ($T_{ct \rightarrow bp}$) which is found through the use of our bone tracking software, the other is the transformation from the BP space to the VBP space ($T_{bp \rightarrow vbp}$). The total transformation would then be $T_{ct \rightarrow bp} \times T_{bp \rightarrow vbp}$. The current method determines $T_{bp \rightarrow vbp}$ by transforming the eye and corners of the BP to the location of the eye and corners of the VBP as described previously. This method is highly dependent upon accurately recreating the gantry positions (thus the eye and corner positions) in the VBP with measurements from the BP (reference point to marker distances). A better method would be to determine this transformation from localization which is the determination of the imaging system in 3D space based on the images of a precision fabricated object (calibration block). The current localization protocol does not accurately and precisely position the calibration block in a specific orientation relative to the walkway. Thus a calibration block to walkway transformation is not specified. A device should be

fabricated to ensure this exact and repeatable placement of the calibration block during the localization protocol so that the BP space can be aligned with the VBP space through this transformation. This new method would directly relate the BP space to the VBP space through the calibration block, which would rely on precise measurements, and could be standardized between all gait trials.

A GUI should be created for the primary user interface. It should include three images that update with every input from the user (VBP room with the walkway and gantries, and both mock fluoroscope images). The marker positions (points on the gantries used to define its position) should also be output. The inputs to the system should include the x and y positions of both emitters as well as its height and the height of the II. This would allow the user to systematically change the position of the emitters and IIs. Marker positions should also be a secondary input so that the user can recreate the BP geometry in the VBP.

6.2 Biplane Fluoroscopy Review

This biplane fluoroscopy review covers six research labs and the validation techniques that they used to determine the accuracy (i.e., bias and precision) of their systems. In this discussion of the validation of biplane fluoroscopy systems, bias is the difference from a known value or the difference from the gold standard measurement that is concurrently recorded, and precision is the variability in the calculated value with repeated measurement. These six labs have published most extensively in this area. Other aspects like localization and distortion correction procedures as well as the lab's hardware were also noted. The purpose of this review is to look at the history of biplane fluoroscopy systems, their progression, and their validation protocols, while evaluating what methods and hardware our lab may want to carry forward.

Biplane fluoroscopy systems capture two sets of X-ray images simultaneously in order to locate bones or markers of interest in 3D space (model-based or marker-based tracking). Prior to tracking, there are two main calibrations that must be performed: distortion correction and localization: There are two different types of image distortion when using biplane fluoroscopy which need to be corrected. First, there is pincushion distortion, in which points further from the center of the image are more displaced in the radial direction relative to their true positions than points closer to the center of the image. Second there is magnetic lens distortion, in which the magnetic fields in the II used to focus the images are affected by external magnetic fields and an "S"-shaped warping of the image is introduced. To distortion correct the images, first a uniform grid of points is imaged. The points in the image can then be mapped to the actual uniform grid points of the plate. Pixel mapping is used to warp the image so that the imaged points match to the corresponding locations of the actual points. The pixel mapping is then applied to all images captured for distortion correction. The geometry of the system also has to be determined to locate objects in 3D space. This is completed by imaging a static object with distinct markers placed at known locations. A direct linear transform (DLT) is then used to calculate the position and orientation of the eye and imaging plane that would result in the obtained fluoroscope images. This provides the geometry of the system and allows for bone tracking.

There are two types of tracking methods commonly used in the literature: model-based tracking and marker-based tracking. For marker-based tracking, high-density spheres are rigidly attached to an object. Three or more markers are needed for every object to define its rigid body motion. The centroid of the spheres are located in both views simultaneously and a DLT is used to locate the sphere in 3D space. Model-based tracking involves a creating a model of the bone to match to the fluoroscope images. Marker-based tracking involves attaching a set of markers (three

or more per bone) to each bone of interest and tracking the markers. In model-based tracking, the subject's bone geometry is typically obtained through either an MRI or CT scan to create a 3D model. The bones are then separated into different volumes (segmentation). A virtual representation of the biplane system is then defined from the localization information, and virtual image intensifier (II) views are generated for the bone model in various 3D poses. The 3D pose of the model which best matches the fluoroscope images is considered the true pose of the bone. The segmented bones can be represented in a number of ways when model-based tracking to the fluoroscope images: contour lines, digitally reconstructed radiographs (DRR), surface models, or silhouettes. Contour line models represent the bones as edges (the outline of the object in addition to defined ridges on the whole outer surface) in the fluoroscope images (typically detected with a Canny edge filter). The surface model represents the bone as a polygonal surface flattened into two dimensions showing the texture of the outer surface of one side. The silhouette models do not contain any internal information about the bones, and are only representative of the outline of the bone. DRRs attempt to mathematically simulate X-rays, by incorporating the interior content and density variation within the bone in addition to the surface information and thus provide the closest match to a fluoroscope image of all the discussed models.

The earliest papers included in this review were conducted in two labs, first at Henry Ford Hospital in Michigan and later at the University of Pittsburgh in Pennsylvania. The first paper by You et al. [73] conducted a validation using a procured canine cadaver tibia mounted to a stage for translation and rotation. Model-based tracking using the DRR method was used to determine the true 3D position of the bone. Tantalum beads were also implanted in the bone to benchmark the accuracy of traditional marker-based tracking. The second part of the study was *in vivo* testing of a canine tibia as the dog walked on a treadmill. Tantalum beads were implanted into the dog's

tibia. *In vitro* tests resulted in 0.23mm and 1.2 degrees for bias for model-based tracking, and ±0.1mm for marker-based tracking when comparing the respective image measurements to the known translational and rotational position. *In vivo* testing had slightly higher bias at 0.5mm and 2.6 degrees comparing the model-based tracking to marker-based tracking. A study in 2003 by Tashman et al. [74] determined the bias and precision of their system with tantalum beads to be 0.02 ± 0.10mm and 0.064 ± 0.31 degrees. This was determined by dropping a precision machined rod with the beads positioned 30mm apart. Three more validation studies were completed [75–77] using the following joints: glenohumeral/scapular, knee, and cervical spine. All of these validations reported bias and precision values of less than 1mm translation and 1degree in rotation for static and dynamic trials. The validations were all completed in situations that closely represented physiological movements and conditions (intact soft tissue with a cadaver), compared against marker-based tracking whose accuracy was quantified in the earlier studies mentioned. This research lab has also utilized semiautomatic model-based tracking to determine the position of the bones in 3D space, using a cluster of microcomputers. Specifically, the DRRs were matched to the actual fluoroscope images using an optimization procedure. The geometry determination of the system was conducted using a 3D calibration block and calculating the DLT to obtain the emitter and II geometry that would create the image.

The next lab that has published validations of a biplane fluoroscopy system was at Massachusetts General Hospital and Harvard University. The first papers published by this lab used simple geometric objects for their validation. Li et al. [78] used a precision machined cylinder and a sphere, and compared the known physical dimensions to the calculated center to center distances. The reported bias and precision was less than 0.1mm and 0.1 degrees with manual image registration through Rhinoceros (McNeel & Associates, Seattle). Bingham et al. [79] conducted

two validation experiments: one imaged 8 spheres with different densities packed together, the other was a virtual exercise matching a CAD model of a total knee arthroplasty device to itself in an arbitrary position. In both validations, the objects were converted to point clouds which were then matched. The calculated center-to-center distances of the spheres from imaging was compared to the actual machined radii of the spheres. The image registration was semiautomatic using a contour model-based tracking by creating a virtual environment in Rhinoceros. The maximum bias and precision in both validations was less than 0.1mm and 0.1 degrees. Future studies manually aligned the object models to the imaged objects using the same software. One study by Defrate et al. [80] imaged a knee in static poses in various ranges of flexion and used a goniometric measurement as a gold standard. Wang et al. [81] axially translated a cadaver spine in a material testing machine, and used the position of the machine as the gold standard. Lin et al. [82] used titanium beads inserted into a cadaver pelvis and femur as a reference for their validation. Reported bias and precision for these studies was also less than 1mm and 1 degree. Four studies [62,63,83,84] conducted *in vivo* studies of the foot, where the human subjects moved in semi-physiologic movements. For two studies, the subjects raised a foot into the air and while elevated positioned it in maximum dorsiflexion and plantar flexion, then maximum pronation and supination [62,63]. The other study involved the subject stepping into the field of view and positioning their foot at heelstrike, midstance and toe off to be imaged statically [83,84]. As the frame rate of the fluoroscope systems was 30 Hz, quasi-static imaging was completed to prevent motion blur. The fluoroscope C-arms were also not disarticulated so that a subject could not move through the field of view unimpeded. Some of the major limitations to the studies as a whole is that the model-based tracking is completed manually which could potentially reduce the speed and practicality of processing large data sets, as well as introduce human error. The validation

procedures used simple geometric figures which may be easier to manually match than more physiological items such as bones with soft tissue.

The biplane fluoroscopy lab located at Duke University is similar to the Massachusetts General Hospital system. A single paper was found describing their validation methods. Caputo et al. [64] rotated a cadaver ankle in maximum plantarflexion and dorsiflexion with radio-opaque beads implanted in the tibia, calcaneus and talus. The position of the beads was then compared to the model of the bones, which were manually aligned to the images through Rhinoceros. The bias ± precision was 0.04 ± 0.11mm for translation and 0.2 ± 0.1 degrees for rotation. The methods presented in this paper are very similar to that presented from the papers in Guoan Li's lab. They also had two intact fluoroscopes which would not allow for a subject to freely walk through the system.

There were two papers found describing the validation of the biplane fluoroscopy system at Steadman Philippon. Both papers—one analyzing the knee [85] and the other the shoulder [86]used beads implanted in the bones of interest and compared them to the model of the bones' positions. The largest bias and precision out of both of the studies was in Giphart et al. [86] with 0.3 ± 0.4mm for translation and 1.7 ± 1.2 degrees for rotation when comparing the model-based tracking to marker-based tracking. They used commercial registration software (Model-Based Roentgen Stereophotogrammetric Analysis, Medis Specials, BV, Leiden, The Netherlands) for model-based tracking. The models were defined as inner and outer surface contours, and they were matched to the fluoroscope images. They used a 15cm calibration cube and calculated the DLT to determine the geometry of the fluoroscope system. To correct for distortion in the fluoroscope images obtained, they imaged a precision-machined aluminum plate with 406 holes, and applied the distortion correction approach discussed earlier.

The fifth lab covered in this review is at Brown University. One study by Brainerd et al. [87] utilized marker-based tracking to capture the kinematics of minipigs chewing. To determine bias and precision, a machined rod with beads attached at precise and specified positions was moved through the field of view. Comparing the bead distances calculated from imaging to the known bead positions, the system accuracy was reported to have bias of 0.08mm and precision of 0.046mm. Precision was also tested *in vivo* with 4 to 5 tantalum beads implanted in the mandible and skull of minipigs. The inter-marker distances were measured as the minipigs chewed. The precision was less than 0.1mm. Miranda et al. [88] determined their system's bias and precision for model a matching and marker-based tracking. For model-based tracking, human cadaver bone was rigidly attached to a stage that could translate or rotate by a precise amount. Marker data was captured simultaneously with tantalum beads attached to a polycarbonate post. The model and marker positions were compared to the stage position. For static analysis the marker bias ± precision was 0.09 ± 0.08 degrees for rotation, and 0.12 ± 0.08mm for translation. Static model-based tracking gave a bias ± precision of 0.44 ± 0.26 degrees for rotation, and 0.33 ± 0.27mm for translation. The dynamic test was completed with the same bones and marker setup as the static trials and only rotational data were reported. The dynamic marker-based tracking was 0.10 ± 0.06 degrees and the dynamic model-based tracking was 0.14 ± 0.12 degrees. These studies compared the stage position to marker-based tracking and model-based tracking. The exclusion of soft tissue for the bias measurements of the bone may be a limiting factor in the validation of this system. The model-based tracking was completed by a semiautomatic open source optimization routine (XROMM, www.xromm.org) which matches the DRR to the fluoroscope images.

The last biplane fluoroscopy lab covered in this review is located at Keio University in Japan. Ito et al. [65] imaged static and dynamic tarsal bones for validation. The bias ± precision

was 0.27±0.19mm for translation and 0.24±0.19 degrees for rotation in static validation trials and 0.36±0.19mm translation and 0.42±0.30 degrees for rotation in dynamic validation trials. The validation did not include soft tissue around the bones, and were not the bones of interest for the rest of the study (tibia, talus, calcaneus). Automatic custom model-based tracking software was used to determine the position and orientation of the bones that used a polygonal surface models of the bones matched to the fluoroscope images.

The research labs had varying methods for data collection during validations along with different ways of processing data. To be equivalent to the other systems cited in this review, our validation studies should show a bias and precision of less than 1mm and 1 degree. The studies in the review that used simple geometric shapes for validation showed a lower bias and variability in tracking than validation studies that conducted *in vitro* or *in vivo* testing. The studies with simple geometric shapes may not be fully representative of *in vivo* bone motion and the validation results are unclear as how they pertain to physiologic motion and tissue. For this reason, our validation tests will closely mimic actual physiologic motion and tissue. Marker-based tracking can be used as a gold standard for model-based tracking approaches as previously seen in other systems, but should first be validated in our own system. We have decided to use DRRs as bone models since they contain the most amount of information, which may lead to better model-based tracking results. There is more data involved with DRRs than the other methods, but increases in computing power and the intelligent use of technology can shorten data processing time. We have implemented a semiautomatic data model-based tracking algorithm that utilizes a graphics processing unit to render DRRs. The multi-threaded capability of a GPU to render a DRR is faster than the serial processing capabilities of a CPU which decreases the time needed to create the DRR for every optimization iteration. An initial positon is defined for the bone of interest, then the bone

is iteratively manipulated in six degrees of freedom by an optimization algorithm to minimize the normalized correlation coefficient (NCC). The NCC is composed of six components, the intensity, horizontal gradient and vertical gradient for both views. The DRR is best matched to the fluoroscope image when the NCC is minimized. We plan to use these approaches to guide our use and evolution of the system.

6.3 Risk of Bias Table

Table 6.2. Methodological quality of included studies with a modified Downs and Black Checklist.

Results

Author	Reporting (n=8)	External Validity (n=2)	Internal Validity (n=5)	Power (n=1)	Total (n=16)	Percent
Crenshaw [17]	7	0	4	0	11	68.75
Kerrigan [31]	7	2	4	0	13	81.25
Maly [40]	8	2	4	0	14	87.5
Nester [25]	6	0	3	0	9	56.25
Kakihana [18]	6	0	4	0	10	62.5
Kakihana [7]	8	2	4	0	14	87.5
Kakihana [13]	8	2	4	0	14	87.5
Schmalz [19]	7	0	3	0	10	62.5
Shimada [52]	8	2	3	0	13	81.25
Kakihana [8]	8	2	5	0	15	93.75
Butler [32]	7	0	4	1	12	75
Kuroyanagi [34]	7	2	5	0	14	87.5
Erhart [20]	8	0	4	0	12	75
Hinman [35]	8	2	5	0	15	93.75
Hinman [36]	8	2	4	0	14	87.5
Hinman [37]	8	2	4	0	14	87.5
Butler [33]	7	0	4	1	12	75
Nakajima [21]	7	0	4	1	12	75
Segal [51]	8	2	4	1	15	93.75
Abdallah [41]	6	2	4	0	12	75
Leitch [22]	6	0	4	0	10	62.5
Barrios [42]]	8	2	4	1	15	93.75
Hinman [9]	8	2	4	0	14	87.5
Kang [26]	7	2	4	1	14	87.5
Pagani [48]	7	2	3	0	12	75
Arazpour [49]	7	2	4	0	13	81.25

Russell [14]	8	0	4	1	13	81.25
Jones [47]	8	0	4	0	12	75
Jones [45]	7	0	4	1	12	75
Jones [46]	7	2	4	0	13	81.25
Moyer [50]	7	2	4	0	13	81.25
Russell [16]	7	0	4	1	12	75
Telfer [15]	8	2	4	0	14	87.5
Jones [38]	8	2	4	0	14	87.5
Molgaard [28]	8	0	4	0	12	75
Pagani [29]	8	0	4	0	12	75
Tipnis [24]	7	0	4	1	12	75
Yeh [27]	8	0	4	0	12	75
Chapman [39]	8	2	4	0	14	87.5
Jones [47]	8	2	4	0	14	87.5
Duivenvoorden[43]	8	2	4	1	15	93.75
Fu [30]	5	2	3	0	10	62.5
Hsu [44]	8	0	4	1	13	81.25
Mean± SD						79.9±9.4

Reporting

1. Is the hypothesis/aim/objective of the study clearly described?
2. Are the main outcomes to be measured clearly described in the Introduction or Methods?
3. Are the characteristics of the patients included in the study clearly described?
4. Are the interventions of interest clearly described?
5. Are the distributions of principal confounders in each group of subjects to be compared clearly described?

   Confounders: Walking speed – similar between conditions.

6. Are the main findings of the study clearly described?
7. Does the study provide estimates of the random variability in the data for the main outcomes?
8. Have the actual probability values been reported (e.g. 0.035 rather than <0.05) for the main outcomes except where the probability value is less than 0.001?

External Validity

9. Were the subjects asked to participate in the study representative of the entire population from which they were recruited?

10. Were those subjects who were prepared to participate representative of the entire population from which they were recruited?

Internal Validity

11. Were the interventions applied in a random order?

12. Was an attempt made to blind those measuring the main outcomes of the intervention?

13. If any of the results of the study were based on "data dredging", was this made clear?

14. Were the statistical tests used to assess the main outcomes appropriate?

15. Were the main outcomes measures used accurate (valid and reliable)?

Power

16. Did the study report a power calculation before recruitment, and was the recruitment equal to or greater than the calculated number of subjects to detect a clinically important effect where the probability value for a difference due to chance is less than 5%?

6.1 AVERAGE KINEMATICS OF INDIVIDUAL SUBJECTS

The average kinematic plots of each subject, in the sagittal, frontal, and transverse planes are shown for each of the bone to bone pairs (talus relative to the tibia, calcaneus relative to the talus and the calcaneus relative to the tibia), with each of the four insole conditions tested. These

trajectories are the average of three walking trials per condition. The shaded region around each curve is the standard deviation for the specified condition.

6.1.1 *Subject 1*

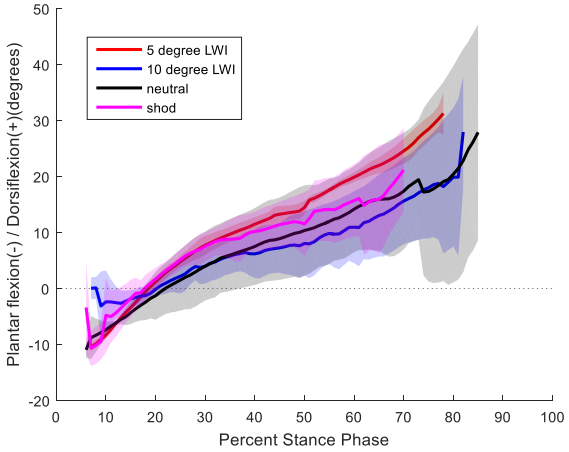

Figure 6.5. The talus relative to tibia in the sagittal plane for subject 1.

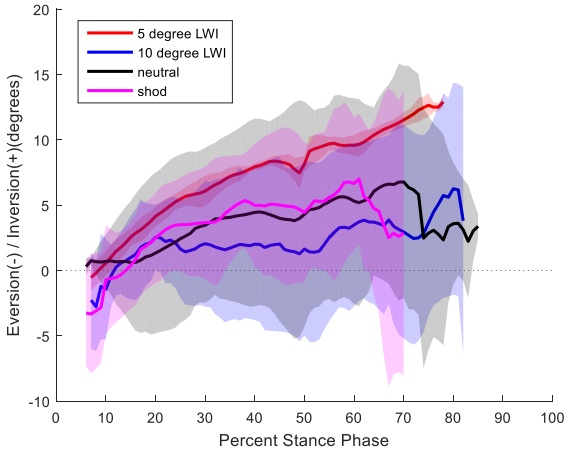

Figure 6.6. The talus relative to the tibia in the frontal plane for subject 1.

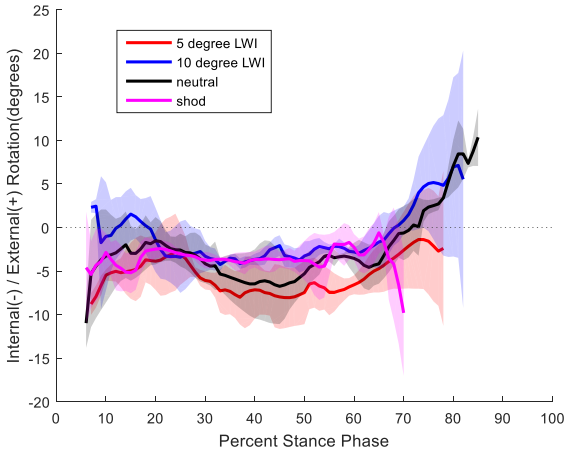

Figure 6.7. The talus relative to the tibia in the transverse plane for subject 1.

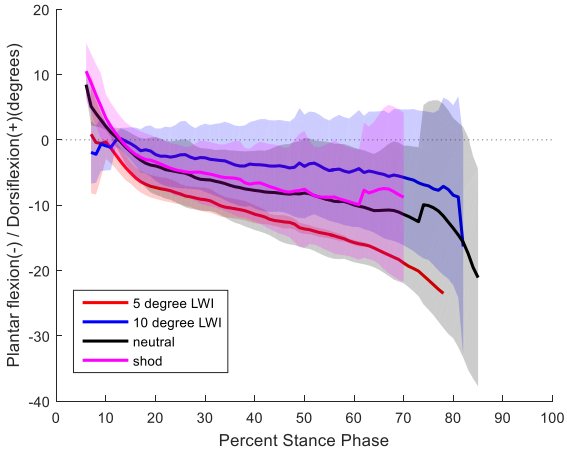

Figure 6.8. The calcaneus relative to the talus in the sagittal plane for subject 1.

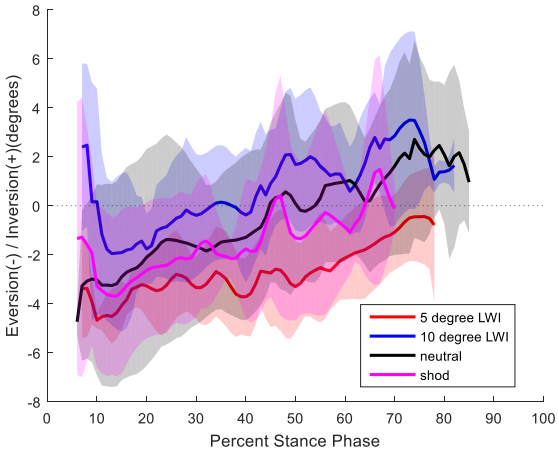

Figure 6.9. The calcaneus relative to the talus in the frontal plane for subject 1.

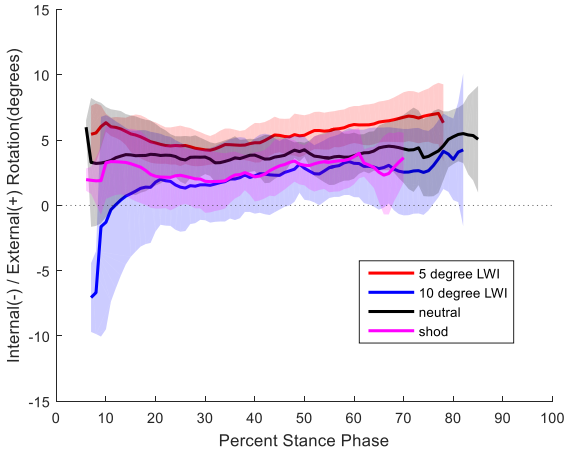

Figure 6.10. The calcaneus relative to the talus in the transverse plane for subject 1.

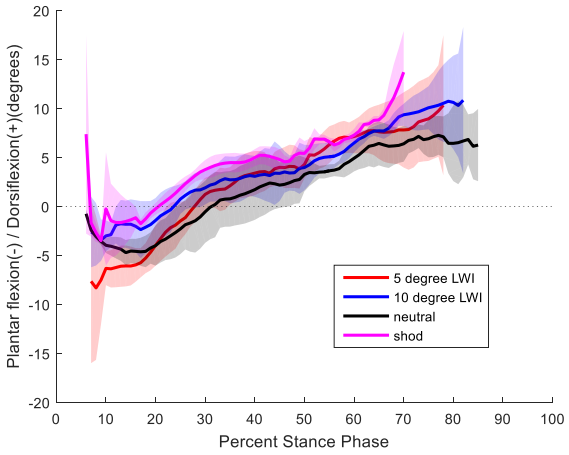

Figure 6.11. The calcaneus relative to the tibia in the sagittal plane for subject 1.

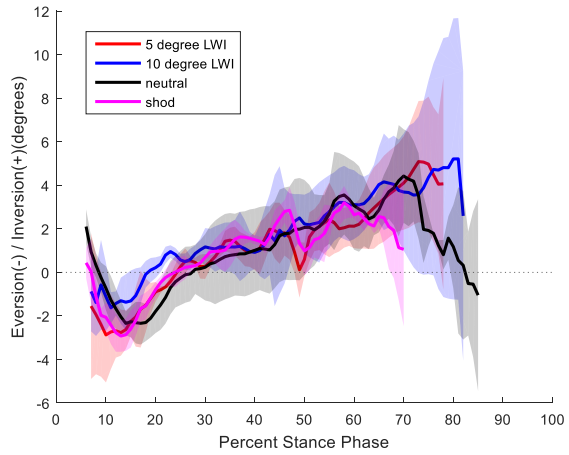

Figure 6.12. The calcaneus relative to the tibia in the frontal plane for subject 1.

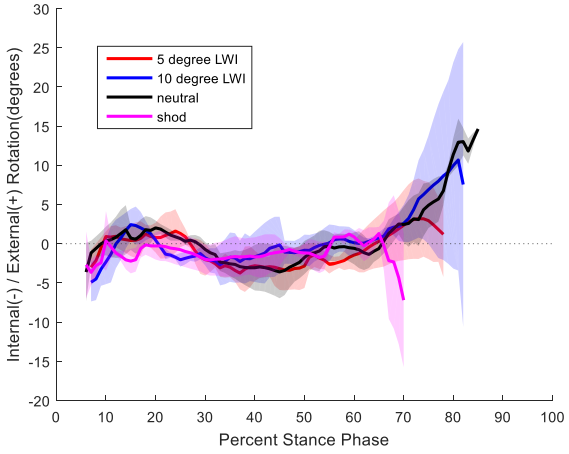

Figure 6.13. The calcaneus relative to the tibia in the transverse plane for subject 1.

6.1.2 *Subject 2*

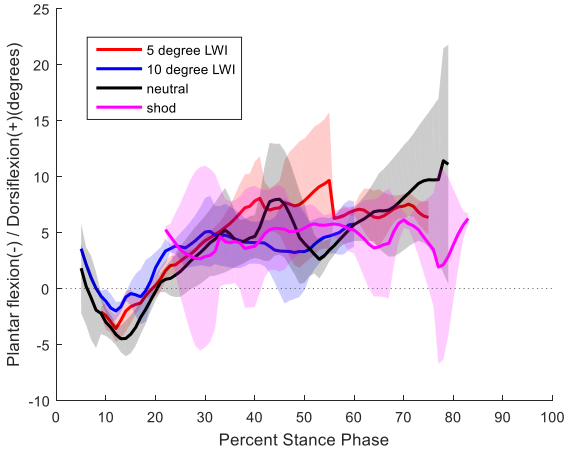

Figure 6.14. The talus relative to the tibia in the sagittal plane for subject 2.

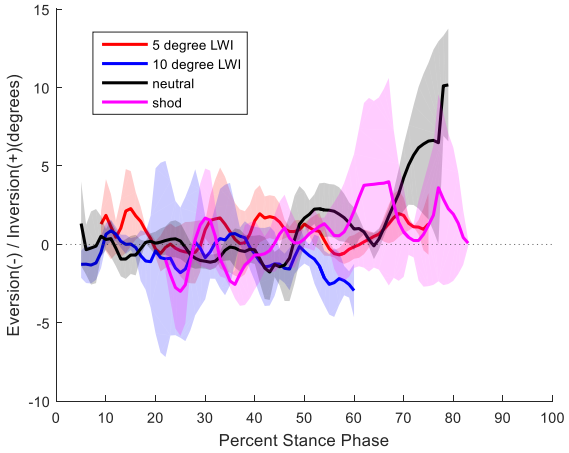

Figure 6.15. The talus relative to the tibia in the frontal plane for subject 2.

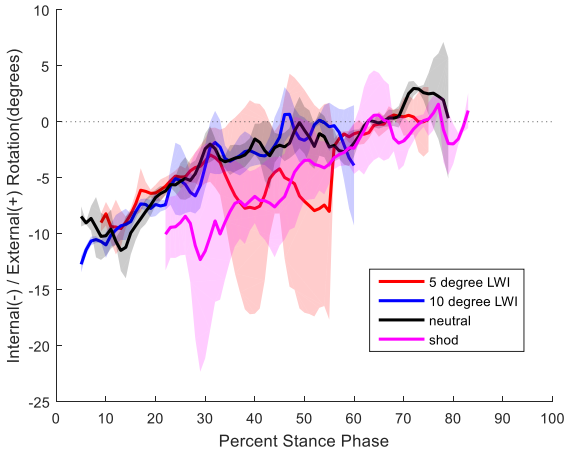

Figure 6.16. The talus relative to the tibia in the transverse plane for subject 2.

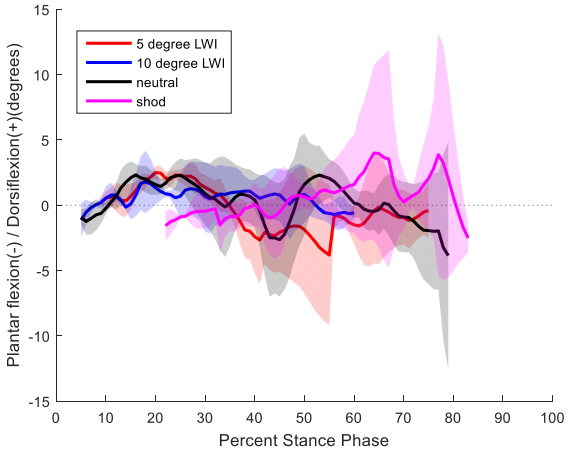

Figure 6.17. The calcaneus relative to the talus in the sagittal plane for subject 2.

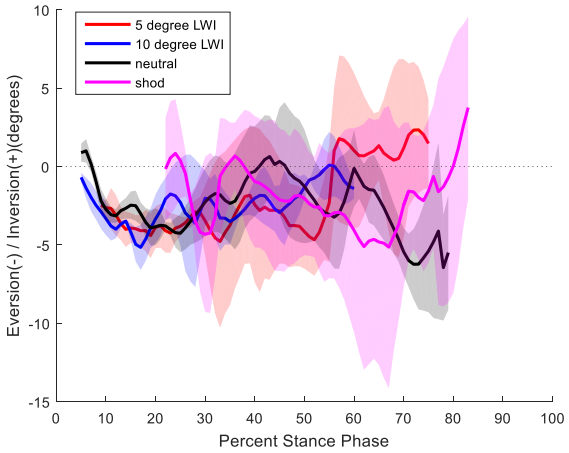

Figure 6.18. The calcaneus relative to the talus in the frontal plane for subject 2.

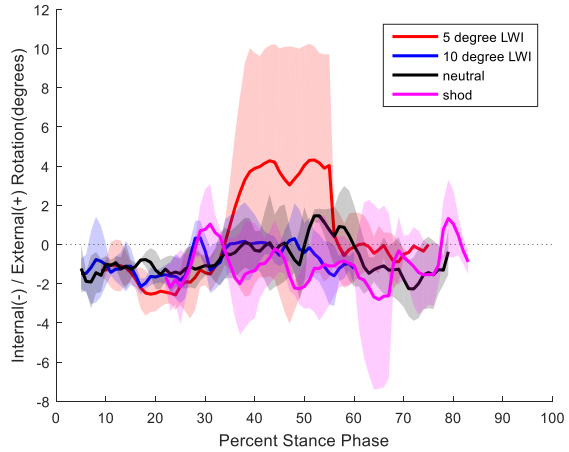

Figure 6.19. The calcaneus relative to the talus in the transverse plane for subject 2.

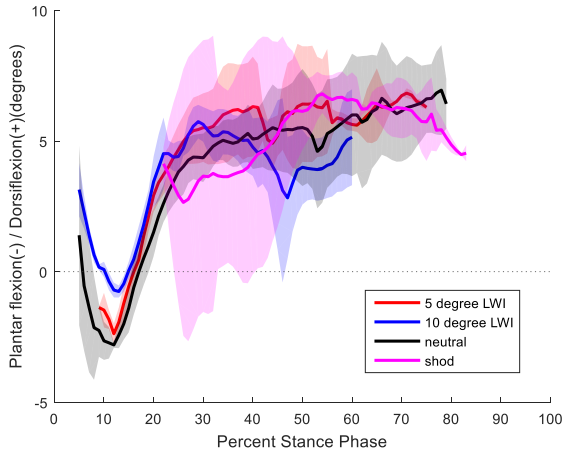

Figure 6.20. The calcaneus relative to the tibia in the sagittal plane for subject 2.

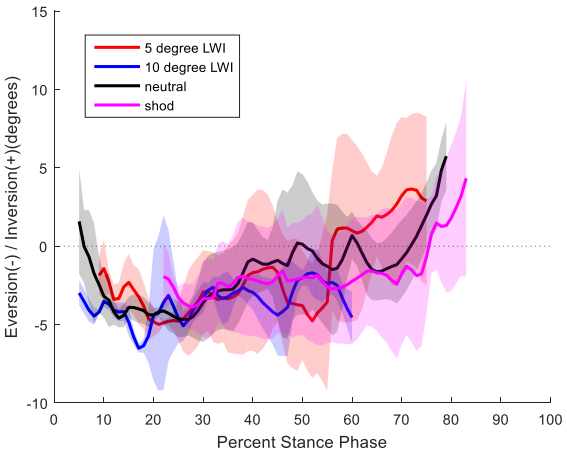

Figure 6.21. The calcaneus relative to tibia in the frontal plane for subject 2.

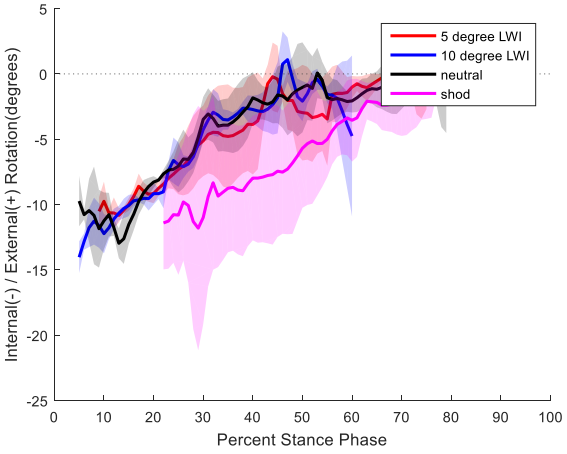

Figure 6.22. The calcaneus relative to the tibia in the transverse plane for subject 2.

6.1.3 *Subject 3*

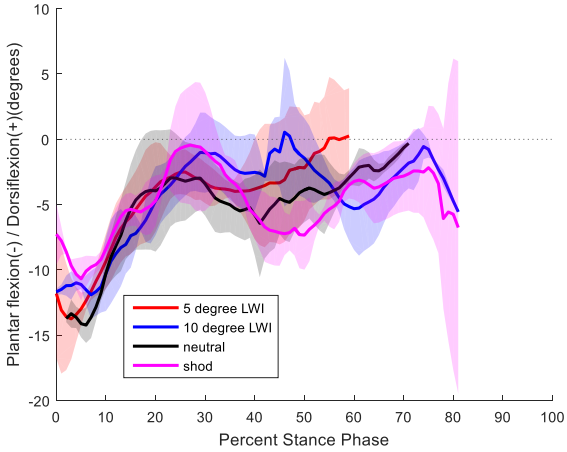

Figure 6.23. The talus relative to the tibia in the sagittal plane for subject 3.

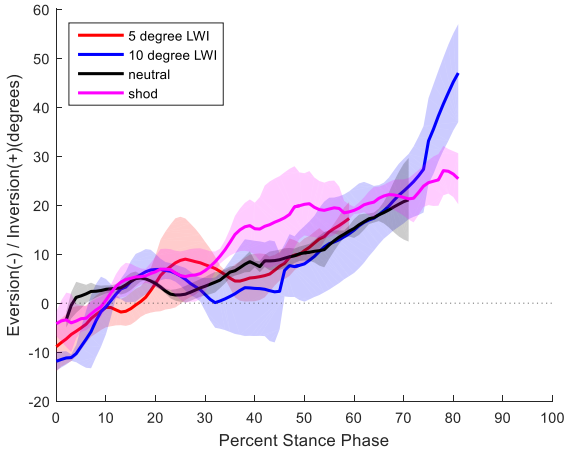

Figure 6.24. The talus relative to the tibia in the frontal plane for subject 3.

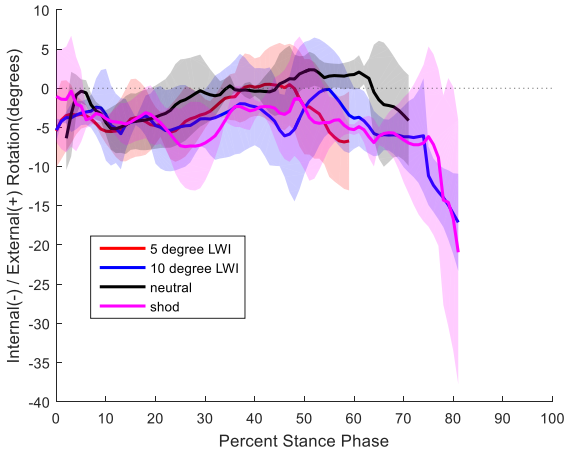

Figure 6.25. The talus relative to the tibia in the transverse plane for subject 3.

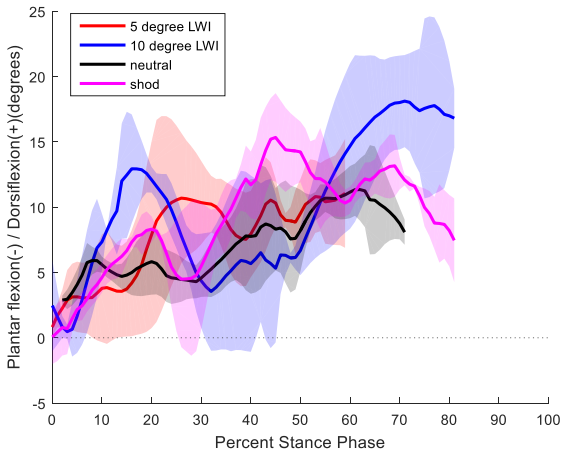

Figure 6.26. The calcaneus relative to the talus in the sagittal plane for subject 3.

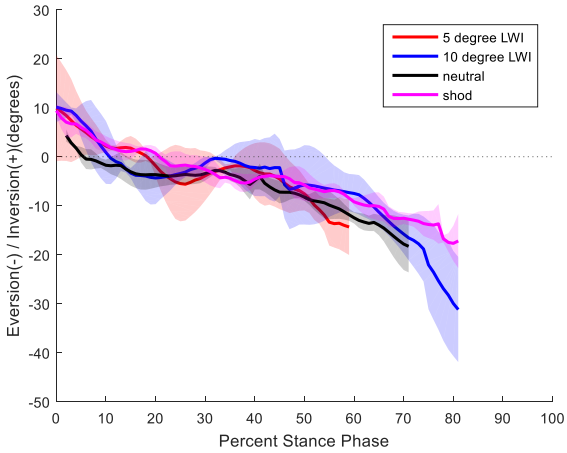

Figure 6.27. The calcaneus relative to the talus in the frontal plane for subject 3.

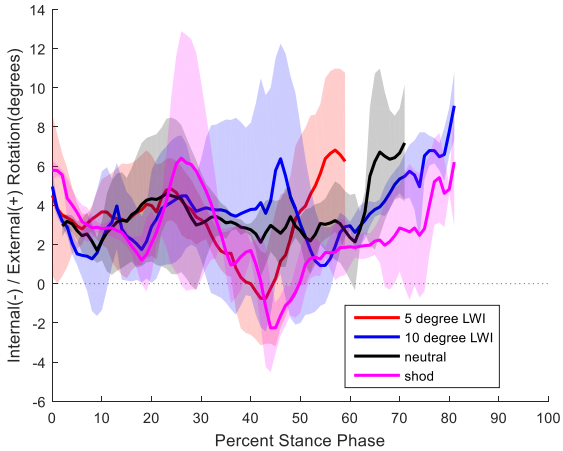

Figure 6.28. The calcaneus relative to the talus in the transverse plane for subject 3.

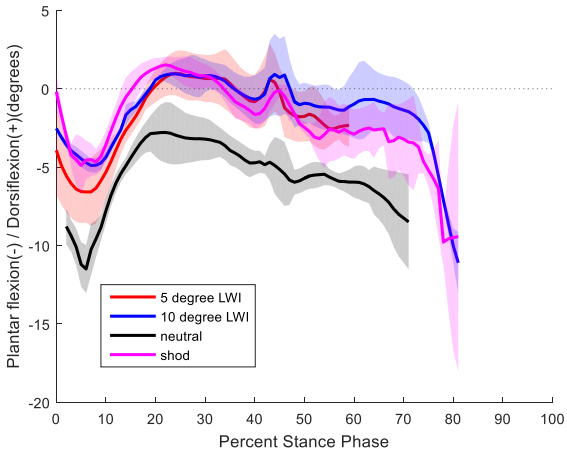

Figure 6.29. The calcaneus relative to the tibia in the sagittal plane for subject 3.

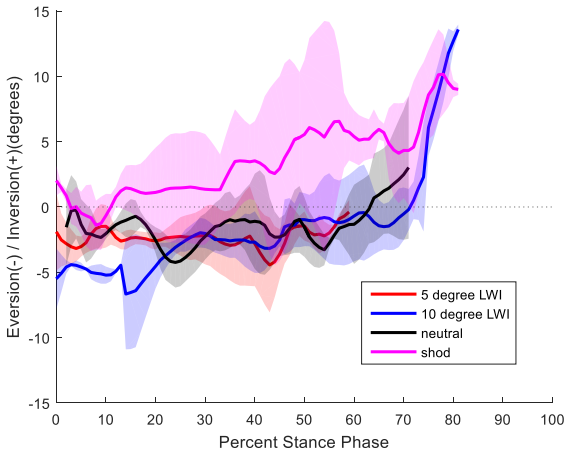

Figure 6.30. The calcaneus relative to the tibia in the frontal plane for subject 3.

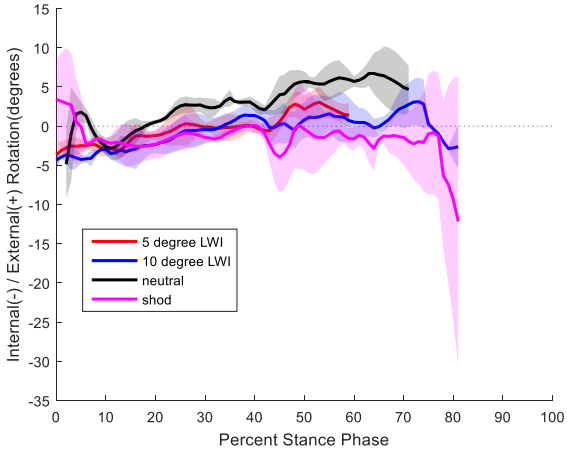

Figure 6.31. The calcaneus relative to the tibia in the transverse plane for subject 3.

BIBLIOGRAPHY

[1] Bedson J, Jordan K, Croft P. The Prevalence and history of knee osteoarthritis in general practice: a case-control study. Fam Pract 2005;22:103–8.

[2] Andriacchi T. Dynamics of knee malalignment 1994;25:395–403.

[3] Sharma L, Hurwitz DE, EUGENE JAT, Sum JA, Lenz ME, Dunlop DD, et al. Knee adduction moment, serum hyaluronan level, and disease severity in medial tibiofemoral osteoarthritis. Age 1998;6:15.

[4] Zhao D, Banks SA, Mitchell KH, D'Lima DD, Colwell CW, Fregly BJ. Correlation between the knee adduction torque and medial contact force for a variety of gait patterns. J Orthop Res 2007;25:789–97. doi:10.1002/jor.20379.

[5] Amin S, Luepongsak N, McGibbon CA, LaValley MP, Krebs DE, Felson DT. Knee adduction moment and development of chronic knee pain in elders: Adduction Moment and New Knee Pain. Arthritis Care Res 2004;51:371–6. doi:10.1002/art.20396.

[6] Miyazaki T, Wada M, Kawahara H, Sato M, Baba H, Shimada S. Dynamic load at baseline can predict radiographic disease progression in medial compartment knee osteoarthritis. Ann Rheum Dis 2002;61:617–22.

[7] Kakihana W, Akai M, Nakazawa K, Takashima T, Naito K, Torii S. Effects of Laterally Wedged Insoles on Knee and Subtalar Joint Moments. Arch Phys Med Rehabil 2005;86:1465–71. doi:10.1016/j.apmr.2004.09.033.

[8] Kakihana W, Akai M, Nakazawa K, Naito K, Torii S. Inconsistent Knee Varus Moment Reduction Caused by a Lateral Wedge in Knee Osteoarthritis: Am J Phys Med Rehabil 2007;86:446–54. doi:10.1097/PHM.0b013e31805bfff5.

[9] Hinman RS, Bowles KA, Metcalf BB, Wrigley TV, Bennell KL. Lateral wedge insoles for medial knee osteoarthritis: Effects on lower limb frontal plane biomechanics. Clin Biomech 2012;27:27–33. doi:10.1016/j.clinbiomech.2011.07.010.

[10] Hall JPL, Barton C, Jones PR, Morrissey D. The Biomechanical Differences Between Barefoot and Shod Distance Running: A Systematic Review and Preliminary Meta-Analysis. Sports Med 2013;43:1335–53. doi:10.1007/s40279-013-0084-3.

[11] Munteanu S, Barton C. Lower limb biomechanics during running in individuals with achilles tendonopthay: a systematic review. J Foot Ankle Res 2011;4.

[12] Robbins S, Maly MR. The effect of gait speed on the knee addduction moment depends on waveform summary measures. Gait Posture 2009;30:543–6.

[13] Kakihana W, Torii S, Akai M, Nakazawa K, Fukano M, Naito K. Effect of a Lateral Wedge on Joint Moments During Gait in Subjects with Recurrent Ankle Sprain: Am J Phys Med Rehabil 2005;84:858–64. doi:10.1097/01.phm.0000179519.65254.37.

[14] Russell EM, Miller RH, Umberger BR, Hamill J. Lateral wedges alter mediolateral load distributions at the knee joint in obese individuals. J Orthop Res 2013;31:665–71. doi:10.1002/jor.22248.

[15] Telfer S, Abbott M, Steultjens MPM, Woodburn J. Dose–response effects of customised foot orthoses on lower limb kinematics and kinetics in pronated foot type. J Biomech 2013;46:1489–95. doi:10.1016/j.jbiomech.2013.03.036.

[16] Russell EM, Hamill J. Lateral wedges decrease biomechanical risk factors for knee osteoarthritis in obese women. J Biomech 2011;44:2286–91. doi:10.1016/j.jbiomech.2011.05.033.

[17] Crenshaw S, Pollo F, Calton E. Effects of lateral-wedged insoles on kinetics at the knee 2000:185–92.

[18] Kakihana W, Akai M, Yamasaki N, Takashima T, Nakazawa K. Changes of Joint Moments in the Gait of Normal Subjects Wearing Laterally Wedged Insoles: Am J Phys Med Rehabil 2004;83:273–8. doi:10.1097/01.PHM.0000118035.71195.DE.

[19] Schmalz T, Blumentritt S, Drewitz H, Freslier M. The influence of sole wedges on frontal plane knee kinetics, in isolation and in combination with representative rigid and semi-rigid ankle–foot-orthoses. Clin Biomech 2006;21:631–9. doi:10.1016/j.clinbiomech.2006.02.004.
[20] Erhart JC, Mündermann A, Mündermann L, Andriacchi TP. Predicting changes in knee adduction moment due to load-altering interventions from pressure distribution at the foot in healthy subjects. J Biomech 2008;41:2989–94. doi:10.1016/j.jbiomech.2008.07.021.
[21] Nakajima K, Kakihana W, Nakagawa T, Mitomi H, Hikita A, Suzuki R, et al. Addition of an arch support improves the biomechanical effect of a laterally wedged insole. Gait Posture 2009;29:208–13. doi:10.1016/j.gaitpost.2008.08.007.
[22] Leitch KM, Birmingham TB, Jones IC, Giffin JR, Jenkyn TR. In-shoe plantar pressure measurements for patients with knee osteoarthritis: Reliability and effects of lateral heel wedges. Gait Posture 2011;34:391–6. doi:10.1016/j.gaitpost.2011.06.008.
[23] Jones RK, Zhang M, Laxton P, Findlow AH, Liu A. The biomechanical effects of a new design of lateral wedge insole on the knee and ankle during walking. Hum Mov Sci 2013;32:596–604. doi:10.1016/j.humov.2012.12.012.
[24] Tipnis RA, Anloague PA, Laubach LL, Barrios JA. The dose–response relationship between lateral foot wedging and the reduction of knee adduction moment. Clin Biomech 2014;29:984–9. doi:10.1016/j.clinbiomech.2014.08.016.
[25] Nester CJ, Van Der Linden ML, Bowker P. Effect of foot orthoses on the kinematics and kinetics of normal walking gait. Gait Posture 2003;17:180–7.
[26] Kang JW, Park HS, Na CK, Park JW, Hong J, Lee SH. Immediate Coronal Plane Kinetic Effects of Novel Lateral-offset Sole Shoes and Lateral-wedge Insole Shoes in Healthy Individuals. Orthopedics 2013;36:e165–71. doi:10.3928/01477447-20130122-18.
[27] Yeh H-C, Chen L-F, Hsu W-C, Lu T-W, Hsieh L-F, Chen H-L. Immediate Efficacy of Laterally Wedged Insoles With Arch Support on Walking in Persons With Bilateral Medial Knee Osteoarthritis. Arch Phys Med Rehabil 2014;95:2420–7. doi:10.1016/j.apmr.2014.06.014.
[28] Mølgaard CM, Graven-Nielsen T, Simonsen O, Kersting UG. Potential interaction of experimental knee pain and laterally wedged insoles for knee off-loading during walking. Clin Biomech 2014;29:848–54. doi:10.1016/j.clinbiomech.2014.08.002.
[29] Pagani CHF, Willwacher S, Benker R, Brüggemann G-P. Effect of an ankle–foot orthosis on knee joint mechanics: A novel conservative treatment for knee osteoarthritis. Prosthet Orthot Int 2013:0309364613513297.
[30] Fu HC, Lie CW, Ng T, Chen K, Tse C, Wong W. Prospective study on the effects of orthotic treatment for medial knee osteoarthritis in Chinese patients: clinical outcome and gait analysis. Hong Kong Med J 2015. doi:10.12809/hkmj144311.
[31] Kerrigan DC, Lelas JL, Goggins J, Merriman GJ, Kaplan RJ, Felson DT. Effectiveness of a lateral-wedge insole on knee varus torque in patients with knee osteoarthritis. Arch Phys Med Rehabil 2002;83:889–93. doi:10.1053/apmr.2002.33225.
[32] Butler RJ, Marchesi S, Royer T, Davis IS. The effect of a subject-specific amount of lateral wedge on knee mechanics in patients with medial knee osteoarthritis. J Orthop Res 2007;25:1121–7. doi:10.1002/jor.20423.
[33] Butler RJ, Barrios JA, Royer T, Davis IS. Effect of laterally wedged foot orthoses on rearfoot and hip mechanics in patients with medial knee osteoarthritis. Prosthet Orthot Int 2009;33:107–16. doi:10.1080/03093640802613237.
[34] Kuroyanagi Y, Nagura T, Matsumoto H, Otani T, Suda Y, Nakamura T, et al. The lateral wedged insole with subtalar strapping significantly reduces dynamic knee load in the medial compartment. Osteoarthritis Cartilage 2007;15:932–6. doi:10.1016/j.joca.2007.02.004.

[35] Hinman RS, Payne C, Metcalf BR, Wrigley TV, Bennell KL. Lateral wedges in knee osteoarthritis: What are their immediate clinical and biomechanical effects and can these predict a three-month clinical outcome? Arthritis Rheum 2008;59:408–15. doi:10.1002/art.23326.
[36] Hinman RS, Bowles KA, Payne C, Bennell KL. Effect of length on laterally-wedged insoles in knee osteoarthritis. Arthritis Rheum 2008;59:144–7. doi:10.1002/art.23249.
[37] Hinman RS, Bowles K, Bennell KL. Laterally wedged insoles in knee osteoarthritis: do biomechanical effects decline after one month of wear? BMC Musculoskelet Disord 2009;10:146. doi:10.1186/1471-2474-10-146.
[38] Jones RK, Chapman GJ, Forsythe L, Parkes MJ, Felson DT. The relationship between reductions in knee loading and immediate pain response whilst wearing lateral wedged insoles in knee osteoarthritis: REDUCTION OF MEDIAL LOADING AND PAIN RESPONSE. J Orthop Res 2014;32:1147–54. doi:10.1002/jor.22666.
[39] Chapman GJ, Parkes MJ, Forsythe L, Felson DT, Jones RK. Ankle motion influences the external knee adduction moment and may predict who will respond to lateral wedge insoles?: an ancillary analysis from the SILK trial. Osteoarthritis Cartilage 2015. doi:10.1016/j.joca.2015.02.164.
[40] Maly MR, Culham EG, Costigan PA. Static and dynamic biomechanics of foot orthoses in people with medial compartment knee osteoarthritis. Clin Biomech 2002;17:603–10.
[41] Abdallah AA, Radwan AY. Biomechanical changes accompanying unilateral and bilateral use of laterally wedged insoles with medial arch supports in patients with medial knee osteoarthritis. Clin Biomech 2011;26:783–9. doi:10.1016/j.clinbiomech.2011.03.013.
[42] Barrios JA, Butler RJ, Crenshaw JR, Royer TD, Davis IS. Mechanical effectiveness of lateral foot wedging in medial knee osteoarthritis after 1 year of wear. J Orthop Res 2013;31:659–64. doi:10.1002/jor.22252.
[43] Duivenvoorden T, van Raaij TM, Horemans HLD, Brouwer RW, Bos PK, Bierma-Zeinstra SMA, et al. Do Laterally Wedged Insoles or Valgus Braces Unload the Medial Compartment of the Knee in Patients With Osteoarthritis? Clin Orthop Relat Res 2015;473:265–74. doi:10.1007/s11999-014-3947-5.
[44] Hsu W-C, Jhong Y-C, Chen H-L, Lin Y-J, Chen L-F, Hsieh L-F. Immediate and long-term efficacy of laterall-wedged insoles on persons with bilateral medial knee osteoarthritis during walking. BioMed Eng Online 2015;14.
[45] Jones RK, Nester CJ, Richards JD, Kim WY, Johnson DS, Jari S, et al. A comparison of the biomechanical effects of valgus knee braces and lateral wedged insoles in patients with knee osteoarthritis. Gait Posture 2013;37:368–72. doi:10.1016/j.gaitpost.2012.08.002.
[46] Jones RK, Chapman GJ, Findlow AH, Forsythe L, Parkes MJ, Sultan J, et al. A new approach to prevention of knee osteoarthritis: reducing medial load in the contralateral knee. J Rheumatol 2013;40:309–15.
[47] Jones RK, Chapman GJ, Parkes MJ, Forsythe L, Felson DT. The effect of different types of insoles or shoe modifications on medial loading of the knee in persons with medial knee osteoarthritis: a randomised trial: THE EFFECT OF DIFFERENT TYPES OF INSOLES OR SHOE. J Orthop Res 2015;33:1646–54. doi:10.1002/jor.22947.
[48] Fantini Pagani CH, Hinrichs M, Brüggemann G-P. Kinetic and kinematic changes with the use of valgus knee brace and lateral wedge insoles in patients with medial knee osteoarthritis. J Orthop Res 2012;30:1125–32. doi:10.1002/jor.22032.
[49] Arazpour M, Bani MA, Maleki M, Ghomshe FT, Kashani RV, Hutchins SW. Comparison of the efficacy of laterally wedged insoles and bespoke unloader knee orthoses in treating medial compartment knee osteoarthritis. Prosthet Orthot Int 2013;37:50–7.
[50] Moyer RF, Birmingham TB, Dombroski CE, Walsh RF, Leitch KM, Jenkyn TR, et al. Combined Effects of a Valgus Knee Brace and Lateral Wedge Foot Orthotic on the External Knee Adduction Moment

in Patients With Varus Gonarthrosis. Arch Phys Med Rehabil 2013;94:103–12. doi:10.1016/j.apmr.2012.09.004.
[51] Segal NA, Foster NA, Dhamani S, Ohashi K, Yack HJ. Effects of Concurrent Use of an Ankle Support with a Laterally Wedged Insole for Medial Knee Osteoarthritis. PM&R 2009;1:214–22. doi:10.1016/j.pmrj.2008.09.005.
[52] Shimada S, Kobayashi S, Wada M, Uchida K, Sasaki S, Kawahara H, et al. Effects of Disease Severity on Response to Lateral Wedged Shoe Insole for Medial Compartment Knee Osteoarthritis. Arch Phys Med Rehabil 2006;87:1436–41. doi:10.1016/j.apmr.2006.08.018.
[53] Hinman RS, Bardin L, Simic M, Bennell KL. Medial arch supports do not significantly alter the knee adduction moment in people with knee osteoarthritis. Osteoarthritis Cartilage 2013;21:28–34. doi:10.1016/j.joca.2012.10.009.
[54] Kemp G, Crossley KM, Wrigley TV, Metcalf BR, Hinman RS. Reducing joint loading in medial knee osteoarthritis: Shoes and canes. Arthritis Rheum 2008;59:609–14. doi:10.1002/art.23578.
[55] Kerrigan DC, Karvosky ME, Lelas JL, Riley PO. Men's shoes and knee joint torques relevant to the development and progression of knee osteoarthritis. J Rheumatol 2003;30:529–33.
[56] Kerrigan DC, Franz JR, Keenan GS, Dicharry J, Della Croce U, Wilder RP. The Effect of Running Shoes on Lower Extremity Joint Torques. PM&R 2009;1:1058–63. doi:10.1016/j.pmrj.2009.09.011.
[57] Levinger P, Menz HB, Fotoohabadi MR, Feller JA, Bartlett JR, Bergman NR. Foot posture in people with medial compartment knee osteoarthritis. J Foot Ankle Res 2010;3:29.
[58] Toda Y, Tsukimura N, Kato A. The effects of different elevations of laterally wedged insoles with subtalar strapping on medial compartment osteoarthritis of the knee. Arch Phys Med Rehabil 2004;85:673–7. doi:10.1016/j.apmr.2003.06.011.
[59] Toda Y, Tsukimura N, Segal N. An optimal duration of daily wear for an insole with subtalar strapping in patients with varus deformity osteoarthritis of the knee. Osteoarthritis Cartilage 2005;13:353–60. doi:10.1016/j.joca.2004.12.012.
[60] Toda Y, Tsukimura N. A 2-year follow-up of a study to compare the efficacy of lateral wedged insoles with subtalar strapping and in-shoe lateral wedged insoles in patients with varus deformity osteoarthritis of the knee. Osteoarthritis Cartilage 2006;14:231–7. doi:10.1016/j.joca.2005.09.006.
[61] Radzimski AO, Mündermann A, Sole G. Effect of footwear on the external knee adduction moment — A systematic review. The Knee 2012;19:163–75. doi:10.1016/j.knee.2011.05.013.
[62] De Asla RJ, Wan L, Rubash HE, Li G. Six DOF in vivo kinematics of the ankle joint complex: Application of a combined dual-orthogonal fluoroscopic and magnetic resonance imaging technique. J Orthop Res 2006;24:1019–27. doi:10.1002/jor.20142.
[63] De Asla RJ, Kozánek M, Wan L, Rubash HE, Li G. Function of anterior talofibular and calcaneofibular ligaments during in-vivo motion of the ankle joint complex. J Orthop Surg 2009;4:7. doi:10.1186/1749-799X-4-7.
[64] Caputo AM, Lee JY, Spritzer CE, Easley ME, DeOrio JK, Nunley JA, et al. In Vivo Kinematics of the Tibiotalar Joint After Lateral Ankle Instability. Am J Sports Med 2009;37:2241–8. doi:10.1177/0363546509337578.
[65] Ito K, Shimizu M, Ikemoto S, Kume S, Niagura T, Imanishi N, et al. Direct assessment of 3D foot bone kinematics using biplanar X-ray fluoroscopy and an automatic model registration method. J Foot Ankle Res 2015;8.
[66] Campbell KJ, Wilson KJ, LaPrade RF, Clanton TO. Normative rearfoot motion during barefoot and shod walking using biplane fluoroscopy. Knee Surg Sports Traumatol Arthrosc 2016;24:1402–8. doi:10.1007/s00167-014-3084-4.
[67] Iaquinto JM, Tsai R, Haynor DR, Fassbind MJ, Sangeorzan BJ, Ledoux WR. Marker-based validation of a biplane fluoroscopy system for quantifying foot kinematics. Med Eng Phys 2014;36:391–6. doi:10.1016/j.medengphy.2013.08.013.

[68] Iaquinto J, Kindig M, Haynor DR, Vu Q, Pepin N, Tsai R, et al. Model-Based Tracking of the Bones of the Foot: A Biplane Fluoroscopy Validation Study In Reviews.
[69] Jian Y, Winter DA, Ishac M, Gilchrist L. Trajectory of the body COG and COP during initiation and termination of gait. Gait Posture n.d.:9–22.
[70] Breniere Y, Do M. When and how does steady state gait movement induced from upright posture begin? J Biomech n.d.;19:1035–40.
[71] Marchelli GLS. GPU-Accelerated Tools for Medical Image Registration and Biomechanical Modeling. 2015.
[72] Wang B, Roach KE, Kapron AL, Fiorentino NM, Saltzman CL, Singer M, et al. Accuracy and feasibility of high-speed dual fluoroscopy and model-based tracking to measure in vivo ankle arthrokinematics. Gait Posture 2015;41:888–93. doi:10.1016/j.gaitpost.2015.03.008.
[73] You B, Anderst W, Tashman S. In Vivo Measurement of 3-D Skeletal Kinematics from Sequences of Biplane Radiographs: Application to Knee Kinematics. IEEE Trans Med Imaging 2001;20:514–25.
[74] Tashman S, Anderst W. In-Vivo Measurement of Dynamic Joint Motion Using High Speed Biplane Radiography and CT: Application to Canine ACL Deficiency. J Biomech Eng 2003;125:238. doi:10.1115/1.1559896.
[75] Bey MJ, Zauel R, Brock SK, Tashman S. Validation of a New Model-Based Tracking Technique for Measuring Three-Dimensional, In Vivo Glenohumeral Joint Kinematics. J Biomech Eng 2006;128:604. doi:10.1115/1.2206199.
[76] Anderst W, Zauel R, Bishop J, Demps E, Tashman S. Validation of three-dimensional model-based tibio-femoral tracking during running. Med Eng Phys 2009;31:10–6. doi:10.1016/j.medengphy.2008.03.003.
[77] Haque MA, Anderst W, Tashman S, Marai GE. Hierarchical model-based tracking of cervical vertebrae from dynamic biplane radiographs. Med Eng Phys 2013;35:994–1004. doi:10.1016/j.medengphy.2012.09.012.
[78] Li G. Feasibility of Using Orthogonal Fluoroscopic Images to Measure In Vivo Joint Kinematics. J Biomech Eng 2004;126:313. doi:10.1115/1.1691448.
[79] Bingham J, Li G. An Optimized Image Matching Method for Determining In-Vivo TKA Kinematics with a Dual-Orthogonal Fluoroscopic Imaging System. J Biomech Eng 2006;128:588. doi:10.1115/1.2205865.
[80] DeFrate LE, Sun H, Gill TJ, Rubash HE, Li G. In vivo tibiofemoral contact analysis using 3D MRI-based knee models. J Biomech 2004;37:1499–504. doi:10.1016/j.jbiomech.2004.01.012.
[81] Wang S, Passias P, Li G, Li G, Wood K. Measurement of Vertebral Kinematics Using Noninvasive Image Matching Method–Validation and Application. Spine 2008;33:E355–61.
[82] Lin H, Wang S, Tsai T-Y, Li G, Kwon Y-M. In-vitro validation of a non-invasive dual fluoroscopic imaging technique for measurement of the hip kinematics. Med Eng Phys 2013;35:411–6. doi:10.1016/j.medengphy.2012.10.004.
[83] Wan L, de Asla RJ, Rubash HE, Li G. Determination of in-vivo articular cartilage contact areas of human talocrural joint under weightbearing conditions. Osteoarthritis Cartilage 2006;14:1294–301. doi:10.1016/j.joca.2006.05.012.
[84] Wan L, de Asla RJ, Rubash HE, Li G. In vivo cartilage contact deformation of human ankle joints under full body weight. J Orthop Res 2008;26:1081–9. doi:10.1002/jor.20593.
[85] Torry MR, Shelburne KB, Peterson DS, Giphart JE, Krong JP, Myers C, et al. Knee Kinematic Profiles during Drop Landings: A Biplane Fluoroscopy Study. Med Sci Sports Exerc 2011;43:533–41. doi:10.1249/MSS.0b013e3181f1e491.
[86] Giphart JE, van der Meijden OAJ, Millett PJ. The effects of arm elevation on the 3-dimensional acromiohumeral distance: a biplane fluoroscopy study with normative data. J Shoulder Elbow Surg 2012;21:1593–600. doi:10.1016/j.jse.2011.11.023.

[87] Brainerd EL, Baier DB, Gatesy SM, Hedrick TL, Metzger KA, Gilbert SL, et al. X-ray reconstruction of moving morphology (XROMM): precision, accuracy and applications in comparative biomechanics research. J Exp Zool Part Ecol Genet Physiol 2010;9999A:n/a – n/a. doi:10.1002/jez.589.
[88] Miranda D, Schwartz J, Loomis A, Brainerd EL, Fleming B, Crisco JJ. Static and Dynamic Error of a Biplanar Videoradiography System Using Marker-Based and Markerless Tracking Techniques. J Biomech Eng 2011;133.